



UNIVERSITÀ DEGLI STUDI DI MESSINA

Dipartimento di Ingegneria

**Dottorato di Ricerca in
INGEGNERIA CIVILE, AMBIENTALE E DELLA SICUREZZA
Ciclo XXXV**

Curriculum

Scienze e tecnologie, materiali, energia e sistemi complessi per il calcolo distribuito e le reti

Settore disciplinare: ICAR/o8

**Novel dynamic-stiffness approaches to the dynamics of
metamaterial structures**

Dottorando: Ing. Andrea Francesco Russillo

Coordinatore: Prof. Ing. Gaetano Bosurgi

Supervisore: Prof. Ing. Giuseppe Failla

Anno accademico 2021/2022

ACKNOWLEDGMENTS

Firstly, I want to thank my advisor Prof. Giuseppe Failla, whose unwavering, patient and irreplaceable support guided my PhD path and taught me the most valuable lessons. Secondly, my gratitude is to my parents, to whom I owe everything.

CONTENTS

Preface	11
1 Locally-resonant metamaterial beams	17
1.1 Problem under study	17
1.2 Governing equations	18
1.3 Dynamic-stiffness method	19
1.4 Modal analysis	28
1.5 Wave propagation in a locally-resonant beam	32
1.6 Numerical application	35
1.7 Conclusions	45
2 Locally-resonant metamaterial plates	47
2.1 Introduction	47
2.2 Reduced-order model	47
2.3 Reduced-order global dynamic-stiffness matrix	52
2.4 Modal response of the reduced-order dynamic-stiffness model	59
2.5 Numerical applications	62
2.6 Conclusions	74
3 Wave propagation in nonlocal Rayleigh lattices	75
3.1 Wave propagation in nonlocal lattices	75
3.2 Exact dynamic-stiffness approach	79
3.3 Finite-element approach	82
3.4 Numerical examples	90
3.5 Conclusions	100
Summary and conclusions	100
A List of Symbols - Chapter 1	103

B List of Symbols - Chapter 2	109
C List of Symbols - Chapter 3	113

LIST OF FIGURES

Locally-resonant metamaterial beam.	18
Mass-spring-dashpot chain consisting of N_r resonators attached at $x = x_h$	20
Boundary conditions for generalized displacements and forces. . .	25
Highlighted n^{th} unit cell of a locally-resonant beam and adjacent cells.	33
Cantilever locally-resonant sandwich beam hosting 1-DOF or 2-DOF resonators.	35
Band gaps of the infinite sandwich beam in Figure 1.5 with 1-DOF resonators.	38
Transmittance of the cantilever locally-resonant sandwich beam in Figure 2 with 1-DOF resonators.	38
FRF for tip deflection of cantilever locally-resonant beam in Figure 2 with 1-DOF resonators.	39
Tip deflection of the cantilever locally-resonant beam in Figure 1.5 with 1-DOF resonators.	40
Band gaps of the infinite sandwich beam in Figure 1.5 with 2-DOF resonators.	41
Transmittance of the cantilever locally-resonant sandwich beam in Figure 2 with 2-DOF resonators.	41
FRF for tip deflection of cantilever sandwich beam in Figure 1.5 with 2-DOF resonators.	42
Tip deflection of the cantilever locally-resonant beam in Figure 1.5 for 2-DOF resonators	44
Locally-resonant metamaterial plates.	48
System under study.	49
Resonators of the system in Figure 2.2.	50

Parallel-strip subdivision of the plates of the system in Figure 2.2, according to the space distribution of the resonators.	53
Generalized displacement (a) and forces (b) for a plate strip.	54
Assembly procedure of the dynamic-stiffness matrix of the system in Figure 2.2.	56
Assembly procedure for the dynamic-stiffness matrices of two consecutive plates of the system in Figure 2.2 coupled by an array of resonators.	57
Locally-resonant metamaterial plate consisting of two simply-supported plates connected by 1-DOF resonators	63
Mode shapes of the system in Figure 2.8, calculated by the proposed reduced-order dynamic-stiffness model.	65
Amplitude of the deflection frequency response function (FRF) at $\mathbf{x} = (0.05, -0.45)$ in the bottom plate for concentrated harmonic $1e^{i\omega t}$ load applied at $\mathbf{x}_f = (0.05, 0.45)$ in the bottom plate.	66
Amplitude of the frequency response function (FRF) for concentrated harmonic load $1e^{i\omega t}$, $\omega = 101$ Hz, applied at $\mathbf{x}_f = (0.05, 0.45)$ in the bottom plate.	68
Amplitude of the frequency response function (FRF) for concentrated harmonic load $1e^{i\omega t}$, $\omega = 142.1$ Hz, applied at $\mathbf{x}_f = (0.05, 0.45)$ in the bottom plate.	69
Amplitude of the frequency response function (FRF) for concentrated harmonic load $1e^{i\omega t}$, $\omega = 241.8$ Hz, applied at $\mathbf{x}_f = (0.05, 0.45)$ in the bottom plate.	70
Time deflection at $\mathbf{x} = (0.05, -0.45)$ in the bottom plate for concentrated sine load $1 \sin(\omega t)$, $\omega = 80$ Hz, applied at $\mathbf{x}_f = (0.05, 0.45)$ in the bottom plate.	71
Time deflection for concentrated sine load $1 \sin(\omega t)$, $\omega = 80$ Hz, applied at $\mathbf{x}_f = (0.05, 0.45)$ in the bottom plate.	72
Time deflection of top/bottom plates and displacements of resonators at line $x = 0.05$ for concentrated sine load $1 \sin(\omega t)$, $\omega = 80$ Hz, applied at $\mathbf{x}_f = (0.05, 0.45)$ in the bottom plate.	73
Periodic planar beam lattices: (a) triangular lattice, (b) Kagome lattice.	75
Degrees of freedom of a unit cell for a generic two-dimensional periodic structure.	79

Dynamic-stiffness approach: Stress-driven nonlocal lattice member modelled by a unique two-node beam element.	79
Finite-element approach: Stress-driven nonlocal lattice member modelled by n two-node beam elements.	82
Dispersion curves along the irreducible Brillouin zone computed by the dynamic-stiffness approach and the finite-element approach.	91
Dispersion curves along the irreducible Brillouin computed by the finite-element approach for various internal lengths.	95
Dispersion curves along the irreducible Brillouin zone computed by the dynamic-stiffness approach, Euler-Bernoulli theory and the finite-element approach.	96
Dispersion curves along the irreducible Brillouin zone computed by the dynamic-stiffness approach and the finite-element approach for various internal lengths.	97
Dispersion curves along the irreducible Brillouin zone computed by the dynamic-stiffness approach and the finite-element approach for the same internal length $L_c = 2 \times 10^{-5}$ m and various thicknesses at constant relative density of the lattice. .	98
Dispersion curves along the irreducible Brillouin zone computed by the dynamic-stiffness approach and the finite-element approach for the same internal length $L_c = 4 \times 10^{-5}$ m and various thicknesses at constant relative density of the lattice. .	99

LIST OF TABLES

Complex eigenvalues of the cantilever locally-resonant sandwich beam in Figure 1.5 with 1-DOF resonators.	37
Complex eigenvalues of the cantilever locally-resonant sandwich beam in Figure 1.5 with 2-DOF resonators	43
First 20 natural frequencies of system in Figure 2.8, calculated by proposed reduced-order dynamic-stiffness model (DSM) and FE model in Abaqus (FEM).	64
Basis vectors of the triangular and Kagome lattices. l denotes the length of each lattice member.	76

PREFACE

In the last decades, a new class of artificial materials, going by the name of *mechanical metamaterials*, has received considerable attention owing to their exotic mechanical properties and found an extremely wide range of applications (e.g., among others, sensing [52, 61], soft robots [36], seismic barriers [37, 38, 45, 51, 57], elastic cloaking [22, 28]). Among other behaviours, mechanical metamaterials may exhibit remarkable wave attenuation properties due to two intrinsic features, namely periodicity and local resonance. These two characteristics lend themselves to be included in new conceptions of structural systems.

Metamaterial structures are structural systems that are tailored in such a way to possess periodicity in conjunction with local resonance effects. To the first class belong all the structures that exhibit a structural periodicity whose scale is comparable to the wave length of the propagating wave [26]; these structures go by the name of *phononic crystals*. In the second class are included all the structural systems, known as *locally-resonant acoustic metamaterials*, that are endowed with periodic arrays of suitably tuned resonant subsystems.

Metamaterial structures have been subject of numerous studies and several structural typologies have been investigated, such as locally-resonant metamaterial beams [23, 24, 34, 59, 76, 82, 88, 91, 92], locally-resonant metamaterial plates [2, 25, 32, 33, 43, 44, 56, 60, 63, 77–81, 87, 89, 90, 93] and periodic lattices [53, 72, 73]. As a consequence, the formulation of exact and analytical methods is of fundamental interest for the investigation of the dynamic response and dispersion properties of metamaterial structures, which can serve as a benchmark for the standard numerical techniques that are usually employed [2, 33, 43, 44, 56, 78, 87, 93].

The purpose of this thesis is to propose new exact and analytical methods for the computation of the dynamic response and the wave propa-

gation analysis of metamaterial structures by means of dynamic-stiffness based techniques. The dynamic-stiffness method presents itself as a very powerful method since it allows to exactly relate the response variables of continuous system, i.e. containing an infinite number of degrees of freedom, in the frequency domain through a finite set of degrees of freedom, namely the response variables sampled at the boundary nodes of the system. This result is achieved by making use of the analytical solutions of the governing equations of the structure, which leads to a frequency-dependent relationship between the response variables at the boundary, that is the generalized forces and displacements defined at the boundary nodes; such a relationship is given by the so-called dynamic-stiffness matrix [3].

The origin of the dynamic-stiffness matrix concept can be traced back to the Dynamic Slope Deflection Method proposed by Koloušek [39–41], where, for the first time, frequency-dependent dynamic stiffness coefficients, known as *Koloušek functions*, have been derived from the free vibration response of a Euler-Bernoulli beam. This work enabled the development of the concept of dynamic-stiffness matrix, that is the exact relationship between the nodal response variables in the frequency domain [19]. Subsequently, the dynamic-stiffness matrix has been formulated for beams, such as tapered beams [15, 16], rotating beams [5, 6, 13], twisted beams [7, 10], sandwich beams [9, 12, 14], functionally graded beams [74, 75], and more recently for plates [46–49]. Remarkably, the dynamic-stiffness approach has been employed to investigate beams carrying mass-spring systems [11], although the study has been limited only to cantilever beams carrying a spring-mass system at the tip and without performing any dynamic condensation. The application of the dynamic-stiffness method to locally-resonant structures has been directly addressed by Russillo and Failla [66], who presented closed-form formulae for computing the free vibration response of locally-resonant metamaterial plates by means of the Wittrick-William algorithm when the dynamic condensation of the degrees of freedom within the resonators is performed. Yet, no use of the dynamic-stiffness method has been made so far to investigate the dynamic response of metamaterial structures in time and frequency domain.

In this thesis, it is demonstrated that the dynamic-stiffness method is particularly suitable for computing the dynamic response and performing the wave propagation analysis of metamaterial structures very efficiently, as it allows implementing an ad hoc exact dynamic condensation of the degrees of freedom within the resonators with a significant model order

reduction, not obtainable by approximate finite element methods. Furthermore, in this thesis it is shown that the dynamic-stiffness method can be profitably employed to compute the dynamic response in the time domain by deriving appropriate orthogonality conditions for the modes of the structure under the assumption of both classical and non-classical damping and by employing the modal superposition principle. This is an important result, because the dynamic-stiffness method is typically implemented in the frequency domain and no study in existing literature has ever demonstrated its applicability in the time domain as well, for any structure including metamaterial ones.

The first chapter is devoted to introduce the dynamic-stiffness method for locally-resonant metamaterial beams, i.e. beams coupled with a periodic array of visco-elastic systems with one or more degrees of freedom. Upon deriving the closed-form solution of the governing equations of the metamaterial beam, the nodal generalized forces and displacements for a given frequency are exactly related by the dynamic-stiffness matrix. This relationship, together with the boundary conditions, provides the exact dynamic response of the beam in the frequency domain. Furthermore, for boundary conditions associated with the free vibrations problem, the dynamic-stiffness matrix represents a key ingredient in finding the natural frequencies and modes of the metamaterial beam by making use of specialized algorithms. Finally, the derivation of the orthogonality conditions associated with the modes of the metamaterial beam allows to decouple the governing equation leading to the modal response for arbitrary loads both in time and frequency domains.

The second chapter addresses an extension of the spectral dynamic-stiffness method, based on the analytical solution of the governing equation of Kirchhoff plates, to deal with locally-resonant metamaterial plates, i.e. systems of one or more plates coupled with periodic arrays of resonators with one or more degrees of freedom. The model lends itself to compute both the frequency-domain forced response and free vibrations response of locally-resonant metamaterial plates; the free vibration problem is tackled by providing an extension of the well-established Wittrick-William algorithm to compute the natural frequencies and modes of locally-resonant structures. Furthermore the derivation of orthogonality conditions pertinent to the modes of the plates only leads to the modal response for arbitrary loads in frequency and time domains.

In the third chapter, the exact dynamic-stiffness method is applied to

study the wave propagation in small-size metamaterial structures, namely planar microlattices. The dispersion curves of microlattices, modelled as an ensemble of stress-driven nonlocal Rayleigh beams, are calculated by solving the exact nonlinear eigenproblem that arises from the application of the Bloch's theorem to the equilibrium equations involving the dynamic-stiffness matrix of a unit cell. This procedure serves as a benchmark for validating the finite-element approximation of the equilibrium equations obtained by deriving appropriate shape functions from the exact static equilibrium equations.

In each Chapter, a detailed description of the proposed dynamic-stiffness methods is provided, along with the main novelties introduced. The conclusions of the thesis are drawn in a final Section. The lists of symbols for each chapter are reported in Appendix.

LOCALLY-RESONANT METAMATERIAL BEAMS

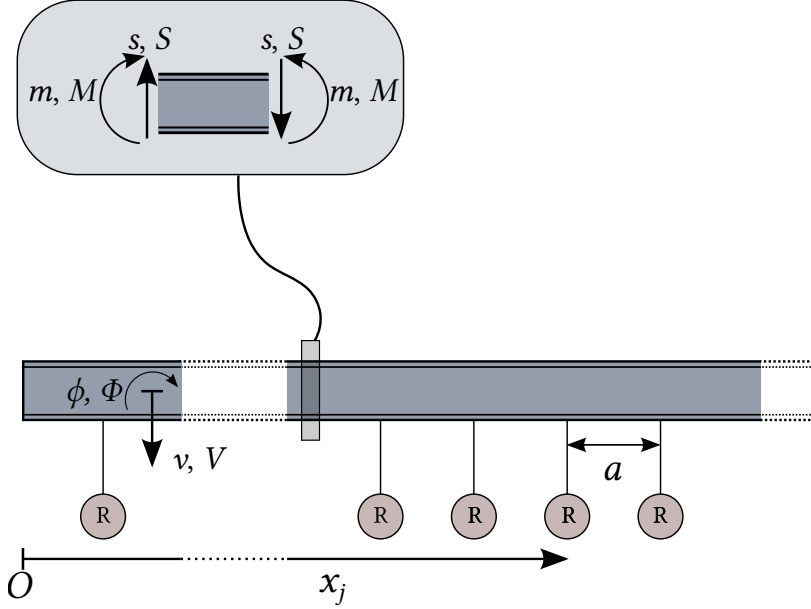
This chapter addresses the formulation of a reduced-order dynamic-stiffness model for locally-resonant metamaterial beams. Upon performing the exact dynamic condensation of the degrees of freedom within each resonator, orthogonality conditions for the modes of the beam only are retrieved. By means of the modal superposition principle, the dynamic response of the reduced-order model both in time and frequency domain is computed in analytical closed form.

1.1 Problem under study

Beams endowed with periodically attached arrays of resonators, i.e. locally-resonant metamaterial beams, represent an innovative structural typology that exhibits remarkable wave attenuation properties. Locally-resonant metamaterial beams can be modelled as continuous-discrete systems, where a continuous Euler-Bernoulli or Timoshenko beam is coupled with a periodic array of resonators, that is single- or multi-degrees-of-freedom mass-spring-dashpot systems as the system depicted in Figure 1.1, being the generic attached resonator symbolically represented with a circled “R”.

In the following Sections, closed analytical formulae for computing the frequency- and time-domain responses will be introduced. First, the frequency-domain response is retrieved by building the exact dynamic-stiffness matrix of the locally-resonant beam; the time-domain response is obtained by first deriving orthogonality conditions for a reduced-order model of the beam not involving the degrees of freedom of the resonators and by using the complex modal superposition principle in order to find the modal impulse response function. Consequently, the time-response under any arbitrary load can be straightforwardly obtained by means of the Duhamel’s integral.

Figure 1.1: Locally-resonant metamaterial beam.



1.2 Governing equations

The locally-resonant beam in Fig. 1.1 is, for generality, modelled as a Timoshenko beam coupled with an array of N_r resonators placed at $x_h = ha$, with $h = 1, \dots, N_r$, where a is the relative distance between two consecutive resonators. The governing equations can be concisely written in operator form as follows:

$$\mathcal{L}\mathbf{v}(x, t) - \mathcal{M}\ddot{\mathbf{v}}(x, t) + \mathcal{R}(x, t) + \mathbf{p}(x, t) = \mathbf{0} \quad (1.1)$$

where the vector $\mathbf{v} = [v \ \phi]^T$ collects the deflection (positive downward) $v = v(x, t)$ and the rotation (positive counterclockwise) $\phi = \phi(x, t)$ of the cross section, the vector $\mathbf{p} = [p_v \ p_\phi]^T$ collects the transversal $p_v = p_v(x, t)$ and rotational $p_\phi = p_\phi(x, t)$ dynamic loads. The operators in Eq. (1.1) are defined as

$$\mathcal{L} = \begin{bmatrix} GA \frac{\partial^2}{\partial x^2} & GA \frac{\partial}{\partial x} \\ -GA \frac{\partial}{\partial x} & -GA + EI \frac{\partial^2}{\partial x^2} \end{bmatrix}; \quad \mathcal{M} = \begin{bmatrix} \rho A & 0 \\ 0 & \rho I \end{bmatrix}; \quad (1.2)$$

$$\mathcal{R}(x, t) = \begin{bmatrix} \sum_{h=1}^{N_r} r_h(t) \delta(x - x_h) \\ 0 \end{bmatrix}$$

where \mathcal{L} is the stiffness operator, \mathcal{M} the mass operator and $\mathcal{R}(x, t)$ the operator associated with the reactions of the resonators; the bar in Eq. (1.2) indicates the generalized derivative and the symbol $\delta(x - x_h)$ denotes the Dirac's delta; $r_h = r_h(t)$ expresses the reaction of the h^{th} resonator at $x_h = ha$.

Assuming that the solution of Eq. (1.1) varies harmonically in time, the vibration response can be written as

$$\mathbf{y} = \mathbf{Y}e^{i\omega t}; \quad \mathbf{u}_h = \mathbf{U}_he^{i\omega t} \quad (1.3)$$

where $\mathbf{y} = \mathbf{y}(x, t) = [v \ \phi \ m \ s]^T$ and $\mathbf{Y} = [V \ \Phi \ M \ S]^T$ collect the response variables of the beam, i.e. deflection (v, V), rotation (ϕ, Φ), shear-force (s, S) and bending moment (m, M) in time and frequency domains, respectively. Vectors $\mathbf{u}_h = \mathbf{u}_h(t) = [u_h^{(1)} \ u_h^{(2)} \ \dots \ u_h^{(n_r)}]^T$ and $\mathbf{U}_h = [U_h^{(1)} \ U_h^{(2)} \ \dots \ U_h^{(n_r)}]^T$ collect the displacements of the n_r masses of the resonator applied at $x = x_h$ in time and frequency domains, respectively. It is noticed that Eq. (1.3) is both a representation of the frequency response function under a harmonic load of frequency ω , i.e. $\mathbf{Y} = \mathbf{Y}(x, \omega)$ and $\mathbf{U}_h = \mathbf{U}_h(\omega)$, and of the free-vibration response, since for each eigenvalue $\omega = \omega_n$, $\mathbf{Y}_n = \mathbf{Y}(x, \omega_n)$ and $\mathbf{U}_{h,n} = \mathbf{U}_h(\omega_n)$ represent the corresponding eigenfunctions.

*Frequency-domain
response representa-
tion*

1.3 Dynamic-stiffness method

Consider the free-vibration problem of the beam in Fig. 1.1. The dynamic response is in this case represented by Eq. (1.3) and Eq. (1.1) follows the governing equation for free vibration of the LR beam in Fig. 1.1.

$$\mathcal{L}\mathbf{V} + \omega^2\mathcal{M}\mathbf{V}(x, \omega) + \mathcal{R}(x, \omega) = \mathbf{0} \quad (1.4)$$

where $\mathbf{V} = [V \ \Phi]^T$ and the operator $\mathcal{R}(x, \omega)$ defined as

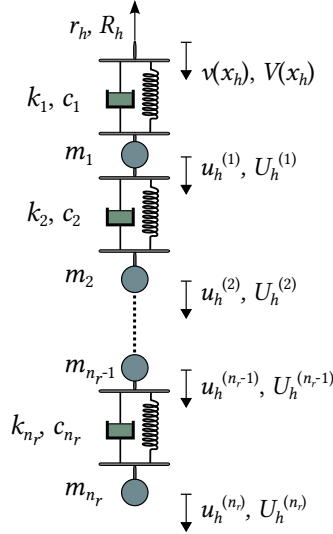
$$\mathcal{R}(x, \omega) = \begin{bmatrix} \sum_{h=1}^{N_r} R_h(\omega)\delta(x - x_h) \\ 0 \end{bmatrix} \quad (1.5)$$

the symbol R_h denotes the reaction force of the h^{th} resonator in the frequency-domain

$$R_h = -\kappa_{eq}(\omega)V(x_h) \quad (1.6)$$

In Eq. (1.6), $\kappa_{eq}(\omega)$ denotes the frequency-dependent dynamic stiffness of the resonator, which can be obtained by exact dynamic condensation of the resonator's equilibrium equations in the frequency domain. In order to illustrate the general procedure, consider for simplicity the resonator in Fig. 1.2.

Figure 1.2: Mass-spring-dashpot chain consisting of N_r resonators attached at $x = x_h$.



The equilibrium in the frequency domain is

$$\mathbf{D}_r(\omega) \begin{bmatrix} V(x_h) \\ \mathbf{U}_h \end{bmatrix} = (\mathbf{K}_r + i\omega\mathbf{C}_r - \omega^2\mathbf{M}_r) \begin{bmatrix} V(x_h) \\ \mathbf{U}_h \end{bmatrix} = \begin{bmatrix} R_h \\ \mathbf{0} \end{bmatrix} \quad (1.7)$$

In Eq. (1.7), \mathbf{K}_r , \mathbf{C}_r and \mathbf{M}_r denotes the stiffness, damping and mass matrix of the resonator, respectively. The dynamic-stiffness matrix \mathbf{D}_r can be further partitioned as follows:

$$\begin{bmatrix} D_r^{[vv]} & \mathbf{d}_r^{[vu]\text{T}} \\ \mathbf{d}_r^{[uv]} & \mathbf{D}_r^{[uu]} \end{bmatrix} \begin{bmatrix} V(x_h) \\ \mathbf{U}_h \end{bmatrix} = \begin{bmatrix} R_h \\ \mathbf{0} \end{bmatrix} \quad (1.8)$$

where the subscript v and u are respectively associated with the deflection of the resonator application point and the DOFs within the resonator. Eq. (1.8) gives the relation between the reaction force exerted by the resonator R_h on the beam and the displacement of its attachment point $V(x_h)$

$$R_h = \left(D_r^{[vv]} - \mathbf{d}_r^{[vu]\text{T}} \mathbf{D}_r^{[uu]} \mathbf{d}_r^{[uv]} \right) V(x_h) \quad (1.9)$$

A comparison with Eq. (1.6) provides the frequency-dependent dynamic stiffness $\kappa_{eq}(\omega)$

$$\kappa_{eq}(\omega) = \mathbf{d}_r^{[vu]T} \mathbf{D}_r^{[uu]} \mathbf{d}_r^{[uv]} - D_r^{[vv]} \quad (1.10)$$

1.3.1 Dynamic-stiffness matrix of the LR Timoshenko beam

Eq. (1.4) serves as basis for deriving the dynamic-stiffness matrix of the locally-resonant Timoshenko beam. The first step is finding a closed-form solution of Eq. (1.4), which can be reduced to a fourth order ordinary differential equation satisfied by both V and Φ

$$\frac{d^4 Z}{dx^4} + p_1 \frac{d^2 Z}{dx^2} + p_2 Z + p_3 = 0 \quad (1.11)$$

where Z may denote either the deflection V or the rotation Φ ; p_1 , p_2 and p_3 are defined as

$$p_1 = \left(\frac{\rho EI \omega^2}{G} + \rho I \omega^2 \right) / EI \quad (1.12)$$

$$p_2 = \left(\frac{\rho^2 I \omega^4}{G} - \rho A \omega^2 \right) / EI \quad (1.13)$$

$$p_3 = \begin{cases} -\frac{EI}{GA} \frac{\bar{d}^2 q}{dx^2} - \left(\frac{\rho I \omega^2}{GA} - 1 \right) q & \text{if } Z = V \\ -\frac{\bar{d} q}{dx} & \text{if } Z = \Phi \end{cases} \quad (1.14)$$

The solution of Eq. (1.11) is readily obtained in closed-form

$$Z(x) = Z_{om}(x) + \sum_{h=1}^{N_r} R_h J_{Z,h}(x) \quad (1.15)$$

being Z_{om} the solution of the homogeneous differential equation associated with Eq. (1.11), i.e.

$$Z_{om}(x) = \sum_{i=1}^4 c_i \alpha_i e^{\lambda_i x} \quad (1.16)$$

where c_i are integration constants, λ_i are the roots of the characteristic polynomial

$$\lambda_{1,2} = \mp \left(\left(-p_1 - \sqrt{p_1^2 - 4p_2} \right) / 2 \right)^{1/2} \quad (1.17)$$

$$\lambda_{3,4} = \mp \left(\left(-p_1 + \sqrt{p_1^2 - 4p_2} \right) / 2 \right)^{1/2} \quad (1.18)$$

$$(1.19)$$

being q the first component of $\mathcal{R}(x, \omega)$ in Eq. (1.5), i.e.

$$q(x, \omega) = \sum_{h=1}^{N_f} R_h(\omega) \delta(x - x_h) \quad (1.20)$$

Furthermore the coefficients α_i in Eq. (1.16) are given as

$$\alpha_i = \begin{cases} 1 & \text{if } Z = \Phi \\ -\frac{GA\lambda_i}{\rho A\omega^2 + GA\lambda_i^2} & \text{if } Z = V \end{cases} \quad (1.21)$$

Furthermore, $J_{Z,h}(x) = J_Z(x, x_h)$ in Eq. (1.15) the particular integral of Eq. (1.11) associated with the Dirac's delta $\delta(x - x_h)$, obtained by the inverse Laplace transform of Eq. (1.11). In particular $J_V(x, x_j)$ is given as

$$J_V(x, x_j) = -(\sqrt{2}GA\Sigma_1)^{-1} [B \sinh(C(x - x_j)) + D \sinh(E(x - x_j))] \mathcal{H}(x - x_j) \quad (1.22)$$

where B, C, D and E are given by

$$\begin{aligned} B &= (\sqrt{2}C)^{-1} [\Sigma_1 + \Sigma_2 - 2(GA)^2] & C &= ((\Sigma_1 - \Sigma_3) / (2EI GA))^{1/2} \\ D &= -(\sqrt{2}C)^{-1} [\Sigma_1 - \Sigma_2 + 2(GA)^2] & E &= (-(\Sigma_1 + \Sigma_3) / (2EI GA))^{1/2} \end{aligned} \quad (1.23)$$

being Σ_1, Σ_2 and Σ_3 defined as

$$\begin{aligned} \Sigma_1 &= \left[(EI)^2 (\rho A)^2 \omega^4 + 2EIGA\rho A\omega^2 (2GA - I\rho\omega^2) + (GA)^2 I^2 \rho^2 \omega^4 \right]^{1/2} \\ \Sigma_2 &= GAI\rho\omega^2 - EI\rho A\omega^2 & \Sigma_3 &= GAI\rho\omega^2 + EI\rho A\omega^2 \end{aligned} \quad (1.24)$$

being $\mathcal{H}(x)$ the unit-step function defined as

$$\mathcal{H}(x) = \begin{cases} 1 & \text{if } x > 0 \\ 0 & \text{if } x < 0 \end{cases} \quad (1.25)$$

Also, $J_\Phi(x, x_j)$ is:

$$J_\Phi(x, x_j) = -GAY_1^{-1} \{ \cosh[S_1(x - x_j)] - \cosh[S_2(x - x_j)] \} \mathcal{H}(x - x_j) \quad (1.26)$$

being S_1 and S_2 defined as

$$S_1 = ((Y_1 - Y_2)/(2EI GA))^{1/2} \quad S_2 = (-(Y_1 + Y_2)/(2EI GA))^{1/2} \quad (1.27)$$

where Y_1 and Y_2 read

$$\begin{aligned} Y_1 &= \left\{ \rho\omega^2 \left[(AEI)^2 \rho\omega^2 + 2AEIGA (2GA - I\rho\omega^2) \right] + (GA I)^2 \rho\omega^2 \right\}^{1/2} \\ Y_2 &= AEI\rho\omega^2 + GAI\rho\omega^2 \end{aligned} \quad (1.28)$$

Now, the FRF vector $\mathbf{Y}(x, \omega)$ can be concisely written as follows

$$\mathbf{Y}(x, \omega) = \mathbf{\Omega}(x, \omega)\mathbf{c} + \mathbf{R}(x)\mathbf{\Lambda}(\omega) \quad (1.29)$$

where the matrix \mathbf{R} is given by

$$\mathbf{R}(x) = \begin{bmatrix} \mathbf{J}(x, x_1) & \dots & \mathbf{J}(x, x_{N_r}) \end{bmatrix} \quad (1.30)$$

being $\mathbf{J}(x, x_h)$ defined as

$$\mathbf{J}(x, x_h) = \begin{bmatrix} J_V(x, x_h) \\ J_\Phi(x, x_h) \\ J_T(x, x_h) \\ J_M(x, x_h) \end{bmatrix} \quad (1.31)$$

with:

$$J_T(x, x_h) = GA \left(\frac{\bar{d}J_V}{dx} + J_\Phi \right); \quad J_M(x, x_h) = EI \frac{\bar{d}J_\Phi}{dx} \quad (1.32)$$

Making use of Eq. (1.15) with $Z = V$ for $V(x_h)$ in Eq. (1.6) it is observed that every reaction force R_h depends only on the four integration constants

c_h and on the reaction forces R_k at $x_k < x_h$. As a consequence the reaction forces R_h can be expressed in terms of the integration constants c_i and the vector Λ in Eq. (1.29), collecting the unknown reaction forces R_h of the resonators, satisfies the following linear system

$$\Lambda = \Phi_{\Omega} \mathbf{c} + \Phi_J \Lambda \quad (1.33)$$

where Φ_{Ω} is matrix whose j^{th} row is the first row of the matrix Ω evaluated at x_h , i.e. $\Omega_1(x_h)$, hence

$$\Phi_{\Omega} = -k_{eq}(\omega) \begin{bmatrix} \Omega_1(x_1) \\ \vdots \\ \Omega_1(x_{N_r}) \end{bmatrix} \quad (1.34)$$

In Eq. (1.33), Φ_J is the strict lower triangular matrix

$$\Phi_J = -k_{eq}(\omega) \begin{bmatrix} 0 & 0 & \dots & 0 \\ J_V(x_2, x_1) & 0 & \dots & 0 \\ \vdots & \ddots & & \vdots \\ J_V(x_{N_r}, x_1) & \dots & J_V(x_{N_r}, x_{N_r-1}) & 0 \end{bmatrix} \quad (1.35)$$

The solution of Eq. (1.33) is given by

$$\Lambda = (\mathbf{I} - \Phi_J)^{-1} \Phi_{\Omega} \mathbf{c} \quad (1.36)$$

where the inverse matrix $(\mathbf{I} - \Phi_J)^{-1}$ can be calculated in closed form as:

$$(\mathbf{I} - \Phi_J)^{-1} = \sum_{h=0}^{N_r-1} \Phi_J^h \quad (1.37)$$

Replacing Eq. (1.33) for Λ in Eq. (1.29) leads to

$$\mathbf{Y}(x, \omega) = \mathbf{W}(x, \omega) \mathbf{c} \quad (1.38)$$

where \mathbf{W} is a 4×4 matrix given as

$$\mathbf{W}(x, \omega) = \Omega(x, \omega) + \mathbf{R}(x)(\mathbf{I} - \Phi_J)^{-1} \Phi_{\Omega} \quad (1.39)$$

Consider now the Timoshenko beam in Figure 1.3. In order to build a general relation between the nodal displacements and forces, appropriate boundary conditions (BCs) must be enforced to the solutions in Eqs. (1.38). The deflections V and rotations Φ satisfy the general boundary conditions

$$V(0) = V_1 \quad \Phi(0) = \Phi_1 \quad V(L) = V_2 \quad \Phi(L) = \Phi_2 \quad (1.40)$$

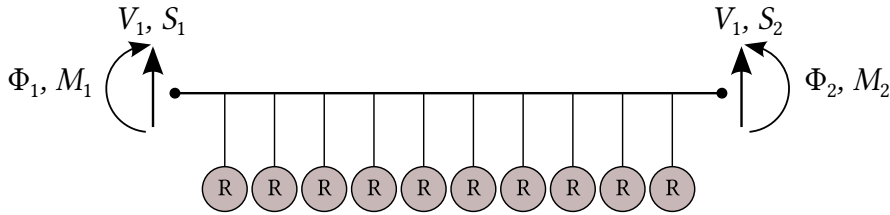


Figure 1.3: Boundary conditions for generalized displacements and forces.

Likewise the shear forces S and bending moments M need to satisfy the following boundary conditions:

$$S(0) = -S_1 \quad M(0) = M_1 \quad S(L) = S_1 \quad M(L) = -M_2 \quad (1.41)$$

Making use of Eq. (1.38), Eqs. (1.40)-(1.41) yields

$$\mathbf{u} = \mathbf{A}\mathbf{c} \quad (1.42)$$

$$\mathbf{f} = \mathbf{B}\mathbf{c} \quad (1.43)$$

being $\mathbf{u} = [V_1 \quad \Phi_1 \quad V_2 \quad \Phi_2]^T$ and $\mathbf{f} = [S_1 \quad M_1 \quad S_2 \quad M_2]^T$ the generalized nodal displacement and forces of a Timoshenko beam, respectively. Furthermore, \mathbf{A} and \mathbf{B} are defined as

$$\mathbf{A} = \begin{bmatrix} \alpha_1 & \alpha_2 & \alpha_3 & \alpha_4 \\ 1 & 1 & 1 & 1 \\ \alpha_1 e^{\lambda_1 L} & \alpha_2 e^{\lambda_2 L} & \alpha_3 e^{\lambda_3 L} & \alpha_4 e^{\lambda_4 L} \\ e^{\lambda_1 L} & e^{\lambda_2 L} & e^{\lambda_3 L} & e^{\lambda_4 L} \end{bmatrix} \quad (1.44)$$

$$\mathbf{B} = \begin{bmatrix} -GA(1 + \lambda_1 \alpha_1) & -GA(1 + \lambda_2 \alpha_2) & -GA(1 + \lambda_3 \alpha_3) & -GA(1 + \lambda_4 \alpha_4) \\ EI\lambda_1 & EI\lambda_2 & EI\lambda_3 & EI\lambda_4 \\ GA(1 + \lambda_1 \alpha_1) e^{\lambda_1 L} & GA(1 + \lambda_2 \alpha_2) e^{\lambda_2 L} & GA(1 + \lambda_3 \alpha_3) e^{\lambda_3 L} & GA(1 + \lambda_4 \alpha_4) e^{\lambda_4 L} \\ -EI\lambda_1 e^{\lambda_1 L} & -EI\lambda_2 e^{\lambda_2 L} & -EI\lambda_3 e^{\lambda_3 L} & -EI\lambda_4 e^{\lambda_4 L} \end{bmatrix} \quad (1.45)$$

Solving Eq. (1.42) with respect the vector \mathbf{c} and substituting the result in Eq. (1.43) leads to the relationship between the generalized nodal displacements and forces of the locally-resonant Timoshenko beam

$$\mathbf{f} = \mathbf{B}\mathbf{A}^{-1}\mathbf{u} = \mathbf{D}(\omega)\mathbf{u} \quad (1.46)$$

where $\mathbf{D}(\omega)$ is the frequency-dependent dynamic-stiffness matrix of the locally-resonant Timoshenko beam. It is noteworthy that the dynamic-stiffness matrix involved in Eq. (1.46) is a 4×4 matrix for any number

N_r of resonators and any number of DOFs within every resonator, furthermore it exactly related the nodal displacements and forces as it is based on the closed-form solution of the governing equations of the locally-resonant Timoshenko beam in the frequency-domain, consequently no discretization of the beam is needed unlike the finite element method.

Eq. (1.46) can be used to evaluate the transmittance of a cantilever beam, which is defined as $V(L)/V(0)$, i.e. the frequency response function at the free end for a unitary harmonic displacement of the clamped end. In particular, making use of the following partition

Transmittance

$$\begin{bmatrix} \mathbf{D}^{[uu]} & \mathbf{D}^{[uk]} \\ \mathbf{D}^{[ku]} & \mathbf{D}^{[kk]} \end{bmatrix} \begin{bmatrix} \mathbf{u}^{[u]} \\ \mathbf{u}^{[k]} \end{bmatrix} = \begin{bmatrix} \mathbf{0} \\ \mathbf{f}^{[u]} \end{bmatrix} \quad (1.47)$$

where $\mathbf{u}^{[u]}$ are the unknown nodal displacements and $\mathbf{u}^{[k]}$ the imposed nodal displacements. Eq. (1.47) leads to

$$\mathbf{u}^{[u]} = -\mathbf{D}^{[uu]}^{-1} \mathbf{D}^{[uk]} \mathbf{u}^{[k]} \quad (1.48)$$

Assuming $\mathbf{u}^{[k]} = [V(0) \ \Phi(0)]^T = [1 \ 0]^T$, the component of the vector $\mathbf{u}^{[u]}$, computed by means of Eq. (1.48), corresponding to the nodal displacement of the free edge $V(L)$ is the transmittance of the locally-resonant beam.

1.3.2 Free vibrations problem

As shown in the previous section, the frequency-domain equilibrium equation of the beam in Figure 1.1 is exactly described by the dynamic-stiffness matrix in Eq. (1.46). For free vibrations, the nodal forces are set equal to zero, i.e. $\mathbf{f} = \mathbf{0}$, and the following nonlinear eigenvalue problem arises:

$$\mathbf{D}(\omega)\mathbf{u} = \mathbf{0} \quad (1.49)$$

Due to the nonlinear nature of the eigenproblem in Eq. (1.49), it is not possible to make use of standard eigensolvers. For the locally-resonant sandwich beam under study, calculating the eigenvalues of Eq. (1.49) with the required accuracy and without missing anyone is a particularly challenging task because, as a result of local resonance, several modes are expected to exhibit eigenvalues close to each other. Here, for the first time, the issue is solved using a contour-integral method, recently introduced in the literature for nonlinear eigenvalue problems [1, 35, 71].

The contour-integral method requires the dynamic-stiffness matrix of the system $\mathbf{D}(\omega)$ in Eq. (1.49). Specifically, the fundamental steps to calculate the eigenvalues are [1, 35, 71]:

1. Selection of a circle $\Gamma = \gamma_0 + \rho_0 e^{i\theta}$ on the complex plane with center γ_0 , radius ρ_0 and $0 \leq \theta \leq 2\pi$.
2. Computation of two complex random probing matrices \mathbf{U} and \mathbf{V} with dimensions $n_0 \times L_0$, where n_0 is the size of the dynamic-stiffness matrix $\mathbf{D}(\omega)$ and L_0 is the assumed maximum algebraic multiplicity of the sought eigenvalues.
3. Computation of the shifted and scaled moments \mathbf{M}_k using N_0 -point trapezoidal rule:

$$\mathbf{S}_k = \frac{1}{N_0} \sum_{j=0}^{N_0-1} \left(\frac{\omega_j - \gamma_0}{\rho_0} \right)^{k+1} \mathbf{D}(\omega_j)^{-1} \mathbf{V}, \quad k = 0, 1, \dots, 2K-1$$

$$\mathbf{M}_k = \mathbf{U}^H \mathbf{S}_k$$

where K is the maximum order considered for the moment and \mathbf{U}^H is the Hermitian transpose of \mathbf{U} .

4. Construction of the Hankel matrices $\hat{\mathbf{H}}_{KL_0}$ and $\hat{\mathbf{H}}_{KL_0}^<$ $\in \mathbb{C}^{KL_0 \times KL_0}$ such that:

$$\hat{\mathbf{H}}_{KL_0} = [\mathbf{M}_{i+j-2}]_{i,j=1}^K, \quad \hat{\mathbf{H}}_{KL_0}^< = [\mathbf{M}_{i+j-1}]_{i,j=1}^K$$

5. Perform a singular value decomposition of $\hat{\mathbf{H}}_{KL_0}$.
6. Omit small singular value components $\sigma_i < \epsilon \cdot \max_i \sigma_i$, set \tilde{m} as the number of remaining singular value components ($\tilde{m} < KL_0$) and construct $\hat{\mathbf{H}}_{\tilde{m}}$ and $\hat{\mathbf{H}}_{\tilde{m}}^<$ extracting the principal submatrix with maximum index \tilde{m} from $\hat{\mathbf{H}}_{KL_0}$ and $\hat{\mathbf{H}}_{KL_0}^<$, that is

$$\hat{\mathbf{H}}_{\tilde{m}} = \hat{\mathbf{H}}_{KL_0}(1 : \tilde{m}, 1 : \tilde{m}); \quad \hat{\mathbf{H}}_{\tilde{m}}^< = \hat{\mathbf{H}}_{KL_0}^<(1 : \tilde{m}, 1 : \tilde{m})$$

7. Compute the eigenvalues ζ_j of the linear pencil:

$$\hat{\mathbf{H}}_{\tilde{m}}^< = \zeta \hat{\mathbf{H}}_{\tilde{m}}$$

8. Calculate the eigenvalues

$$\omega_j = \gamma_0 + \rho_0 \zeta_j, \quad j = 1, \dots, \tilde{m}$$

The algorithm converges to all the eigenvalues ω_k of Eq. (1.49) falling within the selected circle Γ , including multiple roots [1, 35, 71]. Circles of increasing radius and centred at the origin can be considered to explore the complex plane and calculate all the eigenvalues requested for practical purposes.

1.4 Modal analysis

The dynamic-stiffness method allows to exactly evaluate the frequency-domain response of a locally-resonant structure as shown in Section 1.3. On the other hand, the computation of the time-domain response is not directly obtainable from the dynamic-stiffness matrix, but a modal superposition method is required in order to decouple the governing equations of the locally-resonant Timoshenko beam.

1.4.1 Orthogonality conditions

The first step is to derive the pertinent orthogonality conditions for the complex modes of Eq. (1.4). Consider in particular Eq. (1.4) for the n^{th} mode

$$\mathcal{L}\mathbf{V}_n + \omega_n^2 \mathcal{M}\mathbf{V}_n + \mathcal{R}(x, \omega_n) = \mathbf{0} \quad (1.50)$$

Multiplying Eq. (1.50) for \mathbf{V}_m and integrating over the length of the beam

$$\int_0^L \mathbf{V}_m^T \mathcal{L}\mathbf{V}_n dx + \omega_n^2 \int_0^L \mathbf{V}_m^T \mathcal{M}\mathbf{V}_n dx - \sum_{h=1}^{N_r} V_m(x_h) \kappa_{eq}(\omega_n) V_n(x_h) = 0 \quad (1.51)$$

Repeating the same procedure by considering Eq. (1.4) for the m^{th} mode, multiplying for \mathbf{V}_n and taking advantage of the self-adjointness of the mass and stiffness operator lead to

$$\int_0^L \mathbf{V}_m^T \mathcal{L}\mathbf{V}_n dx + \omega_m^2 \int_0^L \mathbf{V}_m^T \mathcal{M}\mathbf{V}_n dx - \sum_{h=1}^{N_r} V_m(x_h) \kappa_{eq}(\omega_m) V_n(x_h) = 0 \quad (1.52)$$

The difference between Eq. (1.51) and Eq. (1.52) gives

$$(\omega_n^2 - \omega_m^2) \int_0^L \mathbf{V}_m^T \mathcal{M}\mathbf{V}_n dx + \sum_{h=1}^{N_r} V_m(x_h) \kappa_{eq}(\omega_m) - \kappa_{eq}(\omega_n) V_n(x_h) = 0 \quad (1.53)$$

After simple algebraic manipulations Eq. (1.53) yields the first orthogonality condition

$$\omega_n(\omega_n + \omega_m) \int_0^L \mathbf{V}_m^T \mathcal{M} \mathbf{V}_n dx + \omega_n \sum_{h=1}^{N_r} \frac{V_m(x_h) \kappa_{eq}(\omega_m) - \kappa_{eq}(\omega_n) V_m(x_h)}{\omega_n - \omega_m} = 0 \quad \text{First orthogonality condition} \quad (1.54)$$

Now, the difference between Eq. (1.51) multiplied by ω_m and Eq. (1.52) multiplied by ω_n provides the second orthogonality condition

$$\int_0^L \mathbf{V}_m^T \mathcal{L} \mathbf{V}_n dx = \omega_m \omega_n \int_0^L \mathbf{V}_m^T \mathcal{M} \mathbf{V}_n dx + \sum_{h=1}^{N_r} V_m(x_h) \mathcal{O}(\omega_n, \omega_m) V_n(x_h) \quad \text{Second orthogonality condition} \quad (1.55)$$

being $\mathcal{O}(\omega_n, \omega_m)$ defined as

$$\mathcal{O}(\omega_n, \omega_m) = \frac{\omega_n \kappa_{eq}(\omega_m) - \omega_m \kappa_{eq}(\omega_n)}{\omega_n - \omega_m} \quad (1.56)$$

It is noticed that the orthogonality conditions Eqs. (1.54)-(1.55) do not involve any of the degrees of freedom of the resonators and form the basis for the modal decoupling of the governing equation in Eq. (1.1) of the locally-resonant beam in Figure 1.1.

1.4.2 Complex modal analysis

Consider the locally-resonant beam in Figure 1.1 under an impulsive load, i.e. a load of the form $\mathbf{p}(x, t) = \mathbf{P}(x) \delta(t)$

$$\mathcal{L} \mathbf{v}(x, t) - \mathcal{M} \ddot{\mathbf{v}}(x, t) + \mathcal{R}(x, t) + \mathbf{P}(x) \delta(t) = \mathbf{0} \quad (1.57)$$

Using the modal superposition principle, the generalized displacements \mathbf{v} can be expanded in terms of eigenfunctions

$$\mathbf{v}(x, t) = \sum_{n=1}^{\infty} g_n(t) \mathbf{V}_n(x) \quad (1.58)$$

Substituting Eq. (1.58) in Eq. (1.57), premultiplying for the eigenvector \mathbf{V}_m and integrating over the beam domain yield

$$g_n \int_0^L \mathbf{V}_m^T \mathcal{L} \mathbf{V}_n dx - \ddot{g}_n \int_0^L \mathbf{V}_m^T \mathcal{M} \mathbf{V}_n dx - g_n \sum_{h=1}^{N_r} V_m(x_h) \kappa_{eq}(\omega_n) V_n(x_h) + \chi_m = 0$$

$$(1.59)$$

being

$$\chi_m = \int_0^L \mathbf{V}_m^T \mathbf{P}(x) \delta(t) dx \quad (1.60)$$

In view of the impulsive nature of the load, the modal coordinate $g_n(t)$ is such that $g_n(t) = \bar{g}_n e^{i\omega_n t}$ and $g_n(t) = \bar{g}_n^* e^{-i\omega_n t}$, being \bar{g}_n and \bar{g}_n^* complex conjugate pairs. As a consequence $\ddot{g}_n(t) = -\omega_n^2 g_n(t)$ and Eq. (1.59) can be further written as

$$\frac{\ddot{g}_n}{\omega_n^2} \left(\int_0^L \mathbf{V}_m^T \mathcal{L} \mathbf{V}_n dx + \omega_n^2 \int_0^L \mathbf{V}_m^T \mathcal{M} \mathbf{V}_n dx - \sum_{h=1}^{N_r} V_m(x_h) \kappa_{eq}(\omega_n) V_n(x_h) \right) = \chi_m \delta(t) \quad (1.61)$$

Substituting the second orthogonality condition Eq. (1.55) in Eq. (1.61) gives

$$\frac{\ddot{g}_n}{\omega_n^2} \left(\omega_n(\omega_n + \omega_m) \int_0^L \mathbf{V}_m^T \mathcal{M} \mathbf{V}_n dx + \omega_n \sum_{h=1}^{N_r} \frac{V_m(x_h) \kappa_{eq}(\omega_m) - \kappa_{eq}(\omega_n) V_n(x_h)}{\omega_n - \omega_m} \right) = \chi_m \delta(t) \quad (1.62)$$

Based on the first orthogonality condition Eq. (1.54), it is recognized that the term within parenthesis in Eq. (1.62) is equal to zero for $\omega_n \neq \omega_m$. On the other hand, for $\omega_n = \omega_m$, Eq. (1.62) becomes the following set of uncoupled differential equations

$$\Pi_n \ddot{g}_n = \chi_n \delta(t) \quad (1.63)$$

where

$$\Pi_n = 2 \int_0^L \mathbf{V}_n^T \mathcal{M} \mathbf{V}_n dx + \omega_n^{-2} \sum_{h=1}^{N_r} \mu(\omega_n) V_n^2(x_h) \quad (1.64)$$

being $\mu(\omega_n)$ defined as

$$\mu(\omega_n) = \lim_{\omega_m \rightarrow \omega_n} \omega_n \left(\frac{\kappa_{eq}(\omega_m) - \kappa_{eq}(\omega_n)}{\omega_n - \omega_m} \right) = -\omega_n \left. \frac{d\kappa_{eq}}{d\omega} \right|_{\omega=\omega_n} \quad (1.65)$$

Impulse response function Now, the impulse response function vector $\mathbf{h}(x, t)$ can be represented by

modal superposition

$$\mathbf{h}(x, t) = \sum_{n=1}^{\infty} g_n(t) \mathbf{Y}_n(x) \quad (1.66)$$

where $g_n(t) = \bar{g}_n e^{i\omega_n t}$ is a time-dependent complex function, ω_n and $\mathbf{Y}_n(x)$ are respectively the eigenvalue and eigenfunction vector associated with the n^{th} mode. Integrating (1.63) over the time yields \dot{g}_n and taking into account that $\dot{g}_n = i\omega_n g_n$, the coefficients \bar{g}_n are found

$$\bar{g}_n = \frac{\chi_n}{i\omega_n \Pi_n} \quad (1.67)$$

Since g_n in Eq. (1.66) may be $g_n = \bar{g}_n e^{i\omega_n t}$ or $g_n = \bar{g}_n^* e^{-i\omega_n t}$, the modal IRF vector of the n^{th} mode assumes the following form [58]:

$$\mathbf{h}_n(x, t) = \gamma_n(x) |\omega_n| w_n(t) + \boldsymbol{\psi}_n(x) \dot{w}_n(t) \quad (1.68)$$

where:

$$\gamma_n(x) = \zeta_n \boldsymbol{\psi}_n(x) - \sqrt{1 - \zeta_n^2} v_n(x) \quad (1.69)$$

$$\boldsymbol{\psi}_n(x) = 2 \operatorname{Re}[\bar{g}_n \mathbf{Y}_n(x)] \quad v_n(x) = 2 \operatorname{Im}[\bar{g}_n \mathbf{Y}_n(x)] \quad (1.70)$$

$$w_n(t) = \frac{1}{\omega_{Dn}} e^{-\zeta_n |\omega_n| t} \sin(\omega_{Dn} t); \quad \omega_{Dn} = |\omega_n| \sqrt{1 - \zeta_n^2} \quad (1.71)$$

being $\zeta_n = \operatorname{Im}(\omega_n) / |\omega_n|$ the modal damping ratio. Based again on ref. [58],

the corresponding vector $\mathbf{H}_n = [H_{v,n} \quad H_{\phi,n} \quad H_{m,n} \quad H_{s,n}]^T$ of modal FRFs *Frequency response function* is

$$\mathbf{H}_n(x, \omega) = \gamma_n(x) |\omega_n| H_n(\omega) + \boldsymbol{\psi}_n(x) i\omega_n H_n(\omega) \quad (1.72)$$

$$H_n(\omega) = \frac{1}{|\omega_n|^2 - \omega^2 + i2\zeta_n |\omega_n| \omega_n} \quad (1.73)$$

The beam IRF and FRF can be computed by truncating Eqs. (1.68)-(1.72) up to M modes

$$\mathbf{h}(x, t) \approx \sum_{n=1}^M \mathbf{h}_n(x, t) \quad (1.74)$$

$$\mathbf{H}(x, \omega) \approx \sum_{n=1}^M \mathbf{H}_n(x, \omega) \quad (1.75)$$

Eq. (1.74) and Eq. (1.75) hold for any number of resonators along the beam. Every modal contribution (1.68) and (1.72) is exact and readily obtainable in

analytical form once the eigenvalues are calculated. For practical purposes, a sufficient number of modes M shall be retained in Eq. (1.74) and Eq. (1.75) to obtain approximate yet accurate expressions of IRF and FRF. The IRF and FRF in every resonator follow from Eq. (1.74) and Eq.(1.75), provided that \mathbf{Y}_n is replaced with $\mathbf{U}_{h,n}$, i.e. the vector of eigenfunctions associated with the n^{th} mode for the response in the h^{th} resonator; $\mathbf{U}_{h,n}$ can be obtained from the deflection $V_n(x_h)$ of the application point.

Finally, it is shown that the modal frequency response function Eq. (1.75) can be used to calculate the transmittance of the beam, i.e. the frequency response function of the beam for a harmonic displacement at one of its ends. In the frequency domain a relative deflection V_g between adjacent sections at any abscissa $x = x_0$ can be modelled as

Modal transmittance

$$\frac{\bar{d}V}{dx} = \frac{S}{GA} - \Phi + V_g \delta(x - x_0) \quad (1.76)$$

The corresponding equations of motion are

$$GA \left[\frac{\bar{d}^2 V}{dx^2} + \frac{\bar{d}\Phi}{dx} - V_g \delta^{(1)}(x - x_0) \right] + \rho A \omega^2 V + \sum_{h=1}^{N_r} R_h \delta(x - x_h) = 0 \quad (1.77)$$

$$EI \frac{\bar{d}^2 \Phi}{dx^2} - GA \left[\frac{\bar{d}V}{dx} + \Phi - V_g \delta(x - x_0) \right] + \rho I \omega^2 \Phi = 0 \quad (1.78)$$

Consequently, the calculation of the transmittance by Eq. (1.75) involves considering the following term in Eq. (1.60)

$$\begin{aligned} \chi_m &= GA V_g \left[\int_0^L V_m(x) \delta^{(1)}(x - x_0) + \Phi_m(x) \delta(x - x_0) dx \right] \\ &= GA V_g \left[\Phi_m(x_0) - \frac{\bar{d}V_m(x_0)}{dx} \right] \end{aligned} \quad (1.79)$$

1.5 Wave propagation in a locally-resonant beam

The dispersion properties of an infinite locally-resonant beam gives an important insight for the characterization of the attenuation properties of a finite-length locally-resonant beam. The evaluation of the dispersion curves of a periodic medium can be performed by means of several techniques involving the Bloch's theorem. Here, the standard transfer matrix approach involving the dynamic-stiffness of the resonators is illustrated.

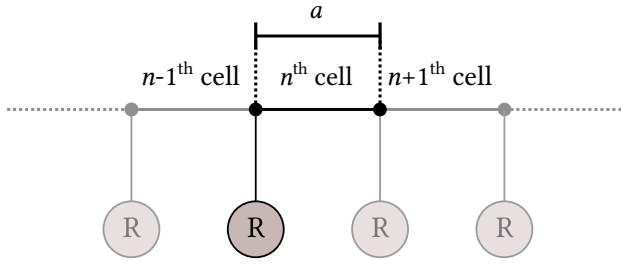


Figure 1.4: Highlighted n^{th} unit cell of a locally-resonant beam and adjacent cells.

The locally-resonant beam depicted in Figure 1.4 is divided in unit cells. The equilibrium equation in the frequency-domain of the n^{th} cell is given by

$$\mathcal{L}\mathbf{V} + \omega^2 \mathcal{M}\mathbf{V} = \mathbf{0} \quad (1.80)$$

The continuity condition between the response variables at the connection point between the $(n-1)^{\text{th}}$ and n^{th} cells reads with the natural boundary condition on the shear force

$$\begin{bmatrix} V^{[n]}(0) \\ \Phi^{[n]}(0) \\ S^{[n]}(0) - \kappa_{eq}(\omega)V^{[n]}(0) \\ M^{[n]}(0) \end{bmatrix} = \begin{bmatrix} V^{[n-1]}(a) \\ \Phi^{[n-1]}(a) \\ S^{[n-1]}(a) \\ M^{[n-1]}(a) \end{bmatrix} \quad (1.81)$$

Making use of the closed-form solution Eq. (1.16) of Eq. (1.80), Eq. (1.81) leads to the following identity [50]:

$$\mathbf{K}\mathbf{c}_n = \mathbf{H}\mathbf{c}_{n-1} \quad (1.82)$$

where \mathbf{K} and \mathbf{H} are given as

$$\mathbf{K} = \begin{bmatrix} \alpha_1 & \alpha_2 & \alpha_3 & \alpha_4 \\ 1 & 1 & 1 & 1 \\ 1 + \lambda_1\alpha_1 + F_1 & 1 + \lambda_2\alpha_2 + F_2 & 1 + \lambda_3\alpha_3 + F_3 & 1 + \lambda_4\alpha_4 + F_4 \\ \lambda_1 & \lambda_2 & \lambda_3 & \lambda_4 \end{bmatrix} \quad (1.83)$$

$$\mathbf{H} = \begin{bmatrix} \alpha_1 e^{\lambda_1 a} & \alpha_2 e^{\lambda_2 a} & \alpha_3 e^{\lambda_3 a} & \alpha_4 e^{\lambda_4 a} \\ e^{\lambda_1 a} & e^{\lambda_2 a} & e^{\lambda_3 a} & e^{\lambda_4 a} \\ (1 + \lambda_1\alpha_1)e^{\lambda_1 a} & (1 + \lambda_2\alpha_2)e^{\lambda_2 a} & (1 + \lambda_3\alpha_3)e^{\lambda_3 a} & (1 + \lambda_4\alpha_4)e^{\lambda_4 a} \\ \lambda_1 e^{\lambda_1 a} & \lambda_2 e^{\lambda_2 a} & \lambda_3 e^{\lambda_3 a} & \lambda_4 e^{\lambda_4 a} \end{bmatrix} \quad (1.84)$$

being $F_i = -\kappa_{eq}(\omega)\alpha_i/GA$ for $i = 1, 2, 3, 4$. Consequently, Eq. (1.82) yields

$$\mathbf{c}_n = \mathbf{T}(\omega)\mathbf{c}_{n-1} = \mathbf{K}^{-1}\mathbf{H}\mathbf{c}_{n-1} \quad (1.85)$$

Making use of the Bloch's theorem, $\mathbf{c}_n = e^{iqa}\mathbf{c}_{n-1}$ is substituted in Eq. (1.85) and the following standard generalized eigenvalue problem is obtained [50]

$$[\mathbf{T}(\omega) - \gamma\mathbf{I}]\mathbf{c}_{n-1} = \mathbf{0} \quad (1.86)$$

being $\gamma = e^{iqa}$. The dispersion curves $q = q(\omega)$ can be constructed by solving Eq. (1.86) for any frequency ω .

1.6 Numerical application

In order to verify the solution methods developed hitherto, a numerical application is considered in this Section. Since the Timoshenko beam is a suitable model for locally-resonant sandwich beams as shown in ref. [24],

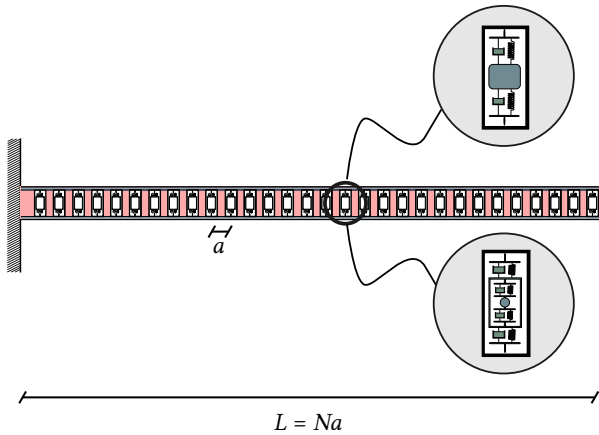


Figure 1.5: Cantilever locally-resonant sandwich beam hosting 1-DOF or 2-DOF resonators.

consider the cantilever locally-resonant sandwich beam in Figure 1.5. Based on ref. [24] the equivalent single-layer Timoshenko beam model:

$EI = 611 \text{ N/m}^{-2}$; $GA = 1.12 \times 10^4 \text{ N}$; $\rho A = 0.1248 \text{ kgm}^{-1}$;
 $\rho I = 1.69 \times 10^{-5} \text{ kg m}$; $a = 0.01 \text{ m}$ is the mutual distance between the resonators, $N = 30$ is the number of the resonators, $L = 0.30 \text{ m}$ is the total length of the beam.

Two cases are considered: (a) 1-DOF resonators with parameters $k_1 = 7415.74 \text{ Nm}^{-1}$, $c_1 = 0.05 \text{ Nsm}^{-1}$, $m_1 = 0.00117 \text{ kg}$; (b) 2-DOF resonators with parameters $k_1 = k_2 = 13361.97 \text{ Nm}^{-1}$; $c_1 = 0.05 \text{ Nsm}^{-1}$; $c_2 = 0.113 \text{ Nsm}^{-1}$; $m_1 = 0.0047 \text{ kg}$; $m_2 = 0.019 \text{ kg}$. The solution methods proposed in Sections 1.3-1.4 are applied to both cases. The modal expansions (1.74)-(1.75) for IRF and FRF require calculating the derivative (1.65) depending on the frequency-dependent stiffness (1.10) pertinent to the 1-DOF and 2-DOF resonators and available in the following forms:

1-DOF

$$\mu(\omega_k) = \frac{m_1 \omega_k^2 (-2c_1^2 \omega_k^2 - ic_1 m_1 \omega_k^3 + 4ic_1 k_1 \omega_k + 2k_1^2)}{(k_1 + ic_1 \omega_k + m_1 \omega_k^2)^2} \quad (1.87)$$

2-DOF

$$\mu(\omega_k) = \frac{\omega_k^2(c_1\Delta_1\omega_k^2 + 2c_1\Gamma_2k_1\omega_k + \Gamma_1k_1^2)}{(\gamma_1k_1 + \omega_k(\gamma_2\omega_k + ic_1\gamma_1))^2} \quad (1.88)$$

being

$$\begin{aligned} \Gamma_1 = & 4ik_2\omega_k(c_2(m_1 + m_2) + im_1m_2\omega_k) + \omega_k^2(-ic_2m_2(4m_1 + m_2)\omega_k \\ & - 2c_2^2(m_1 + m_2) + 2m_1m_2^2\omega_k^2) + 2k_2^2(m_1 + m_2) \end{aligned} \quad (1.89)$$

$$\begin{aligned} \Gamma_2 = & -4k_2\omega_k(c_2(m_1 + m_2) + im_1m_2\omega_k) + \omega_k^2(c_2m_2(4m_1 + m_2)\omega_k \\ & - 2ic_2^2(m_1 + m_2) + 2im_1m_2^2\omega_k^2) + 2ik_2^2(m_1 + m_2) \end{aligned} \quad (1.90)$$

$$\Delta_1 = c_1\Gamma_3 - i\omega_k\left(ic_2(m_1 + m_2)\omega_k + k_2(m_1 + m_2) - m_1m_2\omega_k^2\right) \quad (1.91)$$

$$\begin{aligned} \Gamma_3 = & 4k_2\omega_k(m_1m_2\omega_k - ic_2(m_1 + m_2)) + \omega_k^2(ic_2m_2(4m_1 + m_2)\omega_k \\ & + 2c_2^2(m_1 + m_2) - 2m_1m_2^2\omega_k^2) - 2k_2^2(m_1 + m_2) \end{aligned} \quad (1.92)$$

$$\gamma_1 = k_2 + \omega_k(-m_2\omega_k + ic_2) \quad (1.93)$$

$$\gamma_2 = -k_2(m_1 + m_2) + \omega_k(m_1m_2\omega_k - ic_2(m_1 + m_2)) \quad (1.94)$$

1.6.1 1-DOF resonators

For a first insight into the dynamics of the sandwich beam with 1-DOF resonators, the band gaps of the infinite beam with no damping are calculated using a standard transfer matrix approach as shown in Section 1.5. As expected given the fact that every resonator has one DOF, Figure 1.6 shows one band gap, where no real wave vectors are found. The band gap spans the frequency range 565-788 Hz.

Next, attention is focused on the cantilever beam and damping is considered within the resonators. The contour-integral algorithm in Section 1.3.2 is applied to calculate the first 131 complex eigenvalues, reported in Table 1.1. Several eigenvalues are close to each other, as a result of local resonance; remarkably, the algorithm proves capable of capturing also those differing by a few digits. Figure 1.7 shows the transmittance of the cantilever beam, as calculated using the exact frequency response (1.48) and the corresponding modal representation (1.75) including $M = 131$ modes, where the coefficients χ_k are given by Eq. (1.79); additionally, the individual modal contributions (1.72) are reported for $k = 1, 2, \dots, 31$, while the remaining ones up to $M = 131$ are omitted for clarity. The two solutions (1.38) and

Mode	Eigenvalue	Mode	Eigenvalue	Mode	Eigenvalue	Mode	Eigenvalue
1	967.680 ± 0.062i	34	11411.589 ± 25.056i	67	108291.328 ± 20.777i	100	208643.605 ± 20.733i
2	2498.070 ± 4.094i	35	14453.851 ± 23.306i	68	111421.313 ± 20.780i	101	211780.361 ± 20.728i
3	3177.911 ± 13.012i	36	17504.898 ± 22.413i	69	114556.083 ± 20.768i	102	214916.799 ± 20.723i
4	3367.718 ± 16.915i	37	20607.405 ± 21.905i	70	117690.008 ± 20.761i	103	218053.552 ± 20.719i
5	3445.411 ± 18.664i	38	23699.402 ± 21.572i	71	120825.715 ± 20.752i	104	221189.870 ± 20.715i
6	3483.342 ± 19.543i	39	26817.633 ± 21.357i	72	123960.628 ± 20.746i	105	224326.517 ± 20.712i
7	3505.011 ± 20.051i	40	29920.903 ± 21.175i	73	127096.642 ± 20.739i	106	227462.225 ± 20.704i
8	3518.398 ± 20.368i	41	33041.580 ± 21.038i	74	130231.990 ± 20.734i	107	230597.380 ± 20.682i
9	3527.317 ± 20.579i	42	36133.097 ± 20.791i	75	133368.169 ± 20.729i	108	233424.810 ± 2.526i
10	3533.517 ± 20.727i	43	39207.301 ± 20.081i	76	136503.753 ± 20.725i	109	233780.308 ± 18.256i
11	3538.019 ± 20.834i	44	41615.636 ± 8.516i	77	139640.041 ± 20.720i	110	236878.026 ± 20.686i
12	3541.376 ± 20.914i	45	42883.789 ± 14.665i	78	142775.746 ± 20.716i	111	240013.600 ± 20.697i
13	3543.950 ± 20.975i	46	45683.115 ± 20.384i	79	145912.108 ± 20.712i	112	243149.515 ± 20.699i
14	3545.959 ± 21.023i	47	48777.480 ± 20.690i	80	149047.825 ± 20.708i	113	246286.213 ± 20.698i
15	3547.558 ± 21.061i	48	51886.117 ± 20.764i	81	152184.207 ± 20.704i	114	249422.685 ± 20.696i
16	3548.845 ± 21.092i	49	55012.532 ± 20.766i	82	155319.733 ± 20.699i	115	252559.510 ± 20.694i
17	3549.894 ± 21.117i	50	58136.869 ± 20.764i	83	158455.939 ± 20.693i	116	255696.136 ± 20.692i
18	3550.757 ± 21.138i	51	61268.083 ± 20.751i	84	161590.364 ± 20.682i	117	258833.001 ± 20.689i
19	3551.472 ± 21.155i	52	64397.026 ± 20.740i	85	164723.935 ± 20.643i	118	261969.694 ± 20.685i
20	3552.068 ± 21.169i	53	67530.045 ± 20.726i	86	167628.273 ± 6.541i	119	265106.580 ± 20.680i
21	3552.565 ± 21.181i	54	70661.089 ± 20.712i	87	167974.147 ± 14.280i	120	268243.305 ± 20.674i
22	3552.981 ± 21.191i	55	73795.070 ± 20.696i	88	171010.497 ± 20.629i	121	271380.204 ± 20.664i
23	3553.329 ± 21.200i	56	76927.227 ± 20.678i	89	174144.441 ± 20.647i	122	274516.940 ± 20.647i
24	3553.617 ± 21.206i	57	80061.793 ± 20.656i	90	177279.215 ± 20.644i	123	277653.845 ± 20.609i
25	3553.854 ± 21.212i	58	83194.469 ± 20.624i	91	180415.506 ± 20.618i	124	280790.559 ± 20.420i
26	3554.046 ± 21.217i	59	86329.326 ± 20.574i	92	183551.381 ± 20.559i	125	283927.477 ± 20.983i
27	3554.198 ± 21.220i	60	89461.808 ± 20.463i	93	186687.811 ± 20.267i	126	287064.115 ± 20.794i
28	3554.312 ± 21.223i	61	92595.944 ± 19.948i	94	189824.457 ± 21.142i	127	290200.948 ± 20.755i
29	3554.439 ± 21.226i	62	95728.273 ± 21.431i	95	192960.973 ± 20.849i	128	293337.228 ± 20.735i
30	3554.392 ± 21.225i	63	98858.127 ± 20.857i	96	196097.302 ± 20.791i	129	296473.209 ± 20.713i
31	5094.551 ± 41.909i	64	101922.582 ± 18.719i	97	199233.997 ± 20.766i	130	299408.258 ± 3.362i
32	6076.198 ± 37.949i	65	102800.655 ± 2.539i	98	202370.416 ± 20.749i	131	299651.794 ± 17.409i
33	8561.842 ± 28.981i	66	105167.218 ± 20.683i	99	205507.151 ± 20.740i		

Table 1.1: Complex eigenvalues of the cantilever locally-resonant sandwich beam in Figure 1.5 with 1-DOF resonators.

Figure 1.6: Band gaps of the infinite sandwich beam in Figure 1.5 with 1-DOF resonators.

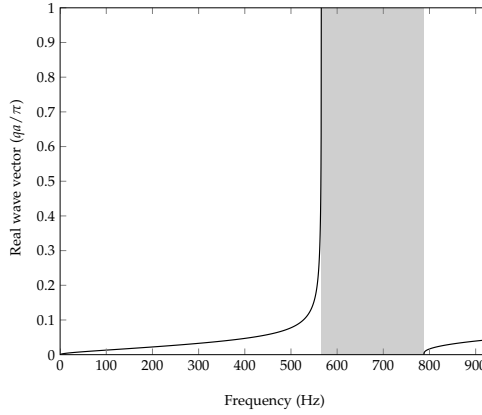
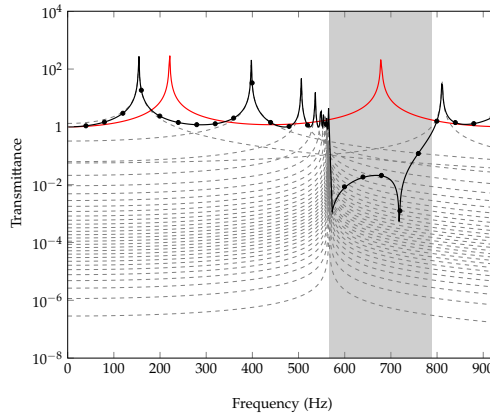


Figure 1.7: Transmittance of the cantilever locally-resonant sandwich beam in Figure 2 with 1-DOF resonators: exact response (1.38) (black continuous line); total modal response (1.75) for $M = 131$ (black dots); single modal responses (1.72) for $k = 1, \dots, 31$ (gray dashed lines); exact response without resonators (red continuous line).



(1.75) are in perfect agreement, substantiating the correctness of the two approaches proposed in this paper. The transmittance within the band gap is well lower than the transmittance over the remaining frequency domain, meaning that the wave attenuation properties of the infinite beam (see Figure 1.6) hold also for the finite beam. A further interesting observation is that the peaks of all individual modal contributions occur either below or above the band gap, i.e. there are no resonance modes within the band gap. For completeness, Figure 1.7 reports the transmittance of the beam without resonators, which exhibits a peak within the band gap well larger than the transmittance of the beam with resonators. Now, the interest is to calculate the FRF of the cantilever beam acted upon by a unit harmonic force applied at the free end. Figure 1.8a illustrates the FRF for the tip deflection over the frequency range 0-930 Hz, as computed using the exact solution (1.38) and

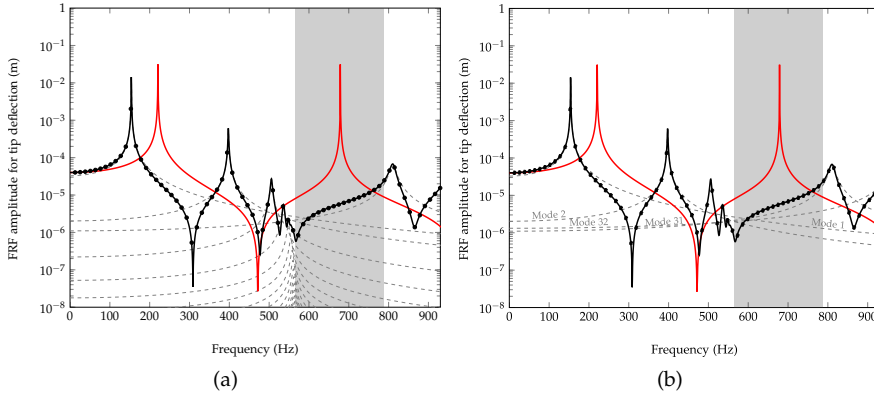


Figure 1.8: FRF for tip deflection of cantilever locally-resonant beam in Figure 2 with 1-DOF resonators, under a unit harmonic force applied at the free end: exact response (1.38) (black continuous line); total modal response (1.75) with $M = 131$ (black dots); single modal responses (1.72) (gray dashed lines); exact response without resonators (red continuous line); modal responses (1.72) are reported for $k = 1, \dots, 20$ and $k = 30, 31, 32$ (Fig. 1.8a) and $k = 1, 2, 31, 32$ (Fig. 1.8b).

the modal representation (1.75) for $M = 131$; again, the individual modal contributions (1.72) are reported for $k = 1, 2, \dots, 20$ and $k = 30, 31, 32$. The two solutions are in perfect agreement; for the frequency range considered in Figure 1.8, $M = 131$ modes are sufficient to provide a very accurate modal representation (1.75) of the exact solution (1.38).

Figure 1.8a shows also the FRF of the beam without resonators, showing that is generally larger than the FRF of the beam with resonators within the whole band gap, except for a limited frequency range 759-788 Hz, i.e. at the right end of the band gap. The inspection of the modal contributions suggests that this is essentially attributable to the contributions of modes 1 – 2 – 31 – 32, as highlighted in Figure 1.8b. For a further insight into this issue, the time response is investigated. Specifically, the closed analytical expression (1.74) for the IRF is used to calculate the tip deflection of the beam acted upon by a unit cosine force with frequency 780 Hz, applied at the free end. Figure 1.9a shows no significant changes in the response if more than $M = 50$ modes are included in Eq. (1.74) for the IRF. Further, consistently with the FRF in Figure 1.8, Figure 1.9b shows that the most significant contributions to the response are associated with the 1st, 2nd, 31th, 32th modes; indeed, due mainly to these contributions, the response of the beam with resonators attains almost the same order of magnitude of the response of the beam without resonators, as shown in Figure 1.9c. Notice that the insight gained into the modal contributions is a crucial information for design purposes because, e.g., once mass and stiffness of the resonators are calibrated, the damping coefficients might be selected so as to minimize the most significant modal contributions, i.e., in this case, those associated with 1st, 2nd, 31th, 32th modes.

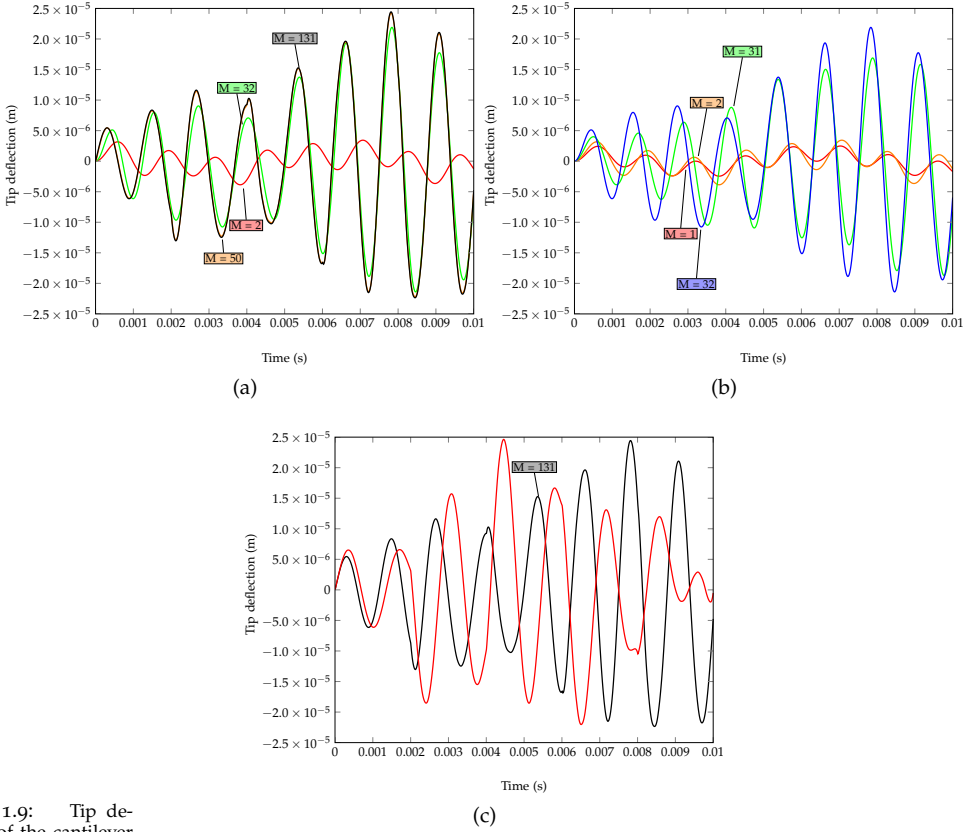


Figure 1.9: Tip deflection of the cantilever beam locally-resonant beam in Figure 1.5 with 1-DOF resonators, under a unit cosine force with frequency 780 Hz: (a) total response for increasing number of modes M in Eq. (1.74); (b) single modal response for most significant modes; (c) total response for $M = 131$ in Eq. (1.74) (black continuous line) and response of the beam without resonators (red continuous line) for $M = 131$.

This substantiates the interest in the proposed modal representation of the response, in both frequency and time domain.

1.6.2 2-DOF resonators

Now, consider the sandwich beam with 2-DOF resonators. The band gaps of the infinite beam without damping, calculated by the transfer matrix approach, are reported in Figure 1.10. As expected, there are two band gaps, over the frequency ranges 130-374 Hz and 553-849 Hz. For the finite beam with damping, the first 161 complex eigenvalues calculated by the contour-integral algorithm in Section 1.3.2 are reported in Table 1.2. Again, the algorithm proves capable of capturing several eigenvalues close to each other, some differing even by a few digits, as a result of local resonance.

For a further insight, transmittance and FRF for the tip deflection un-

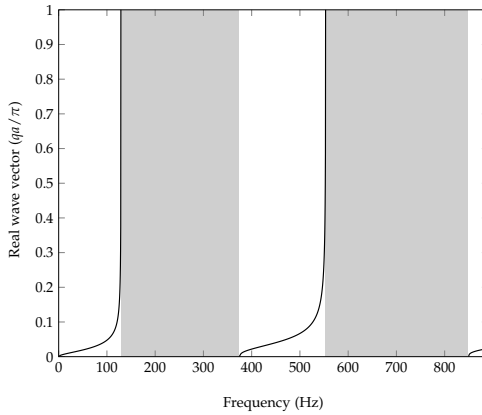


Figure 1.10: Band gaps of the infinite sandwich beam in Figure 1.5 with 2-DOF resonators.

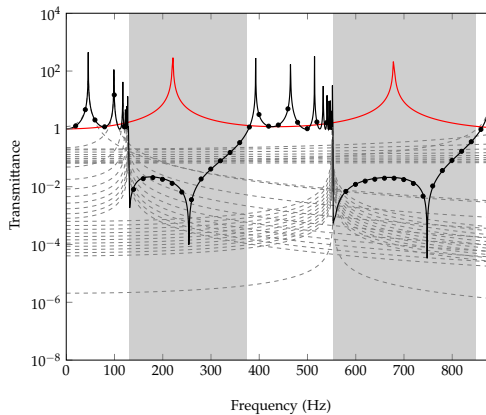


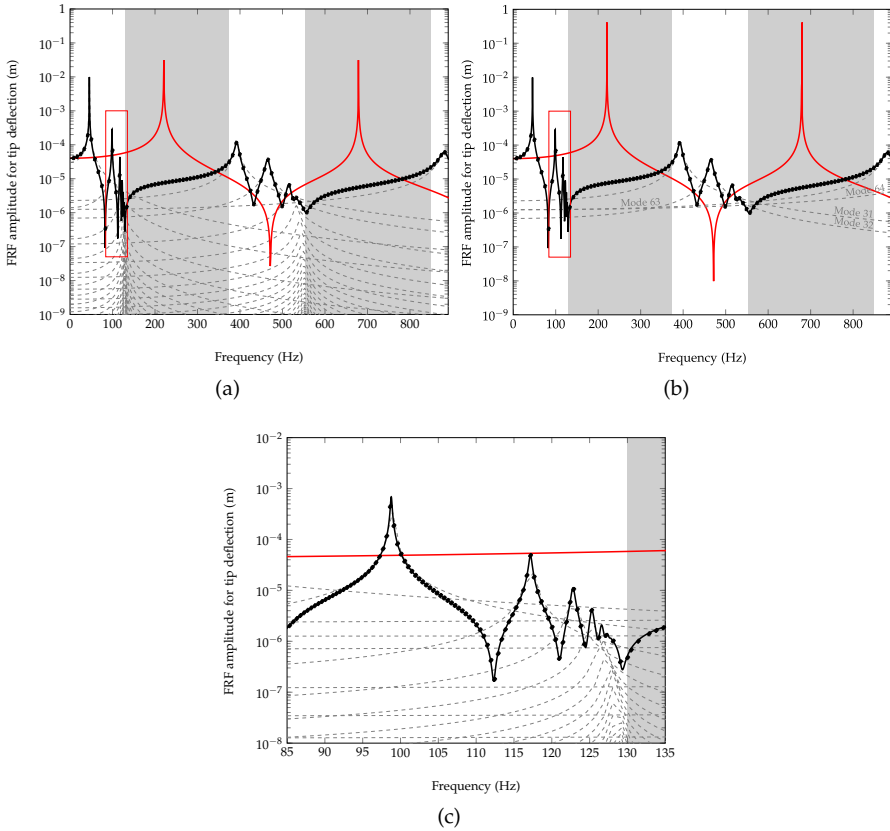
Figure 1.11: Transmittance of the cantilever locally-resonant sandwich beam in Figure 2 with 2-DOF resonators: exact response (1.38) (black continuous line); total modal response (1.75) for $M = 161$ (black dots); single modal responses (1.72) (gray dashed lines) for $k = 1, \dots, 10, k = 40, \dots, 50$ and $k = 60, \dots, 70$; exact response without resonators (red continuous line).

der a unit harmonic force at the free end are reported in Figure 1.11 and Figure 1.12, respectively. Again, the exact solution (1.48) and the modal expansion (1.75) are in perfect agreement, proving the correctness of the two approaches. In this case, the modal expansion (1.75) represents very accurately both the transmittance and the FRF with $M = 161$ over the frequency domain 0-890 Hz (see Figure 1.12a and zoomed view in Figure 1.12c). Further comments mirror those made for the beam with 1-DOF resonators, i.e.: the transmittance within the band gaps is a few orders of magnitude lower than the transmittance over the remaining frequency domain, meaning that the wave attenuation properties of the infinite beam hold also for the finite beam; there are no resonance modes within the two band gaps.

The FRF of the beam with resonators is generally lower than the corresponding one without resonators within the two band gaps, except for a

limited frequency range at the vicinity of the right end of the second band gap. Figure 1.12b shows that the most significant contributions to the FRF at the right end of the second bandgap are associated with modes 31-32-63-64. This result is confirmed by the time analysis of the tip deflection under a unit cosine force applied at the free end, with frequency 940 Hz, reported in Figure 1.13. Indeed, the response built using Eq. (1.74) for the IRF attains the same order of magnitude of the response of the beam without resonators due mainly to the contributions of these modes; on the other hand, no significant changes in the time response are noticed if more than $M = 70$ modes are included.

Figure 1.12: FRF for tip deflection of cantilever sandwich beam in Figure 1.5 with 2-DOF resonators, under a unit harmonic force applied at the free end: exact response (1.38) (black continuous line); total modal response (1.75) for $M = 161$ (black dots); single modal responses (1.72) (gray dashed lines); exact response without resonators (red continuous line); modal responses (1.72) are reported for $k = 1, \dots, 52$ and $k = 60, \dots, 64$ (Fig. 1.12a) and $k = 31, 32, 63, 64$ (Fig. 1.12b); a zoomed view is included (Fig. 1.12c).



Mode	Eigenvalue	Mode	Eigenvalue	Mode	Eigenvalue	Mode	Eigenvalue
1	286.280 ± 0.027i	42	3466.432 ± 38.350i	83	67602.459 ± 41.199i	124	189850.729 ± 42.944i
2	620.619 ± 0.632i	43	3468.384 ± 38.399i	84	70730.285 ± 41.172i	125	192986.582 ± 41.899i
3	736.251 ± 1.280i	44	3469.911 ± 38.437i	85	73861.305 ± 41.136i	126	196122.458 ± 41.691i
4	771.551 ± 1.552i	45	3471.128 ± 38.467i	86	76990.732 ± 41.089i	127	199258.737 ± 41.600i
5	787.217 ± 1.686i	46	3472.110 ± 38.491i	87	80122.759 ± 41.024i	128	202394.761 ± 41.545i
6	795.224 ± 1.757i	47	3472.912 ± 38.511i	88	83253.055 ± 40.924i	129	205531.118 ± 41.513i
7	799.919 ± 1.800i	48	3473.571 ± 38.528i	89	86385.636 ± 40.751i	130	208667.207 ± 41.488i
8	802.868 ± 1.827i	49	3474.118 ± 38.541i	90	89515.805 ± 40.352i	131	211803.611 ± 41.470i
9	804.854 ± 1.846i	50	3474.574 ± 38.553i	91	92646.501 ± 38.420i	132	214939.706 ± 41.454i
10	806.244 ± 1.859i	51	3474.956 ± 38.562i	92	95781.756 ± 44.114i	133	218076.128 ± 41.442i
11	807.260 ± 1.868i	52	3475.274 ± 38.570i	93	98908.259 ± 42.056i	134	221212.123 ± 41.430i
12	808.020 ± 1.876i	53	3475.541 ± 38.577i	94	101966.090 ± 37.151i	135	224348.457 ± 41.419i
13	808.604 ± 1.881i	54	3475.762 ± 38.582i	95	102806.610 ± 5.535i	136	227483.857 ± 41.401i
14	809.062 ± 1.886i	55	3475.944 ± 38.587i	96	105213.896 ± 41.472i	137	230618.697 ± 41.353i
15	809.426 ± 1.889i	56	3476.393 ± 38.598i	97	108336.858 ± 41.610i	138	233427.574 ± 4.545i
16	809.720 ± 1.892i	57	3476.357 ± 38.597i	98	111465.571 ± 41.591i	139	233798.678 ± 37.005i
17	809.960 ± 1.894i	58	3476.295 ± 38.595i	99	114599.106 ± 41.550i	140	236898.785 ± 41.357i
18	810.158 ± 1.896i	59	3476.207 ± 38.593i	100	117731.872 ± 41.522i	141	240034.101 ± 41.377i
19	810.322 ± 1.898i	60	3476.091 ± 38.590i	101	120866.478 ± 41.495i	142	243169.755 ± 41.377i
20	810.458 ± 1.899i	61	30083.321 ± 41.607i	102	124000.350 ± 41.475i	143	246306.196 ± 41.372i
21	810.572 ± 1.900i	62	33188.621 ± 41.451i	103	127135.375 ± 41.456i	144	249442.418 ± 41.366i
22	810.668 ± 1.901i	63	5537.644 ± 58.228i	104	130269.785 ± 41.442i	145	252578.998 ± 41.358i
23	810.747 ± 1.902i	64	6647.837 ± 53.665i	105	133405.068 ± 41.427i	146	255715.386 ± 41.350i
24	810.814 ± 1.902i	65	9073.851 ± 47.573i	106	136539.800 ± 41.415i	147	258852.019 ± 41.339i
25	810.868 ± 1.903i	66	11819.176 ± 44.797i	107	139675.274 ± 41.402i	148	261988.485 ± 41.327i
26	810.912 ± 1.903i	67	14783.101 ± 43.456i	108	142810.201 ± 41.392i	149	265125.149 ± 41.310i
27	810.947 ± 1.904i	68	17779.491 ± 42.718i	109	145945.818 ± 41.380i	150	268261.659 ± 41.287i
28	810.973 ± 1.904i	69	20842.056 ± 42.297i	110	149080.823 ± 41.369i	151	271398.349 ± 41.253i
29	810.992 ± 1.904i	70	23904.008 ± 41.994i	111	152216.521 ± 41.357i	152	274534.881 ± 41.192i
30	811.003 ± 1.904i	71	26998.851 ± 41.805i	112	155351.390 ± 41.344i	153	277671.594 ± 41.054i
31	2466.989 ± 23.532i	72	36266.575 ± 41.032i	113	158486.963 ± 41.328i	154	280808.160 ± 40.369i
32	2920.847 ± 27.657i	73	39326.373 ± 39.566i	114	161620.773 ± 41.300i	155	283944.735 ± 42.413i
33	3233.359 ± 33.001i	74	41661.862 ± 15.667i	115	164753.712 ± 41.215i	156	287081.233 ± 41.728i
34	3345.749 ± 35.461i	75	42965.366 ± 30.348i	116	167637.727 ± 11.615i	157	290217.891 ± 41.589i
35	3397.235 ± 36.666i	76	45787.637 ± 40.462i	117	167994.170 ± 29.950i	158	293353.991 ± 41.522i
36	3423.788 ± 37.305i	77	48876.968 ± 41.055i	118	171039.168 ± 41.172i	159	296489.787 ± 41.462i
37	3439.413 ± 37.685i	78	51980.110 ± 41.218i	119	174172.626 ± 41.192i	160	299411.374 ± 5.958i
38	3449.241 ± 37.926i	79	55101.302 ± 41.241i	120	177306.906 ± 41.164i	161	299665.134 ± 35.609i
39	3455.865 ± 38.089i	80	58220.947 ± 41.251i	121	180442.694 ± 41.071i		
40	3460.505 ± 38.204i	81	61347.886 ± 41.238i	122	183578.055 ± 40.860i		
41	3463.895 ± 38.287i	82	64472.968 ± 41.223i	123	186713.794 ± 39.818i		

Table 1.2: Complex eigenvalues of the cantilever locally-resonant sandwich beam in Figure 1.5 with 2-DOF resonators

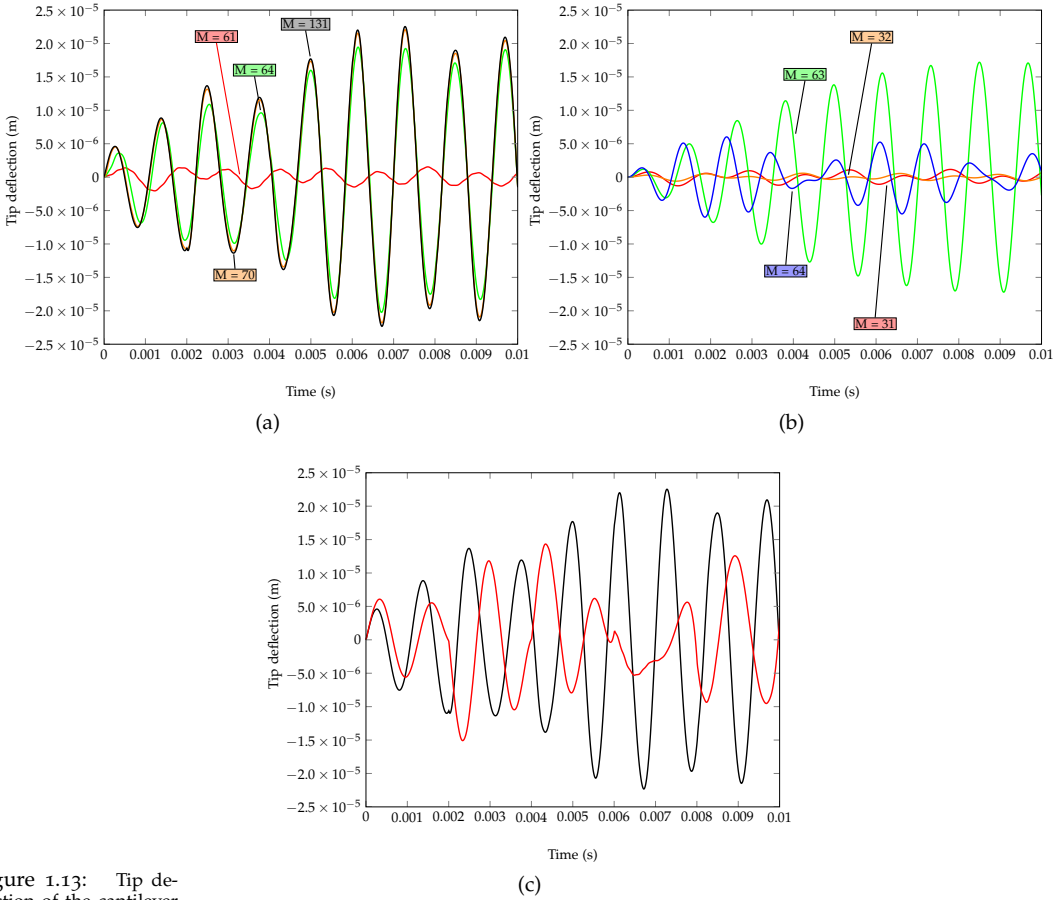


Figure 1.13: Tip deflection of the cantilever locally-resonant beam in Figure 1.5 for 2-DOF resonators, under a unit cosine force with frequency 830 Hz: (a) total response for increasing number of modes M in Eq. (1.74); (b) single modal response for most significant modes; (c) total response for $M = 161$ in Eq. (1.74) (black continuous line) and response of the beam without resonators (red continuous line) for $M = 161$.

1.7 Conclusions

In this chapter, a novel computational framework for computing the dynamic response of locally-resonant metamaterial beams, i.e. beams coupled with multi-DOF mass-spring-dashpot subsystems, has been presented. In particular, the following key contributions have been produced:

1. A novel closed form expression for the dynamic-stiffness matrix of a locally-resonant metamaterial beam in the frequency domain for an arbitrary number of resonators and degrees of freedom within each resonator. Since the solutions are derived from the closed form solution of the beam governing equation, thus the dynamic response in the frequency domain can be computed without introducing any approximation.
2. The contour-integral method is applied for the first time to solve the complex nonlinear eigenvalue problem arising from the equations of motion for free vibrations. The problem is notoriously challenging to solve because locally-resonant metamaterials beam exhibit several eigenvalues close to each other, as a result of local resonance.
3. Analytical expressions for computing the dynamic response of the locally-resonant metamaterial beam in the time domain based on the dynamic-stiffness method and on the modal analysis are derived.

The numerical applications confirms the accuracy and the efficiency of the proposed approach. Furthermore, since it is based on analytical solutions of the governing equations, the proposed framework is particularly useful for benchmarking purposes. Further studies may extend the proposed framework for computing the dynamic response of arbitrary periodic structures, like planar hierarchical lattice structures.

LOCALLY-RESONANT METAMATERIAL PLATES

The goal of this chapter is to formulate a spectral dynamic-stiffness model for locally-resonant metamaterial plates. The spectral dynamic-stiffness method and the exact dynamic condensation of the dynamic-stiffness matrices governing the equilibrium of the resonators provide a framework for the calculation of the natural frequencies and the corresponding undamped modes. The derivation of the orthogonality conditions for the modes of the reduced-order model leads to closed analytical solution of the modal response under arbitrary loads, both in time and frequency domains.

2.1 Introduction

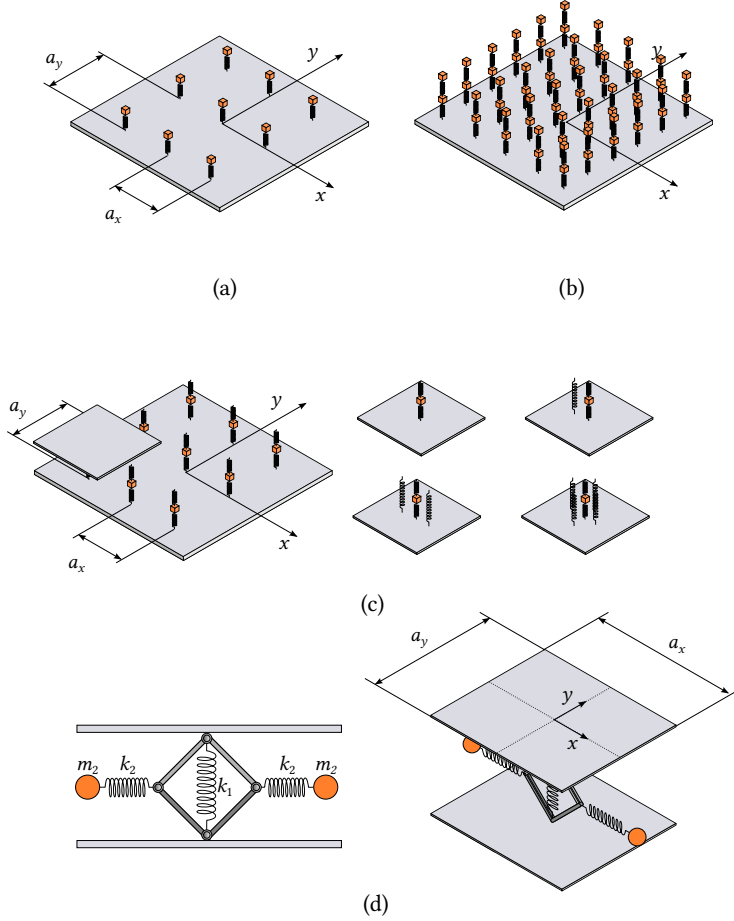
The dynamics of locally-resonant metamaterial plates such as the one reported in Fig. 2.1 is generally performed by means of FE codes, where the degrees of freedom within the resonators are necessarily taken into account. Here, a spectral dynamic-stiffness model based on the dynamic-stiffness method and the exact-dynamic condensation not involving the degrees of freedom within the resonator is proposed. For generality, the proposed model is presented for an assembly of n_p plates coupled by arrays of resonators. Every resonator exerts transverse forces on two consecutive plates by being activated by the deflections of its attachment points

2.2 Reduced-order model

As basis for deriving the reduced-order model of the system in Figure 2.2, the equations governing its free vibrations are considered. First, assume that the vector collecting the deflection in every plate depends harmonically on time, i.e. $\mathbf{w}(\mathbf{x}, t) = \mathbf{W}(\mathbf{x})e^{i\omega t}$, where $\mathbf{W}(\mathbf{x}) = [W^{(1)} \ \dots \ W^{(n_p)}]^T$ collects the frequency-dependent deflections in every plate, ω is the frequency and $\mathbf{x} = (x, y)$. The equilibrium equations in the frequency domain

Free-vibration problem

Figure 2.1: Locally-resonant metamaterial plates: (a) single plate with 1-DOF mass-spring resonators [89]; (b) single plate with 2-DOF mass-spring resonators [56]; (c) two plates coupled by different types of 1-DOF mass-spring resonators [63]; (d) two plates coupled by 1-DOF mass-spring-truss resonators [81].



can be written in the following general form:

$$\mathcal{L}\mathbf{W}(\mathbf{x}) - \omega^2 \mathcal{M}\mathbf{W}(\mathbf{x}) - \mathcal{R}(\mathbf{x}) = \mathbf{0} \quad (2.1)$$

In Eq. (2.1), \mathcal{L} is the stiffness operator, \mathcal{M} is the mass operator, \mathcal{R} is the operator associated with the reaction forces of the resonators, given as:

$$\mathcal{L} = \begin{bmatrix} D_1 \nabla_1 & \dots & 0 \\ \vdots & \ddots & \vdots \\ 0 & \dots & D_{n_p} \nabla_{n_p} \end{bmatrix} \quad \nabla_k = \frac{\partial^4}{\partial x^4} + 2 \frac{\partial^4}{\partial x^2 \partial y^2} + \frac{\partial^4}{\partial y^4} \quad (2.2)$$

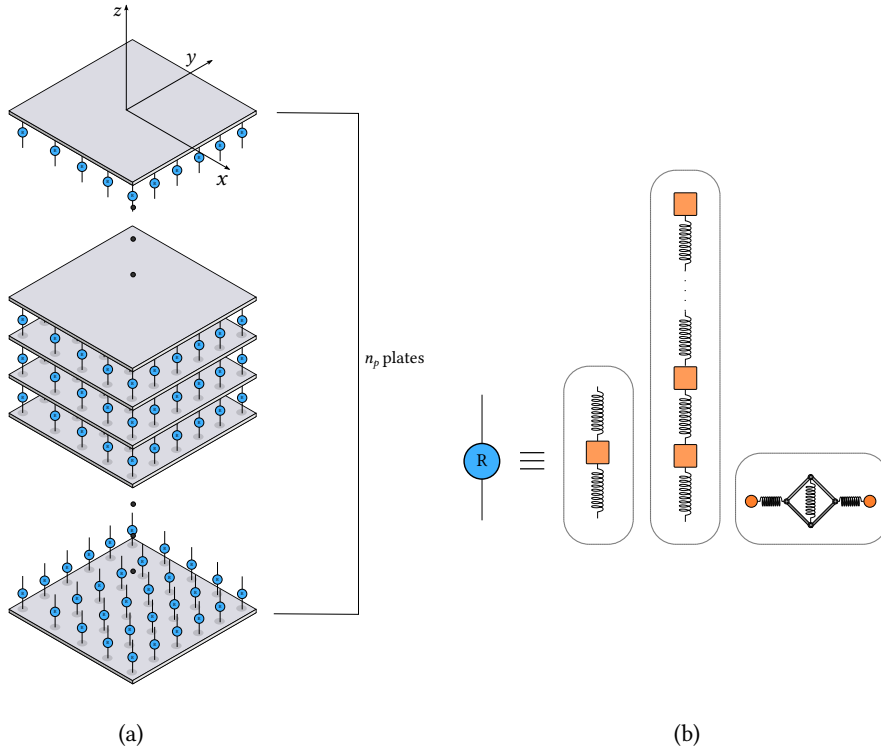


Figure 2.2: System under study: (a) assembly of plates coupled by arrays of resonators; (b) multi-DOF resonators.

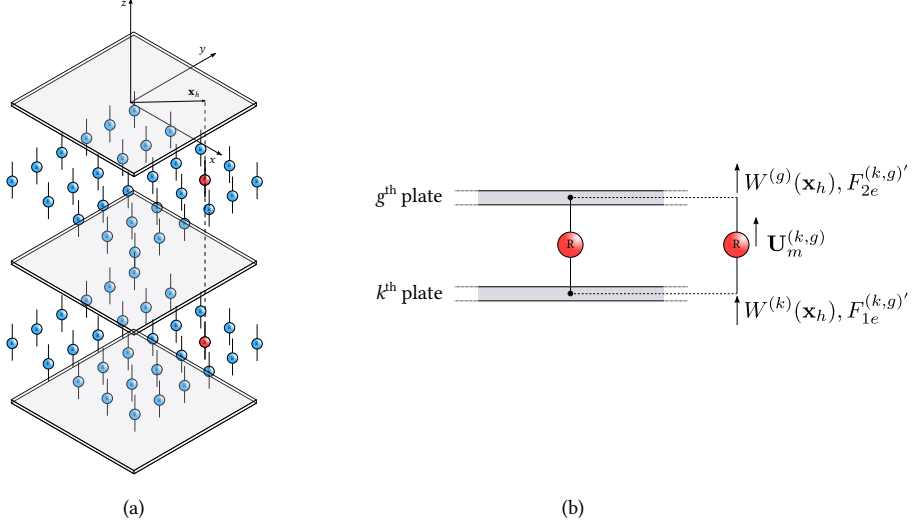
$$\mathcal{M} = \begin{bmatrix} \rho_1 h_1 & \dots & 0 \\ \vdots & \ddots & \vdots \\ 0 & \dots & \rho_{n_p} h_{n_p} \end{bmatrix} \quad (2.3)$$

$$\mathcal{R}(\mathbf{x}) = \sum_{h=1}^{N_r} \mathbf{R}_h \delta(\mathbf{x} - \mathbf{x}_h) \quad (2.4)$$

where $D_k = E_k h_k^3 / 12(1 - \nu_k^2)$ is the flexural stiffness of the k^{th} plate, E_k the Young modulus, ν_k the Poisson coefficient, h_k the thickness and ρ_k the mass volume density; N_r is the number of resonators connecting two consecutive plates, $\mathbf{R}_h = \mathbf{R}_h(\omega)$ is a frequency-dependent vector including the reaction forces that the $(n_p - 1)$ resonators aligned along a vertical line at $\mathbf{x} = \mathbf{x}_h$ exerts on the plates, $\delta(\mathbf{x} - \mathbf{x}_h)$ is the bi-dimensional Dirac's delta; finally,

the bar in Eq. (2.2) means generalized derivative, which is considered as \mathcal{R} in Eq. (2.4) involves Dirac's deltas.

Figure 2.3: Resonators of the system in Figure 2.2: (a) Resonators at $\mathbf{x} = \mathbf{x}_h$; (b) Forces and displacements of the resonator at $\mathbf{x} = \mathbf{x}_h$, between the k^{th} and g^{th} plates.



The reduced-order model hinges on the fact that the vector \mathbf{R}_h in Eq. (2.4) can be obtained by an exact dynamic condensation of the DOFs within the resonators. Consider the equation of motion in the frequency domain of the resonator coupling the k^{th} and g^{th} plates at $\mathbf{x} = \mathbf{x}_h$ (as shown see Figure 2.3):

$$\begin{bmatrix} \mathbf{K}_{ee}^{(k,g)} & \mathbf{K}_{em}^{(k,g)} \\ \mathbf{K}_{me}^{(k,g)} & \mathbf{K}_{mm}^{(k,g)} \end{bmatrix} \begin{bmatrix} \mathbf{U}_e^{(k,g)} \\ \mathbf{U}_m^{(k,g)} \end{bmatrix} = \begin{bmatrix} \mathbf{F}_e^{(k,g)'} \\ \mathbf{0} \end{bmatrix} \quad (2.5)$$

where $\mathbf{F}_e^{(k,g)'} = \begin{bmatrix} F_{1e}^{(k,g)'} & F_{2e}^{(k,g)'} \end{bmatrix}^T$ is the force exerted by the plates on the resonator, $\mathbf{U}_m^{(k,g)}$ is the vector collecting the DOFs of the masses within the resonator, $\mathbf{U}_e^{(k,g)} = \mathbf{W}^{(k,g)}(\mathbf{x}_h) = \begin{bmatrix} W^{(k)}(\mathbf{x}_h) & W^{(g)}(\mathbf{x}_h) \end{bmatrix}^T$ is the vector of the k^{th} and g^{th} plate deflections at the attachment points of the resonator. Being $\mathbf{F}_e^{(k,g)} = -\mathbf{F}_e^{(k,g)'}$, Eq. (2.5) yields:

$$\mathbf{F}_e^{(k,g)} = -\kappa_{eq}^{(k,g)}(\omega) \mathbf{W}^{(k,g)}(\mathbf{x}_h) = -[\mathbf{K}_{ee}^{(k,g)} - \mathbf{K}_{em}^{(k,g)} (\mathbf{K}_{mm}^{(k,g)})^{-1} \mathbf{K}_{me}^{(k,g)}] \mathbf{W}^{(k,g)}(\mathbf{x}_h) \quad (2.6)$$

The matrix $\boldsymbol{\kappa}_{eq}^{(k,g)}(\omega)$ in Eq. (2.6) assumes the following form:

$$\boldsymbol{\kappa}_{eq}^{(k,g)}(\omega) = \mathbf{K}_{ee}^{(k,g)} - \mathbf{K}_{em}^{(k,g)} (\mathbf{K}_{mm}^{(k,g)})^{-1} \mathbf{K}_{me}^{(k,g)} = \begin{bmatrix} \kappa_{11}^{(k,g)}(\omega) & \kappa_{12}^{(k,g)}(\omega) \\ \kappa_{21}^{(k,g)}(\omega) & \kappa_{22}^{(k,g)}(\omega) \end{bmatrix} \quad (2.7)$$

Based on Eq. (2.6) and Eq. (2.7), vector \mathbf{R}_h in Eq. (2.4) can be written as

$$\mathbf{R}_h = -\boldsymbol{\kappa}_{eq}(\omega) \mathbf{W}(\mathbf{x}_h) \quad (2.8)$$

Reactions exerted by the resonators

where $\mathbf{W}(\mathbf{x}_h) = [W_1(\mathbf{x}_h) \ \dots \ W_{n_p}(\mathbf{x}_h)]^T$ is the vector collecting the deflections of the attachment points of the $(n_p - 1)$ resonators aligned along the vertical line at $\mathbf{x} = \mathbf{x}_h$ and $\boldsymbol{\kappa}_{eq}(\omega)$ is a frequency-dependent symmetric stiffness matrix given as

$$\boldsymbol{\kappa}_{eq}(\omega) = \mathbf{P}^T \tilde{\boldsymbol{\kappa}}_{eq}(\omega) \mathbf{P} \quad (2.9)$$

being $\tilde{\boldsymbol{\kappa}}_{eq}$

$$\tilde{\boldsymbol{\kappa}}_{eq}(\omega) = \begin{bmatrix} \boldsymbol{\kappa}_{eq}^{(1,2)} & \dots & \mathbf{0} \\ \vdots & \ddots & \vdots \\ \mathbf{0} & \dots & \boldsymbol{\kappa}_{eq}^{(n_p-1, n_p)} \end{bmatrix} \quad (2.10)$$

and \mathbf{P} the matrix relating $\mathbf{W}(\mathbf{x}_h)$ to the vector $\mathbf{U}_e = [\mathbf{U}_e^{(1,2)T} \ \dots \ \mathbf{U}_e^{(n_p-1, n_p)T}]^T$, i.e.

$$\mathbf{U}_e = \mathbf{P} \mathbf{W}(\mathbf{x}_h) \quad (2.11)$$

$$\mathbf{P} = \begin{bmatrix} 1 & 0 & 0 & \dots & 0 \\ \mathbf{0} & \mathbf{v} & \mathbf{0} & \dots & \mathbf{0} \\ \vdots & \ddots & \ddots & \ddots & \vdots \\ \mathbf{0} & \dots & \mathbf{0} & \mathbf{v} & \mathbf{0} \\ 0 & \dots & 0 & 0 & 1 \end{bmatrix} \quad (2.12)$$

with $\mathbf{v} = [1 \ 1]^T$. To demonstrate Eqs. (2.8)-(2.9), it is noticed that

$$\mathbf{R}_h = \mathbf{P}^T \mathbf{F}_e = -\mathbf{P}^T \mathbf{F}'_e \quad (2.13)$$

where $\mathbf{F}_e = -\mathbf{F}'_e = [\mathbf{F}_e^{(1,2)T} \ \dots \ \mathbf{F}_e^{(n_p-1, n_p)T}]^T$, being \mathbf{F}'_e the vector collecting the forces exerted by the plates on the resonators aligned along the vertical line at $\mathbf{x} = \mathbf{x}_h$,

$$\mathbf{F}'_e = \tilde{\boldsymbol{\kappa}}_{eq}(\omega) \mathbf{U}_e \quad (2.14)$$

with $\tilde{\kappa}_{eq}$ given by Eq. (2.10) and Eq. (2.11) respectively.

The proposed reduced-order dynamic-stiffness model hinges on Eq. (2.8), as it expresses the reaction forces of the resonators in terms of the deflections of the attachment points on the plates, without involving any of the DOFs within the resonators. Consequently, the model-order reduction does not require any approximation, because the dynamic condensation of the DOFs within the resonators in Eq. (2.6) is exact.

2.3 Reduced-order global dynamic-stiffness matrix

The formulation of a reduced-order global dynamic-stiffness matrix for the system in Figure 2.2, which depends only on generalized coordinates describing the dynamics of the plates, is derived by using the model-order reduction introduced in Section 2.2.

2.3.1 Implementation

The space distribution of the resonators determines the subdivision of the plates in parallel strips as depicted in Figure 2.4. For the j^{th} strip on the k^{th} plate, see Figure 2.5, be

$$\begin{bmatrix} f_1^{(k,j)}(y) \\ f_2^{(k,j)}(y) \\ f_3^{(k,j)}(x) \\ f_4^{(k,j)}(x) \\ f_5^{(k,j)}(y) \\ f_6^{(k,j)}(y) \\ f_7^{(k,j)}(x) \\ f_8^{(k,j)}(x) \end{bmatrix} = \begin{bmatrix} V_x^{(k,j)}(a, y) \\ M_x^{(k,j)}(a, y) \\ V_y^{(k,j)}(x, b) \\ M_y^{(k,j)}(x, b) \\ -V_x^{(k,j)}(-a, y) \\ -M_x^{(k,j)}(-a, y) \\ -V_y^{(k,j)}(x, -b) \\ -M_y^{(k,j)}(x, -b) \end{bmatrix} ; \quad \begin{bmatrix} d_1^{(k,j)}(y) \\ d_2^{(k,j)}(y) \\ d_3^{(k,j)}(x) \\ d_4^{(k,j)}(x) \\ d_5^{(k,j)}(y) \\ d_6^{(k,j)}(y) \\ d_7^{(k,j)}(x) \\ d_8^{(k,j)}(x) \end{bmatrix} = \begin{bmatrix} W^{(k,j)}(a, y) \\ \Phi_x^{(k,j)}(a, y) \\ W^{(k,j)}(x, b) \\ \Phi_y^{(k,j)}(x, b) \\ W^{(k,j)}(-a, y) \\ \Phi_x^{(k,j)}(-a, y) \\ W^{(k,j)}(x, -b) \\ \Phi_y^{(k,j)}(x, -b) \end{bmatrix} \quad (2.15)$$

the vectors collecting (generalized) forces and displacements, i.e. Kirchhoff shear forces and bending moment per unit length, deflection and rotation along the four edges of the strip, being $\Phi_x^{(k,j)}(x, y) = -\partial W^{(k,j)} / \partial x$ and $\Phi_y^{(k,j)}(x, y) = -\partial W^{(k,j)} / \partial y$. It is noticed that every force/displacement in Eq. (2.15) is a single-variable function over the respective interval $[-a, a]$

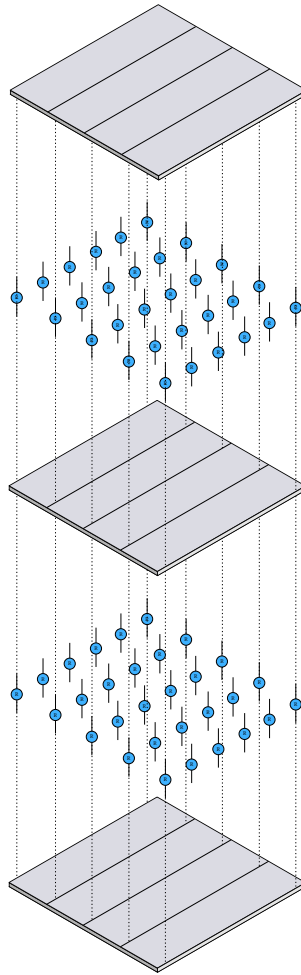


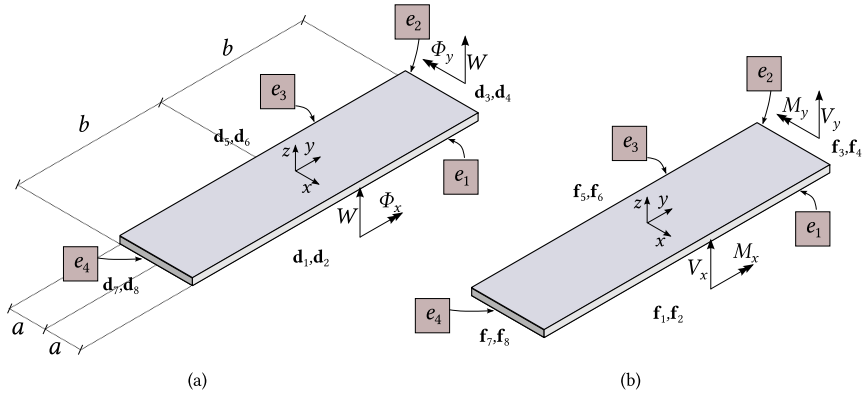
Figure 2.4: Parallel-strip subdivision of the plates of the system in Figure 2.2, according to the space distribution of the resonators.

or $[-b, b]$ and can be represented by the following modified Fourier series representation [48]

$$q(\xi) = \sum_{\substack{s=0 \\ l \in \{0,1\}}}^{\infty} Q_s^{(l)} \frac{\mathcal{T}_l(\gamma_{ls}\xi)}{\sqrt{\zeta_{ls}L}} \quad (2.16)$$

$$Q_s^{(l)} = \int_{-L}^L q(\xi) \frac{\mathcal{T}_l(\gamma_{ls}\xi)}{\sqrt{\zeta_{ls}L}} d\xi \quad (2.17)$$

Figure 2.5: Generalized displacement (a) and forces (b) for a plate strip.



$$\mathcal{T}_l(\gamma_{ls}\tilde{\zeta}) = \begin{cases} \cos\left(\frac{s\pi}{L}\tilde{\zeta}\right) & l = 0 \\ \sin\left[\left(s + \frac{1}{2}\right)\frac{\pi}{L}\tilde{\zeta}\right] & l = 1 \end{cases} \quad \begin{matrix} \zeta \in [-L, L] \\ s \in \mathbb{N} \end{matrix} \quad (2.18)$$

$$\tilde{\zeta}_{ls} = \begin{cases} 2 & l = 0 \text{ and } s = 0 \\ 1 & l = 1 \text{ or } s \geq 1 \end{cases} \quad (2.19)$$

where L indicates either a or b . Representing all the components in Eq. (2.15) by Eq. (2.16) and using the governing equations provide the following matrix relation:

$$\mathbf{f}^{(k,j)} = \mathbf{D}^{(k,j)}(\omega)\mathbf{d}^{(k,j)} \quad (2.20)$$

where $\mathbf{D}^{(k,j)}(\omega)$ is the dynamic-stiffness matrix of the j^{th} bare strip of the

k^{th} plate, i.e. [48]

$$\begin{bmatrix} \mathbf{f}_1^{(k,j)} \\ \mathbf{f}_2^{(k,j)} \\ \mathbf{f}_3^{(k,j)} \\ \mathbf{f}_4^{(k,j)} \\ \mathbf{f}_5^{(k,j)} \\ \mathbf{f}_6^{(k,j)} \\ \mathbf{f}_7^{(k,j)} \\ \mathbf{f}_8^{(k,j)} \end{bmatrix} = \begin{bmatrix} \mathbf{K}_{11}^{(k,j)} & \mathbf{K}_{12}^{(k,j)} & \mathbf{K}_{13}^{(k,j)} & \mathbf{K}_{14}^{(k,j)} & \mathbf{K}_{15}^{(k,j)} & \mathbf{K}_{16}^{(k,j)} & \mathbf{K}_{17}^{(k,j)} & \mathbf{K}_{18}^{(k,j)} \\ \mathbf{K}_{21}^{(k,j)} & \mathbf{K}_{22}^{(k,j)} & \mathbf{K}_{23}^{(k,j)} & \mathbf{K}_{24}^{(k,j)} & \mathbf{K}_{25}^{(k,j)} & \mathbf{K}_{26}^{(k,j)} & \mathbf{K}_{27}^{(k,j)} & \mathbf{K}_{28}^{(k,j)} \\ \mathbf{K}_{31}^{(k,j)} & \mathbf{K}_{32}^{(k,j)} & \mathbf{K}_{33}^{(k,j)} & \mathbf{K}_{34}^{(k,j)} & \mathbf{K}_{35}^{(k,j)} & \mathbf{K}_{36}^{(k,j)} & \mathbf{K}_{37}^{(k,j)} & \mathbf{K}_{38}^{(k,j)} \\ \mathbf{K}_{41}^{(k,j)} & \mathbf{K}_{42}^{(k,j)} & \mathbf{K}_{43}^{(k,j)} & \mathbf{K}_{44}^{(k,j)} & \mathbf{K}_{45}^{(k,j)} & \mathbf{K}_{46}^{(k,j)} & \mathbf{K}_{47}^{(k,j)} & \mathbf{K}_{48}^{(k,j)} \\ \mathbf{K}_{51}^{(k,j)} & \mathbf{K}_{52}^{(k,j)} & \mathbf{K}_{53}^{(k,j)} & \mathbf{K}_{54}^{(k,j)} & \mathbf{K}_{55}^{(k,j)} & \mathbf{K}_{56}^{(k,j)} & \mathbf{K}_{57}^{(k,j)} & \mathbf{K}_{58}^{(k,j)} \\ \mathbf{K}_{61}^{(k,j)} & \mathbf{K}_{62}^{(k,j)} & \mathbf{K}_{63}^{(k,j)} & \mathbf{K}_{64}^{(k,j)} & \mathbf{K}_{65}^{(k,j)} & \mathbf{K}_{66}^{(k,j)} & \mathbf{K}_{67}^{(k,j)} & \mathbf{K}_{68}^{(k,j)} \\ \mathbf{K}_{71}^{(k,j)} & \mathbf{K}_{72}^{(k,j)} & \mathbf{K}_{73}^{(k,j)} & \mathbf{K}_{74}^{(k,j)} & \mathbf{K}_{75}^{(k,j)} & \mathbf{K}_{76}^{(k,j)} & \mathbf{K}_{77}^{(k,j)} & \mathbf{K}_{78}^{(k,j)} \\ \mathbf{K}_{81}^{(k,j)} & \mathbf{K}_{82}^{(k,j)} & \mathbf{K}_{83}^{(k,j)} & \mathbf{K}_{84}^{(k,j)} & \mathbf{K}_{85}^{(k,j)} & \mathbf{K}_{86}^{(k,j)} & \mathbf{K}_{87}^{(k,j)} & \mathbf{K}_{88}^{(k,j)} \end{bmatrix} \begin{bmatrix} \mathbf{d}_1^{(k,j)} \\ \mathbf{d}_2^{(k,j)} \\ \mathbf{d}_3^{(k,j)} \\ \mathbf{d}_4^{(k,j)} \\ \mathbf{d}_5^{(k,j)} \\ \mathbf{d}_6^{(k,j)} \\ \mathbf{d}_7^{(k,j)} \\ \mathbf{d}_8^{(k,j)} \end{bmatrix} \quad (2.21)$$

All entries of the matrix $\mathbf{D}^{(k,j)}(\omega)$ in Eq. (2.21) are available in a concise analytical form, as demonstrated in ref. [48]. Further, in Eq. (2.21) $\mathbf{d}_i^{(k,j)}$ and $\mathbf{f}_i^{(k,j)}$ denote the sub-vectors collecting the coefficients of the modified Fourier series representations used for the displacements and forces along the strip (see Figure 2.5)

$$\begin{aligned} \mathbf{d}_i^{(k,j)} &= \begin{bmatrix} d_{i0}^{(0,k,j)} & d_{i1}^{(0,k,j)} & d_{i2}^{(0,k,j)} & \dots & d_{i0}^{(1,k,j)} & d_{i1}^{(1,k,j)} & d_{i2}^{(1,k,j)} & \dots \end{bmatrix}^T \\ \mathbf{f}_i^{(k,j)} &= \begin{bmatrix} f_{i0}^{(0,k,j)} & f_{i1}^{(0,k,j)} & f_{i2}^{(0,k,j)} & \dots & f_{i0}^{(1,k,j)} & f_{i1}^{(1,k,j)} & f_{i2}^{(1,k,j)} & \dots \end{bmatrix}^T \end{aligned} \quad (2.22)$$

where the superscripts $(0, k, j)$ and $(1, k, j)$ indicate the coefficients associated with cosine terms ($l = 0$) and sine terms ($l = 1$) in the modified Fourier series representations (2.16) for the j^{th} strip of the k^{th} plate.

The dynamic-stiffness matrix $\mathbf{D}^{(k)}(\omega)$ of the k^{th} plate is built by assembling the dynamic-stiffness matrices $\mathbf{D}^{(k,j)}(\omega)$ of the strips, as in a standard FE assembly procedure. Consequently, the size of the dynamic-stiffness matrix of the plate depends on the number of generalized coordinates representing the response variables along the external edges and the internal lines, as shown in the following figure:

Having built the dynamic-stiffness matrix for every plate separately, the next step is constructing the global dynamic-stiffness matrix for the whole system in Figure 2.4, that is for the system of plates coupled by the arrays of resonators. For any two consecutive plates coupled by an array of resonators, this task is performed as schematically illustrated in Figure 2.7,

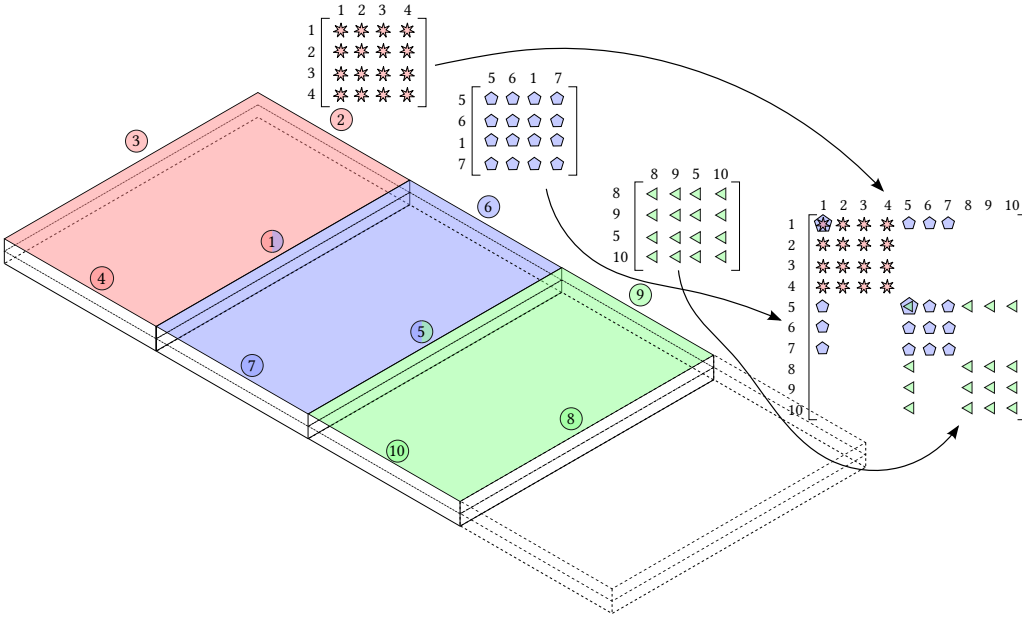


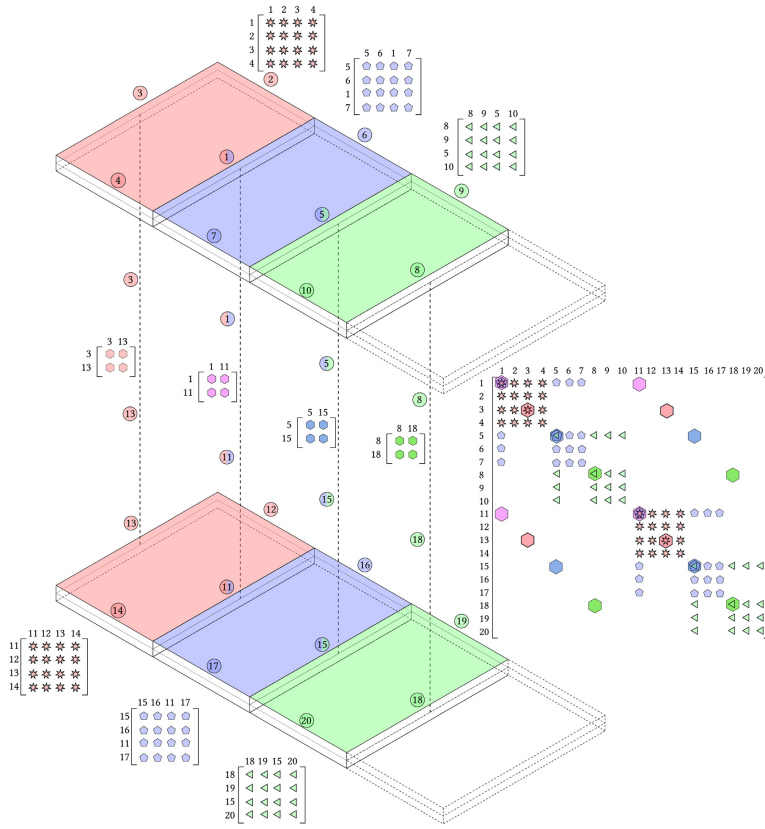
Figure 2.6: Assembly procedure of the dynamic-stiffness matrix of the system in Figure 2.2.

where symbol “ \diamond ” denotes the dynamic-stiffness matrix in the following equation, which is associated with every line of resonators shown in Figure 2.4:

$$\begin{bmatrix} \mathbf{r}_1^{(k)} \\ \mathbf{r}_2^{(g)} \end{bmatrix} = \begin{bmatrix} \mathcal{K}_{11} & \mathcal{K}_{12} \\ \mathcal{K}_{21} & \mathcal{K}_{22} \end{bmatrix} \begin{bmatrix} \mathbf{u}_1^{(k)} \\ \mathbf{u}_2^{(g)} \end{bmatrix} \quad (2.23)$$

Symbols $\mathbf{u}_1^{(k)}$ and $\mathbf{u}_2^{(g)}$ denote specific subvectors $\mathbf{d}_i^{(k,j)}$ and $\mathbf{d}_i^{(g,j)}$ in Eq. (2.21), namely: $\mathbf{u}_1^{(k)} = \mathbf{d}_1^{(k,j)}$ and $\mathbf{u}_2^{(g)} = \mathbf{d}_1^{(g,j)}$ or $\mathbf{u}_1^{(k)} = \mathbf{d}_3^{(k,j)}$ and $\mathbf{u}_2^{(g)} = \mathbf{d}_3^{(g,j)}$ if the line of resonators coincide with the edge e_1 or the edge e_3 respectively, for the j^{th} strip of k^{th} and g^{th} plates. Matrices \mathcal{K}_{11} , \mathcal{K}_{12} , \mathcal{K}_{21} , \mathcal{K}_{22} in Eq. (2.23) can be partitioned as follows, on the basis of Eq. (2.22):

$$\begin{aligned} \mathcal{K}_{11} &= \begin{bmatrix} \mathcal{K}_{11}^{00} & \mathcal{K}_{11}^{01} \\ \mathcal{K}_{11}^{10} & \mathcal{K}_{11}^{11} \end{bmatrix}; & \mathcal{K}_{12} &= \begin{bmatrix} \mathcal{K}_{12}^{00} & \mathcal{K}_{12}^{01} \\ \mathcal{K}_{12}^{10} & \mathcal{K}_{12}^{11} \end{bmatrix} \\ \mathcal{K}_{21} &= \begin{bmatrix} \mathcal{K}_{21}^{00} & \mathcal{K}_{21}^{01} \\ \mathcal{K}_{21}^{10} & \mathcal{K}_{21}^{11} \end{bmatrix}; & \mathcal{K}_{22} &= \begin{bmatrix} \mathcal{K}_{22}^{00} & \mathcal{K}_{22}^{01} \\ \mathcal{K}_{22}^{10} & \mathcal{K}_{22}^{11} \end{bmatrix} \end{aligned} \quad (2.24)$$



with each submatrix given by:

$$(\mathcal{K}_{11}^{tl})_{vs} = -\kappa_{11}^{(k,g)}(\omega) \sum_{h=1}^{n_e} \frac{\mathcal{T}_t(\gamma_{tv}\xi_h)}{\sqrt{\zeta_{tv}L}} \frac{\mathcal{T}_l(\gamma_{ls}\xi_h)}{\sqrt{\zeta_{ls}L}} \quad (2.25)$$

$$(\mathcal{K}_{12}^{tl})_{vs} = -\kappa_{12}^{(k,g)}(\omega) \sum_{h=1}^{n_e} \frac{\mathcal{T}_t(\gamma_{tv}\xi_h)}{\sqrt{\zeta_{tv}L}} \frac{\mathcal{T}_l(\gamma_{ls}\xi_h)}{\sqrt{\zeta_{ls}L}} \quad (2.26)$$

$$(\mathcal{K}_{21}^{tl})_{vs} = -\kappa_{21}^{(k,g)}(\omega) \sum_{h=1}^{n_e} \frac{\mathcal{T}_t(\gamma_{tv}\xi_h)}{\sqrt{\zeta_{tv}L}} \frac{\mathcal{T}_l(\gamma_{ls}\xi_h)}{\sqrt{\zeta_{ls}L}} \quad (2.27)$$

$$(\mathcal{K}_{22}^{tl})_{vs} = -\kappa_{22}^{(k,g)}(\omega) \sum_{h=1}^{n_e} \frac{\mathcal{T}_t(\gamma_{tv}\xi_h)}{\sqrt{\zeta_{tv}L}} \frac{\mathcal{T}_l(\gamma_{ls}\xi_h)}{\sqrt{\zeta_{ls}L}} \quad (2.28)$$

where $t, l \in \{0, 1\}$, L is the length of the edges of the strips mutually-connected by the resonators, n_e is the number of resonators along each of the connected edges, ξ_h is the coordinate of the attachment point of the h^{th}

Figure 2.7: Assembly procedure for the dynamic-stiffness matrices of two consecutive plates of the system in Figure 2.2 coupled by an array of resonators; symbol “ \diamond ” denote the dynamic-stiffness matrix (2.23) associated with a line of resonators.

resonator over the edge of the k^{th} and g^{th} plates.

2.3.2 Free vibrations analysis

The reduced-order global dynamic-stiffness matrix hereinafter as $\tilde{\mathbf{D}}$ (with tilde denoting “reduced order”) derived using the formulation proposed in Section 2.3 can be used to calculate the natural frequencies of the free-vibration problem governing the system in Figure 2.2 by the well-known Wittrick-Williams algorithm [83–86], which captures all the natural frequencies including multiple ones, to any desired degree of accuracy. The implementation of the Wittrick-Williams algorithm involves calculating the number of natural frequencies below a given trial frequency J , using the formula

$$J(\omega) = J_{0s} + J_{0r} + s[\tilde{\mathbf{D}}(\omega)] \quad (2.29)$$

where J_{0s} and J_{0r} are the numbers of “clamped-clamped” natural frequencies below ω of the bare strips (J_{0s}) and the resonators (J_{0r}). In this case, the term “clamped-clamped” denotes the natural frequencies of the internal modes within every strip and every resonator, when the generalized coordinates along the edges of the strips (i.e., the coordinates used to formulate the reduced-order global dynamic-stiffness matrix) are set equal to zero. Specifically, J_{0s} can be obtained by closed analytical expressions in ref. [48] while J_{0r} can be evaluated as [66]

$$J_{0r}(\omega) = \sum_{h=1}^{N_r(n_p-1)} \sum_{i=1}^{N_i} \min \left\{ 1, \left\lfloor \frac{\omega}{\omega_{hi}} \right\rfloor \right\} \quad (2.30)$$

where N_r is the number of resonators connecting two consecutive plates, n_p is the number of plates, N_i is the number of DOFs within every resonator and ω_{hi} is the i^{th} natural frequency of the h^{th} resonator.

For every calculated natural frequency, the associated deflection eigenfunctions in all the plates is derived as non-trivial solution of the eigenvalue problem involving the reduced-order global dynamic-stiffness matrix $\tilde{\mathbf{D}}$, as computed for that natural frequency. The corresponding modal rotations, bending moments, shear forces and twisting moment can be obtained using the plate equations. Furthermore, the modal displacements and internal forces within every resonator can be obtained from the equation of motion (2.5) of the resonator, being $\mathbf{U}_e^{(k,g)} = \mathbf{W}^{(k,g)}(\mathbf{x}_h)$ the vector of modal deflections of the attachment points on the plates. As a consequence, the

modal response within all the resonators can be fully described, remarkably so since the natural frequencies and modes are obtained by the reduced-order global dynamic-stiffness matrix that does not involve any of the DOFs within the resonators.

2.4 Modal response of the reduced-order dynamic-stiffness model

The natural frequencies and modes calculated from the reduced-order global dynamic-stiffness matrix $\tilde{\mathbf{D}}$ formulated in Section 2.3, allows to compute the modal response under arbitrary loading of the system in Figure 2.2, in both time and frequency domains, once suitable orthogonality conditions for the modes of the reduced-order model are found as shown in the next Section.

2.4.1 Orthogonality conditions

The stiffness operator \mathcal{L} in Eq. (2.2) and the mass operator \mathcal{M} in Eq. (2.3) are both self-adjoint [55], i.e.

$$\int_A \mathbf{W}_n^T \mathcal{L} \mathbf{W}_m \, dA = \int_A \mathbf{W}_m^T \mathcal{L} \mathbf{W}_n \, dA \quad (2.31)$$

$$\int_A \mathbf{W}_n^T \mathcal{M} \mathbf{W}_m \, dA = \int_A \mathbf{W}_m^T \mathcal{M} \mathbf{W}_n \, dA \quad (2.32)$$

being A the domain of the plates, \mathbf{W}_n and \mathbf{W}_m the vector of the n^{th} and m^{th} deflection eigenfunctions in all the plates, fulfilling homogeneous BCs.

Making use of Eqs. (2.31)–(2.32), Eq. (2.1) for (\mathbf{W}_m, ω_m) and (\mathbf{W}_n, ω_n) reads

$$\mathcal{L} \mathbf{W}_m(\mathbf{x}) - \omega_m^2 \mathcal{M} \mathbf{W}_m(\mathbf{x}) + \sum_{h=1}^{N_r} \kappa_{eq}(\omega_m) \mathbf{W}_m(x_h) \delta(\mathbf{x} - \mathbf{x}_h) = \mathbf{0} \quad (2.33)$$

$$\mathcal{L} \mathbf{W}_n(\mathbf{x}) - \omega_n^2 \mathcal{M} \mathbf{W}_n(\mathbf{x}) + \sum_{h=1}^{N_r} \kappa_{eq}(\omega_n) \mathbf{W}_n(x_h) \delta(\mathbf{x} - \mathbf{x}_h) = \mathbf{0} \quad (2.34)$$

Multiplying Eq. (2.33) by \mathbf{W}_n and Eq. (2.34) by \mathbf{W}_m , integrating the two

equations over A and considering the BCs yield:

$$\int_A \mathbf{W}_n^T \mathcal{L} \mathbf{W}_m \, dA - \omega_m^2 \int_A \mathbf{W}_n^T \mathcal{M} \mathbf{W}_m \, dA + \sum_{h=1}^{N_r} \mathbf{W}_n^T(x_h) \boldsymbol{\kappa}_{eq}(\omega_m) \mathbf{W}_m(x_h) = 0 \quad (2.35)$$

$$\int_A \mathbf{W}_m^T \mathcal{L} \mathbf{W}_n \, dA - \omega_n^2 \int_A \mathbf{W}_m^T \mathcal{M} \mathbf{W}_n \, dA + \sum_{h=1}^{N_r} \mathbf{W}_m^T(x_h) \boldsymbol{\kappa}_{eq}(\omega_n) \mathbf{W}_n(x_h) = 0 \quad (2.36)$$

Using self-adjointness of \mathcal{L} and \mathcal{M} , see Eq. (2.31) and Eq. (2.32), as well the symmetry of matrix $\boldsymbol{\kappa}_{eq}(\omega)$ in Eq. (2.9), the difference between Eq. (2.35) and Eq. (2.36) provides the first orthogonality condition:

$$\omega_n(\omega_n + \omega_m) \int_A \mathbf{W}_m^T \mathcal{M} \mathbf{W}_n \, dA + \omega_n \sum_{h=1}^{N_r} \frac{\mathbf{W}_m(x_h)^T (\boldsymbol{\kappa}_{eq}(\omega_n) - \boldsymbol{\kappa}_{eq}(\omega_m)) \mathbf{W}_n(x_h)}{\omega_m - \omega_n} = 0 \quad (2.37)$$

Further, upon multiplying Eq. (2.35) by ω_n and Eq. (2.36) by ω_m , the difference of the two equations leads to the second orthogonality condition:

$$\int_A \mathbf{W}_m^T \mathcal{L} \mathbf{W}_n \, dA = - \sum_{h=1}^{N_r} \frac{\mathbf{W}_m(x_h)^T (\omega_m \boldsymbol{\kappa}_{eq}(\omega_n) - \omega_n \boldsymbol{\kappa}_{eq}(\omega_m)) \mathbf{W}_n(x_h)}{\omega_m - \omega_n} - \omega_n \omega_m \int_A \mathbf{W}_m^T \mathcal{M} \mathbf{W}_n \, dA \quad (2.38)$$

The orthogonality conditions (2.37) and (2.38) involve the modes of the plates only and do not involve any DOF within the resonators. Eq. (2.1), Eq. (2.37) and Eq. (2.38) are the basis to formulate the proposed reduced-order model approach to calculate the modal response.

2.4.2 Modal response

In order to derive the modal response, consider the governing equation of the system in Figure 2.2 under an impulsive load, given as

$$\mathcal{L} \mathbf{w}(\mathbf{x}, t) + \mathcal{M} \ddot{\mathbf{w}}(\mathbf{x}, t) - \mathcal{R}(\mathbf{x}, t) = \mathbf{f}(\mathbf{x}) \delta(t) \quad (2.39)$$

where $\mathbf{f}(\mathbf{x})$ is a space-dependent loading function, with arbitrary location on any of the plates in Figure 2.2, \mathbf{w} is the vector collecting the time-dependent deflections in the plates and

$$\mathcal{R}(\mathbf{x}, t) = \sum_{h=1}^{N_r} \mathbf{r}_h \delta(\mathbf{x} - \mathbf{x}_h) \quad (2.40)$$

being $\mathbf{r}_h = \mathbf{r}_h(t)$ a time-dependent vector including the reaction forces that the $(n_p - 1)$ resonators aligned along a vertical line at $\mathbf{x} = \mathbf{x}_h$ exerts on the plates.

Using modal superposition, the deflection \mathbf{w} can be represented as

$$\mathbf{w}(\mathbf{x}, t) = \sum_{n=1}^{\infty} \mathbf{W}_n(\mathbf{x}) g_n(t) \quad (2.41)$$

where \mathbf{W}_n is the vector collecting the n^{th} deflection eigenfunctions in all the plates. Further, in view of the impulsive nature of the load, $g_n(t) = \bar{g}_n e^{i\omega_n t}$ and $g_n(t) = \bar{g}_n^* e^{-i\omega_n t}$, being \bar{g}_n and \bar{g}_n^* complex conjugate pairs.

First, assume that $g_n(t) = \bar{g}_n e^{i\omega_n t}$. Replacing Eq. (2.41) for $\mathbf{w}(\mathbf{x}, t)$ in Eq. (2.39) and taking into account that $\ddot{g}_n = -\omega_n^2 g_n(t)$, Eq. (2.39) takes the form

$$\sum_{n=1}^{\infty} \left(\frac{-\ddot{g}_n}{\omega_n^2} \right) \left\{ \mathcal{L} \mathbf{W}_n + \sum_{h=1}^{N_r} \kappa_{eq}(\omega_n) \mathbf{W}_n(\mathbf{x}_h) \delta(\mathbf{x} - \mathbf{x}_h) - \omega_n^2 \mathcal{M} \mathbf{W}_n(\mathbf{x}) \right\} = \mathbf{f}(\mathbf{x}) \delta(t) \quad (2.42)$$

Multiply Eq. (2.42) by \mathbf{W}_m and integrate over A to obtain

$$\sum_{n=1}^{\infty} \left(\frac{-\ddot{g}_n}{\omega_n^2} \right) \left\{ \int_A \mathbf{W}_m^T \mathcal{L} \mathbf{W}_n \, dA + \sum_{h=1}^{N_r} \mathbf{W}_m^T(\mathbf{x}_h) \kappa_{eq}(\omega_n) \mathbf{W}_n(\mathbf{x}_h) - \omega_n^2 \int_A \mathbf{W}_m^T \mathcal{M} \mathbf{W}_n \, dA \right\} = \chi_m \delta(t) \quad (2.43)$$

where χ_m is the projection of the space-dependent loading function \mathbf{f} on \mathbf{W}_m

$$\chi_m = \int_A \mathbf{W}_m^T \mathbf{f} \, dA \quad (2.44)$$

Making use of the orthogonality condition (2.38), Eq. (2.43) leads to

$$\sum_{n=1}^{\infty} \frac{\ddot{g}_n}{\omega_n^2} \left\{ (\omega_n \omega_m + \omega_n^2) \int_A \mathbf{W}_m^T \mathcal{M} \mathbf{W}_n \, dA + \omega_n \sum_{h=1}^{N_r} \frac{\mathbf{W}_m(\mathbf{x}_h)^T (\kappa_{eq}(\omega_n) - \kappa_{eq}(\omega_m)) \mathbf{W}_n(\mathbf{x}_h)}{\omega_m - \omega_n} \right\} = \chi_m \delta(t) \quad (2.45)$$

The first orthogonality condition (2.37) ensures that the expression within parenthesis in Eq. (2.45) is equal to zero for $\omega_m \neq \omega_n$. On the other hand, for $\omega_m = \omega_n$ the following decoupled system of equations is obtained:

$$\Pi_n \ddot{g}_n = \chi_n \delta(t) \quad (2.46)$$

where Π_n is

$$\Pi_n = \sum_{h=1}^{N_r} \omega_n^{-2} \mathbf{W}_n^T(\mathbf{x}_h) \boldsymbol{\mu}(\omega_n) \mathbf{W}_n(\mathbf{x}_h) + 2 \int_A \mathbf{W}_n^T \mathcal{M} \mathbf{W}_n \, dA \quad (2.47)$$

where the symbol $\boldsymbol{\mu}(\omega_n)$ in Eq. (2.47) denotes a resonator-dependent term calculated by the following limit

$$\boldsymbol{\mu}(\omega_n) = \lim_{\omega_m \rightarrow \omega_n} \omega_n \left(\frac{\boldsymbol{\kappa}_{eq}(\omega_n) - \boldsymbol{\kappa}_{eq}(\omega_m)}{\omega_m - \omega_n} \right) = -\omega_n \left. \frac{d\boldsymbol{\kappa}_{eq}}{d\omega} \right|_{\omega=\omega_n} \quad (2.48)$$

The dynamic-stiffness $\boldsymbol{\kappa}_{eq}(\omega)$ in Eq. (2.8) is differentiable for typical resonators involved in locally-resonant metamaterial plates, as mass-spring chains, mass-spring-truss resonators with lateral masses or elastic bars with distributed mass. Indeed, the frequency-dependent stiffness matrix involves polynomial and/or transcendental functions of the frequency.

As shown in Sec. 1.4, Eq. (2.46) is the basis to derive the complex coefficients in Eq. (2.41), which are given by Eq. (1.67). Furthermore, once the vector \mathbf{Y}_n collecting the n^{th} eigenfunctions of all response variables, i.e. deflection, rotation, bending moment, shear forces and twisting moment in all the plates as derived from the Kirchhoff-Love plate equations, as well as displacements and forces within the resonators (see at the end of Section 2.3.2 for the calculation of the eigenfunctions from the reduced-order global dynamic-stiffness matrix) is known, Eq. (1.68) and Eq. (1.72) can be used to compute the modal response to arbitrary loads obtaining Eqs. (1.74)-(1.75).

Eq. (1.74) and Eq. (1.75) apply for arbitrary dynamic loads. Recognize that time dependence and frequency dependence of the load are accounted for in $f(t)$ and $\hat{f}(\omega)$, while space dependence is included in Eq. (2.44) for χ_n , which is involved in the impulse and frequency response functions (1.68)-(1.72). Analytical expressions for Eq. (1.74) are obviously available for time-dependent harmonic loads or other typical time-dependent loading functions in dynamics.

2.5 Numerical applications

Consider the system in Figure 2.8, consisting of two 1×1 m square plates mutually connected by 1-DOF resonators. Both plates are simply supported along the two parallel edges in the x -direction. The parameters of the plates

and the resonators are: $E = 77.6 \text{ GPa}$, $\rho = 2730 \text{ kg/m}^3$, $m_r = 0.25 \text{ kg}$, $k_r = 1 \times 10^5 \text{ N/m}$. The mutual distance between the plates is 20 cm [60]. It is assumed that the lines of resonators are at distance 0.05 m from the edges of the plate. The total number of resonators is $N_r(n_p - 1) = 100$.

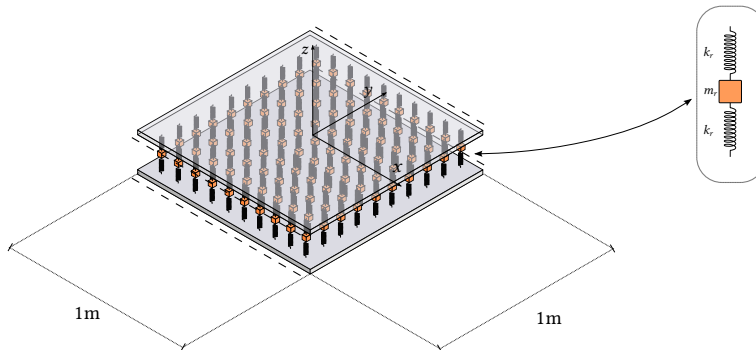


Figure 2.8: Locally-resonant metamaterial plate consisting of two simply-supported plates connected by 1-DOF resonators

The proposed dynamic-stiffness approach is implemented in Matlab [54], dividing every plate in 11 strips. The modified Fourier series representations (2.16) for the response variables within every strip are truncated to the first $\mathcal{N} = 12$ terms, totalling $1104 = 12 \times (2\mathcal{N} + 2\mathcal{N}) + 2 \times 11 \times 2\mathcal{N}$ generalized coordinates for every plate, since there are: 12 edges of the strips in the y -direction, 2×11 edges of the strips in the x -direction, $2\mathcal{N}$ coefficients for deflection and $2\mathcal{N}$ coefficients for rotation along every edge, assuming \mathcal{N} terms associated with cosine terms ($l = 0$) and \mathcal{N} terms associated with sine terms ($l = 1$) (see Eq. (2.22)). As a result, the size of the reduced-order global dynamic-stiffness matrix $\tilde{\mathbf{D}}$ is 2208×2208 . The resonator DOFs are eliminated by the exact dynamic condensation described in Section 2.3. Specifically, the matrix $\kappa_{eq}(\omega)$ in Eq. (2.7) is given by

$$\kappa_{eq}^{(k,g)}(\omega) = \begin{bmatrix} k_r + \theta & \theta \\ \theta & k_r + \theta \end{bmatrix} \quad (2.49)$$

being $\theta = -k_r^2 / (2k_r - m_r\omega^2)$, which leads to the following expression for the matrix $\mu^{(k,g)}(\omega_n)$ in Eq. (2.48)

$$\mu^{(k,g)}(\omega_n) = \frac{2m_r k_r^2}{(2k_r - m_r\omega_n^2)^2} \begin{bmatrix} 1 & 1 \\ 1 & 1 \end{bmatrix} \quad (2.50)$$

For comparison, the system is implemented in Abaqus, using S4R5 4-node thin shell elements and considering 3 flexural DOFs for every node. Con-

sidering 2550 FEs and 2652 nodes for every plate, 100 nodes for the resonators, the size of the global stiffness and mass matrices is 15808×15808 , taking into account BCs along the simply supported edges. Specifically, a lumped formulation is adopted for the mass matrix.

Firstly, the natural frequencies are calculated from the reduced-order global dynamic-stiffness matrix $\tilde{\mathbf{D}}$ via the Wittrick-Williams algorithm and compared to the corresponding ones obtained by the FE method in Abaqus. Table 2.1 reports 20 of the calculated natural frequencies, showing an excellent agreement with relative errors up to 0.39% at most.

Table 2.1: First 20 natural frequencies of system in Figure 2.8, calculated by proposed reduced-order dynamic-stiffness model (DSM) and FE model in Abaqus (FEM).

Mode	FEM ($\cdot 10\text{Hz}$)	DSM ($\cdot 10\text{Hz}$)
1	2.0581	2.0581
2	3.3773	3.3905
3	7.4499	7.4705
4	7.8683	7.8621
5	9.0742	9.0835
6	9.9398	9.9394
7	10.4218	10.4274
8	11.7512	11.7709
9	12.1368	12.1468
10	12.7126	12.6976
11	12.9761	12.9682
12	13.3415	13.3511
13	13.4040	13.4276
14	13.4977	13.5032
15	13.6688	13.6712
16	13.8081	13.8023
17	13.8506	13.8466
18	13.8526	13.8553
19	13.8873	13.8914
20	13.9549	13.9568

The proposed reduced-order global dynamic-stiffness matrix is capable of capturing the natural frequencies of the system with remarkable accuracy and a very limited size of the model, as compared to the size of a standard FE one.

Furthermore, in Figure 2.9 two modes calculated by the proposed dynamic-stiffness approach are depicted. The corresponding eigenmodes within the

resonators can be also obtained, using the equation of motion (2.5) where $\mathbf{U}_e^{(k,g)} = \mathbf{W}^{(k,g)}(\mathbf{x}_h)$ is the vector collecting the deflections of the plates at the attachment points on the plates.

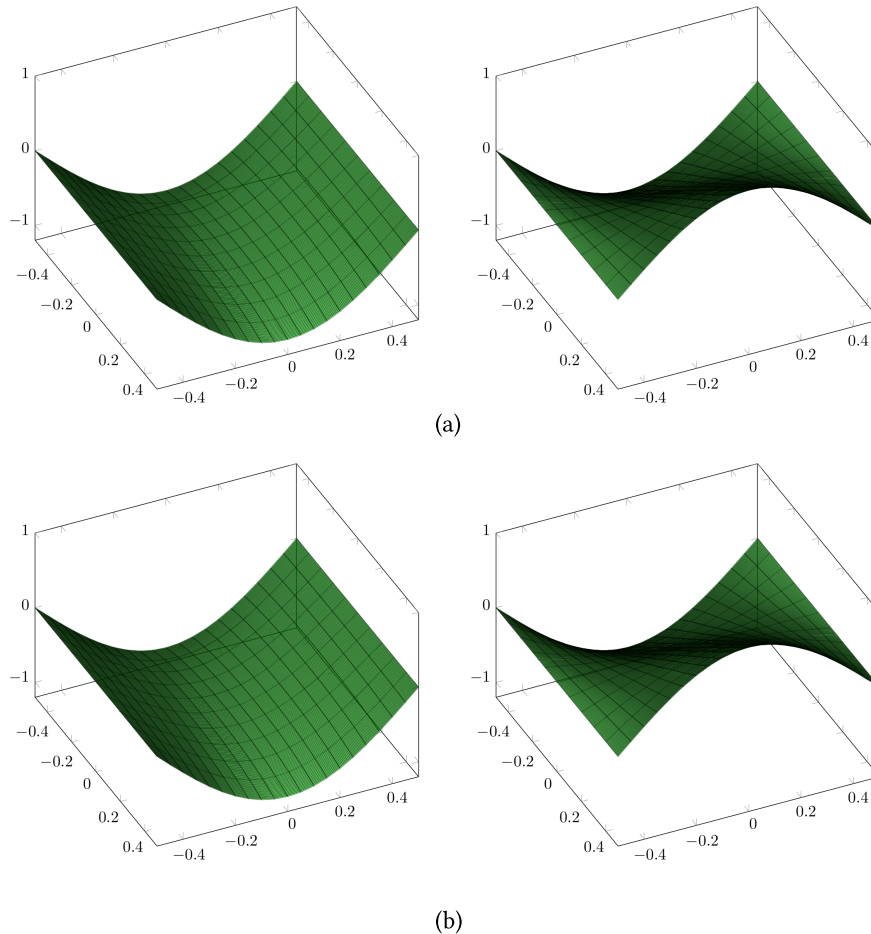
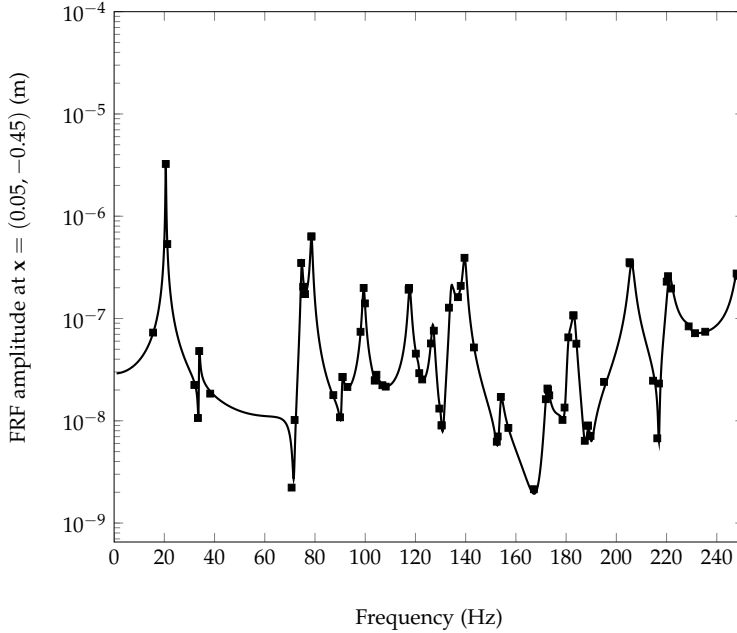


Figure 2.9: Mode shapes of the system in Figure 2.8, calculated by the proposed reduced-order dynamic-stiffness model: (a) top plate, first mode (left column) and second mode (right column); (b) bottom plate, first mode (left column) and second mode (right column).

The time and frequency responses can be calculated by means of Eq. (1.74) and Eq. (1.75). In particular, Eq. (1.74) and Eq. (1.75) are applied calculating $N_M = 200$ natural modes from the proposed reduced-order global dynamic-stiffness matrix and assuming, for all modes, an indicative modal damping ratio = 0.005. For comparison, time and frequency responses are calculated also by the corresponding FE modal expansions in Abaqus. For a first insight, consider a harmonic concentrated force $Fe^{i\omega t}$, $F = 1$ N, applied at $\mathbf{x}_f = (0.05, 0.45)$ in the bottom plate.

Figure 2.10 shows the deflection frequency response at $x_f = (0.05, -0.45)$ in the bottom plate, as given by Eq. (1.75) and the FE method. The agreement between the two solutions is excellent through the whole frequency domain, substantiating the accuracy of the proposed dynamic-stiffness approach.

Figure 2.10: Amplitude of the deflection frequency response function (FRF) at $x = (0.05, -0.45)$ in the bottom plate for concentrated harmonic $1e^{i\omega t}$ load applied at $x_f = (0.05, 0.45)$ in the bottom plate, calculated by proposed reduced-order dynamic-stiffness model (black continuous line) and FE model in Abaqus (black squares).



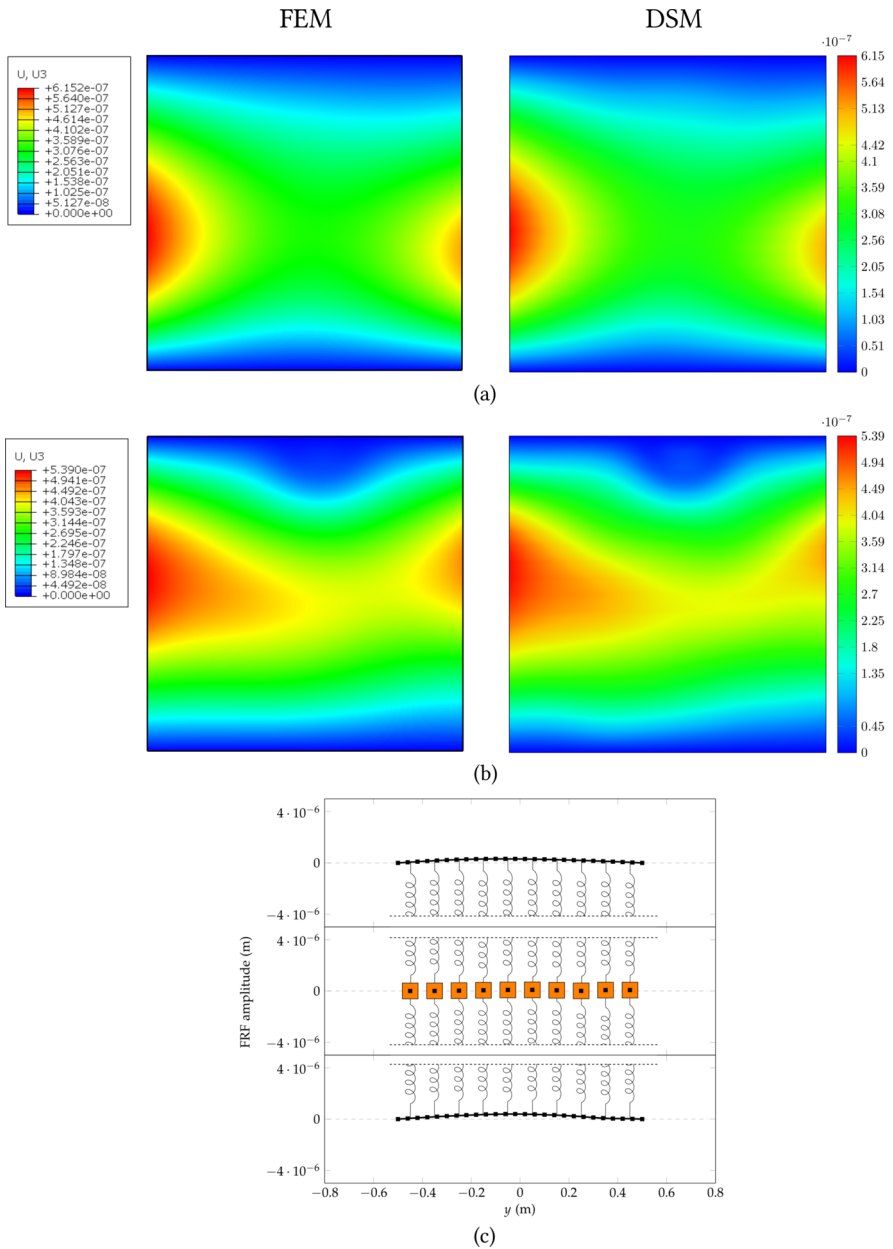
Further, Figures 2.11-2.13 show the frequency response (1.75) evaluated over the whole top and bottom plates, for three forcing frequencies of the harmonic concentrated force, $\omega = 101$ Hz, 142.1 Hz, 241.8 Hz. Again, a very satisfactory agreement is found between Eq. (1.75) and the corresponding FE solution. For completeness, Figures 2.11-2.13 illustrate also the displacement frequency response of the resonators along the line at $x = 0.05$, including the deflection frequency response of the plates. Specifically, the response of the resonators is obtained by Eq. (1.75), using Eq. (2.5) to calculate the modal displacements within every resonator in terms of the deflection of its attachment points on the plates. Eq. (1.75) and the FE solution coincide at all points of the plates and within the resonators as well, confirming the accuracy of the proposed dynamic-stiffness approach.

Lastly, the accuracy of Eq. (1.74) to calculate the response in the time domain is assessed. To this purpose, a sine concentrated force $F \sin(\omega t)$,

for $F = 1\text{ N}$ and $\omega = 80\text{ Hz}$, is considered to be again applied at $\mathbf{x}_f = (0.05, 0.45)$ in the bottom plate. Figures 2.14-2.15 represent the time response as obtained by Eq. (1.74) and the FE method, at $\mathbf{x} = (0.05, -0.45)$ in the bottom plate during the time interval $[0, 1]\text{ s}$ (Figure 2.14) and over the whole system at $t = 1\text{ s}$ (Figure 2.15). In both cases, Eq. (1.74) and the FE solution can be hardly distinguished, confirming the validity of Eq. (1.74). For a final insight, Figure 2.16 illustrates the response within the line of the resonators along the line at $x = 0.05$, at $t = 1\text{ s}$, including the deflection of the plates. Again, Eq. (1.74) and the FE method provide the same results, confirming the accuracy of the proposed dynamic-stiffness approach.

Now, a final remark is that no significant differences are found in the results reported throughout this Section, by increasing the number of generalized coordinates (> 2208) and the number of FE elements (> 5100) here selected. Therefore, the relevant conclusion is that the proposed reduced-order dynamic-stiffness model provides very accurate results in terms of natural frequencies, modes, frequency and time responses with a limited number of generalized coordinates compared to the number of DOFs of a corresponding standard FE model. On the other hand, Eq. (1.74)-(1.75) are straightforward to implement and provide full insight into the response of the plates and the resonators as well.

Figure 2.11: Amplitude of the frequency response function (FRF) for concentrated harmonic load $1e^{i\omega t}$, $\omega = 101$ Hz, applied at $x_f = (0.05, 0.45)$ in the bottom plate, calculated by proposed reduced-order dynamic-stiffness model (DSM) and FE model in Abaqus (FEM): (a) Deflection of top plate by DSM (right column) and FEM (left column); (b) Deflection of bottom plate by DSM (right column) and FEM (left column); (c) Deflection of top/bottom plates and displacements of resonators at $x = 0.05$ by DSM (black continuous lines), FEM (black squares).



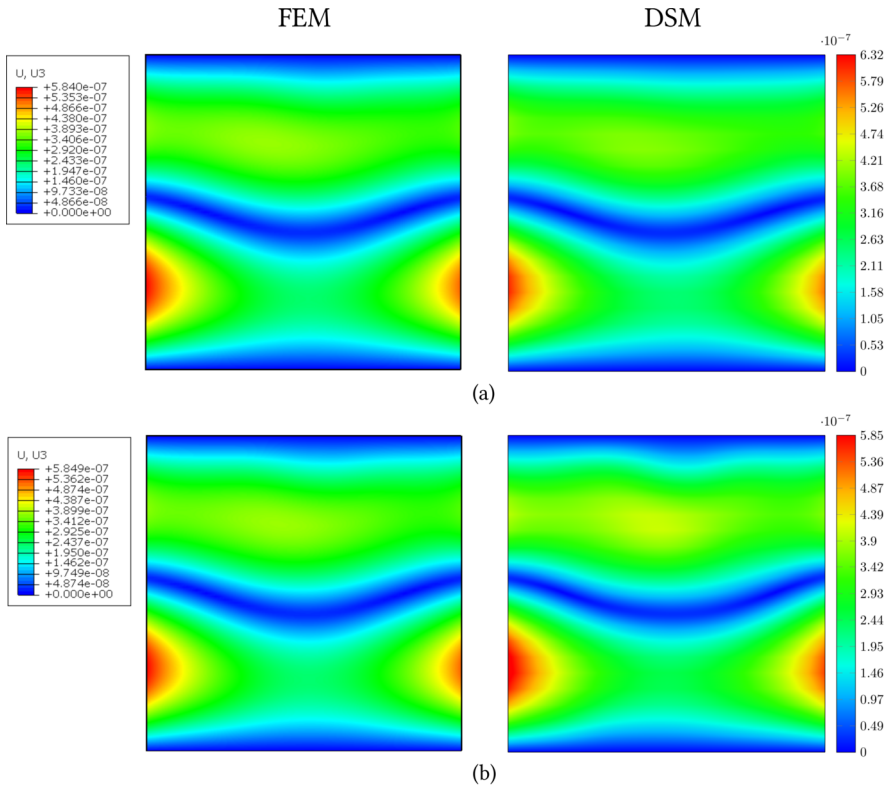


Figure 2.12: Amplitude of the frequency response function (FRF) for concentrated harmonic load $1e^{i\omega t}$, $\omega = 142.1$ Hz, applied at $\mathbf{x}_f = (0.05, 0.45)$ in the bottom plate, calculated by proposed reduced-order dynamic-stiffness model (DSM) and FE model in Abaqus (FEM): (a) Deflection of top plate by DSM (right column) and FEM (left column); (b) Deflection of bottom plate by DSM (right column) and FEM (left column); (c) Deflection of top/bottom plates and displacements of resonators at $x = 0.05$ by DSM (black continuous lines), FEM (black squares).

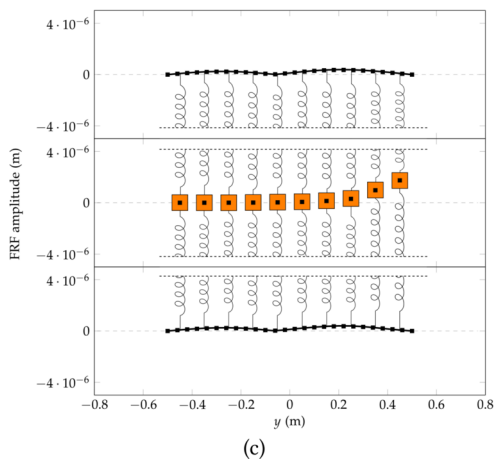
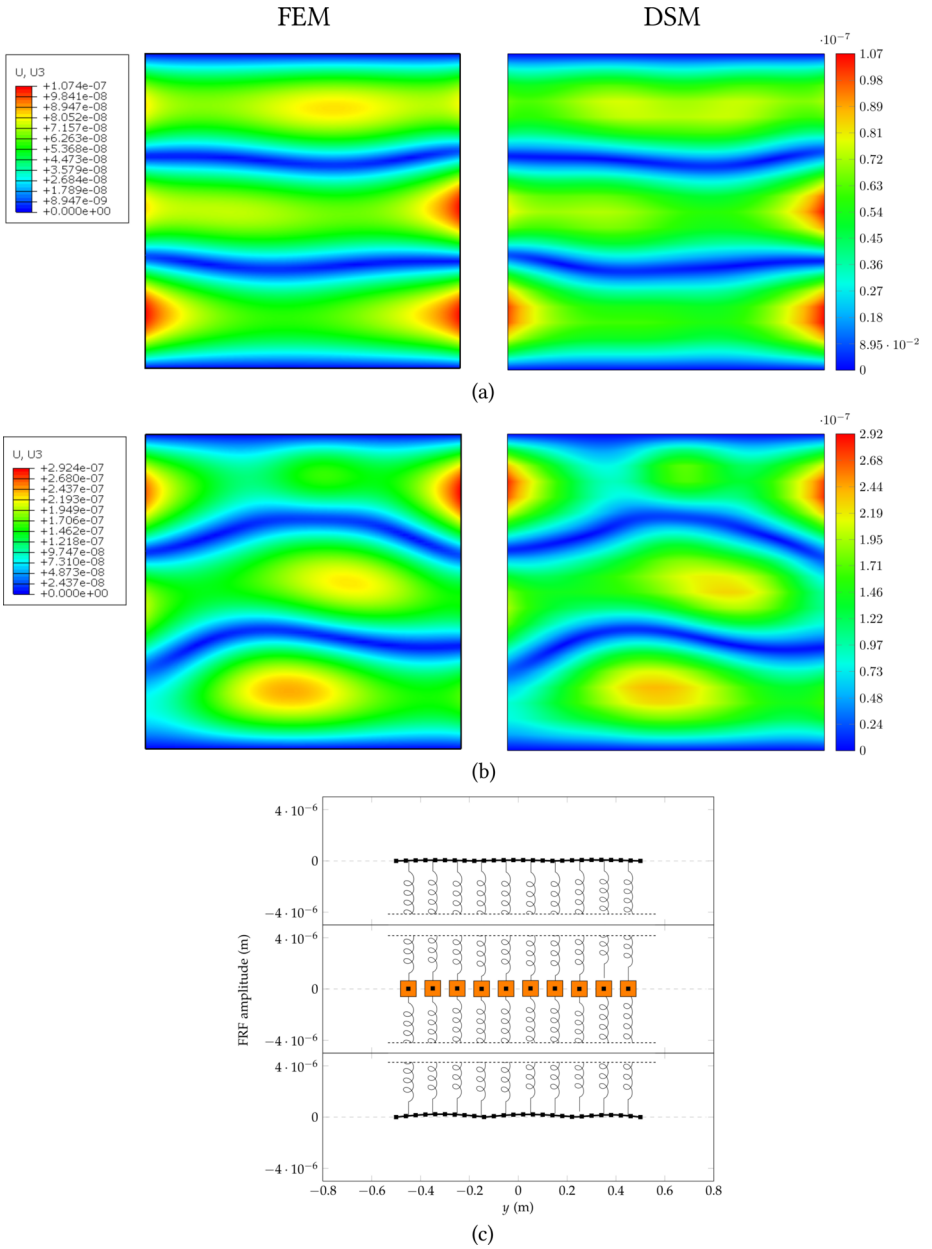


Figure 2.13: Amplitude of the frequency response function (FRF) for concentrated harmonic load $1e^{i\omega t}$, $\omega = 241.8$ Hz, applied at $x_f = (0.05, 0.45)$ in the bottom plate, calculated by proposed reduced-order dynamic-stiffness model (DSM) and FE model in Abaqus (FEM): (a) Deflection of top plate by DSM (right column) and FEM (left column); (b) Deflection of bottom plate by DSM (right column) and FEM (left column); (c) Deflection of top/bottom plates and displacements of resonators at $x = 0.05$ by DSM (black continuous lines), FEM (black squares).



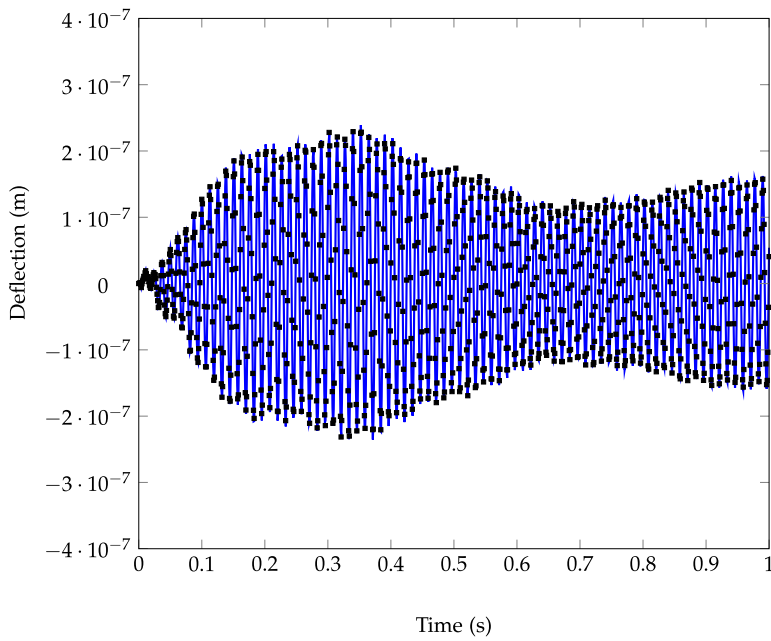
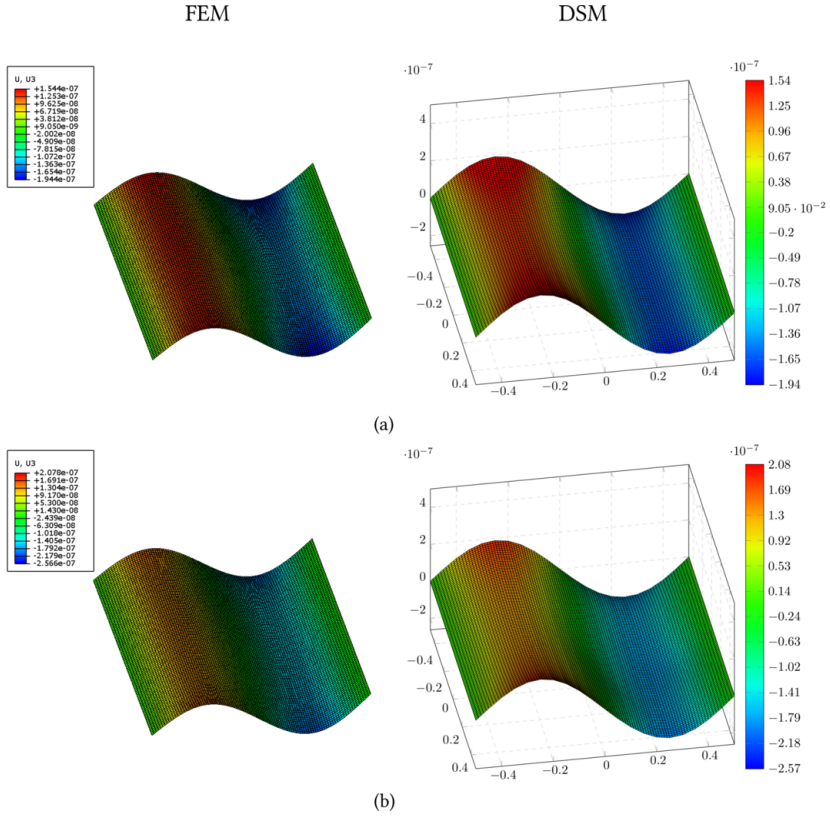


Figure 2.14: Time deflection at $\mathbf{x} = (0.05, -0.45)$ in the bottom plate for concentrated sine load $1 \sin(\omega t)$, $\omega = 80$ Hz, applied at $\mathbf{x}_f = (0.05, 0.45)$ in the bottom plate, calculated by proposed reduced-order dynamic-stiffness model (blue continuous line) and FE model in Abaqus (black squares).

Figure 2.15: Time deflection for concentrated sine load $1 \sin(\omega t)$, $\omega = 80$ Hz, applied at $\mathbf{x}_f = (0.05, 0.45)$ in the bottom plate, calculated at $t = 1$ s by proposed reduced-order dynamic-stiffness model (DSM) and FE model in Abaqus (FEM): (a) Deflection of top plate by DSM (right column) and FEM (left column); (b) Deflection of bottom plate by DSM (right column) and FEM (left column).



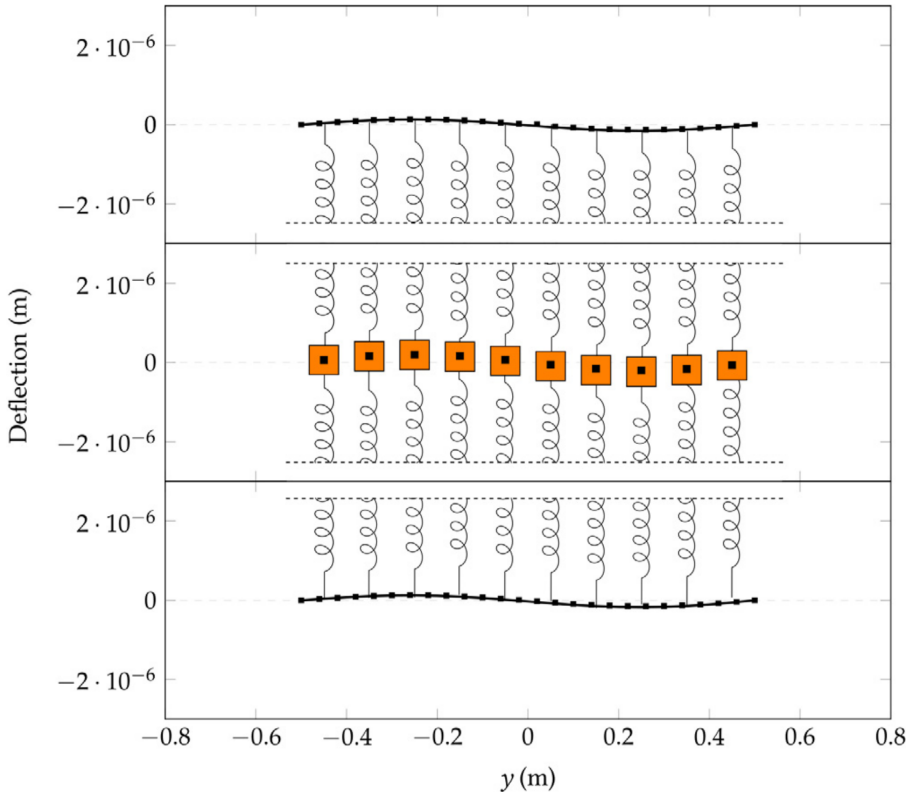


Figure 2.16: Time deflection of top/bottom plates and displacements of resonators at line $x = 0.05$ for concentrated sine load $1 \sin(\omega t)$, $\omega = 80$ Hz, applied at $\mathbf{x}_f = (0.05, 0.45)$ in the bottom plate, calculated at $t = 1$ s by proposed reduced-order dynamic-stiffness model (black continuous line) and FE model in Abaqus (black squares).

2.6 Conclusions

A new dynamic-stiffness model for evaluating the dynamic response of locally-resonant metamaterial plates has been presented in this chapter. Within the proposed framework, assemblies of plates coupled by periodic arrays of resonators are modelled with a reduced-order dynamic-stiffness model obtained by performing an exact dynamic condensation of the degrees of freedom within the resonators, which yields a frequency-dependent dynamic stiffness relating the reaction forces of the resonators to the deflections of their attachment points on the plates. The dynamic-stiffness matrix of the model-order reduction model is derived employing the spectral dynamic-stiffness method and it serves as basis to calculate the natural frequencies and the undamped modes by a modification of the Wittrick-Williams algorithm. Secondly, the orthogonality conditions for the modes of the plates only has been derived, leading to analytical expressions for the modal response under arbitrary load in time and frequency domains, under the assumption of classical damping. The numerical applications substantiate the accuracy and computational effectiveness of the proposed framework by comparison with the finite element results computed in Abaqus.

The proposed approach presents itself as an effective framework for modelling locally-resonant metamaterial plates of emerging interest in engineering, to which several studies have been devoted addressing in particular a two-plate system with an internal array of resonators such as the 1-DOF mass-spring resonators in ref. [60], 1-DOF mass-spring resonators consisting of mass-spring subsystems in parallel with springs in ref. [63] or the mass-spring-truss assemblies in ref. [81].

WAVE PROPAGATION IN NONLOCAL RAYLEIGH LATTICES

In this chapter the wave propagation in nonlocal Rayleigh lattices is addressed. Upon building the exact dynamic-stiffness matrix of a nonlocal beam element, the band structure of the lattice is calculated by means of the Bloch's theorem. Furthermore, a finite-element formulation, derived by introducing an ad-hoc procedure for constructing a set of shape functions satisfying the static governing equations of each lattice member, is introduced.

3.1 Wave propagation in nonlocal lattices

The study of the propagation of free elastic waves in nonlocal lattices is performed by applying the Bloch's theorem to the frequency-domain equilibrium equations of the reference unit cell. In Figure 3.1, the reference

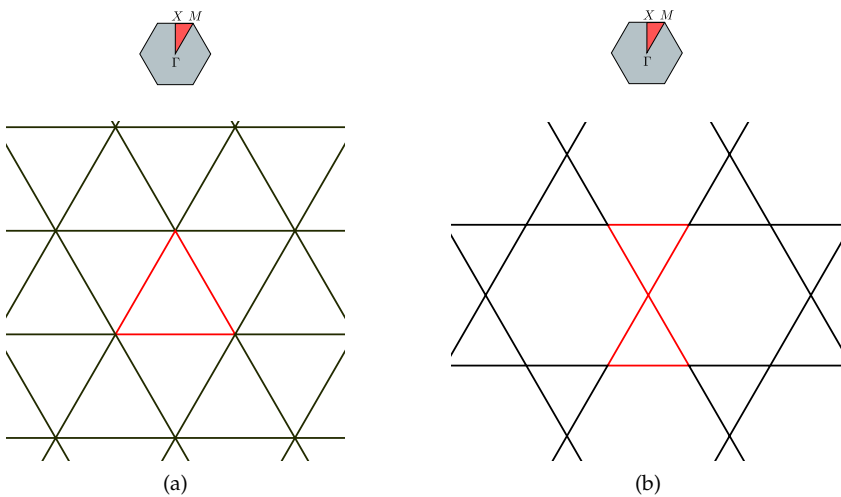
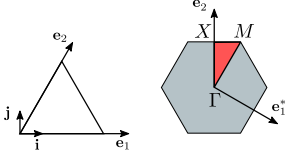
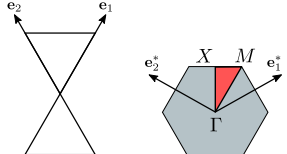


Figure 3.1: Periodic planar beam lattices: (a) triangular lattice, (b) Kagome lattice.

unit cell of two periodic planar beam lattices is highlighted in red and the

corresponding Brillouin zone and irreducible Brillouin zones are reported on top. In particular the basis vectors of the direct and reciprocal lattices, respectively denoted with $\{\mathbf{e}_1, \mathbf{e}_2\}$ and $\{\mathbf{e}_1^*, \mathbf{e}_2^*\}$, are reported in Table 3.1 [62].

Table 3.1: Basis vectors of the triangular and Kagome lattices. l denotes the length of each lattice member.

Topology	Direct lattice	Reciprocal lattice
	$\mathbf{e}_1 = l\mathbf{i}$ $\mathbf{e}_2 = l\left(\frac{1}{2}\mathbf{i} + \frac{\sqrt{3}}{2}\mathbf{j}\right)$	$\mathbf{e}_1^* = \frac{1}{l}\left(\mathbf{i} - \frac{1}{\sqrt{3}}\mathbf{j}\right)$ $\mathbf{e}_2^* = \frac{1}{l}\frac{2}{\sqrt{3}}\mathbf{j}$
	$\mathbf{e}_1 = 2l\left(\frac{1}{2}\mathbf{i} + \frac{\sqrt{3}}{2}\mathbf{j}\right)$ $\mathbf{e}_2 = 2l\left(-\frac{1}{2}\mathbf{i} + \frac{\sqrt{3}}{2}\mathbf{j}\right)$	$\mathbf{e}_1^* = \frac{1}{2l}\left(\mathbf{i} + \frac{1}{\sqrt{3}}\mathbf{j}\right)$ $\mathbf{e}_2^* = \frac{1}{2l}\left(-\mathbf{i} + \frac{1}{\sqrt{3}}\mathbf{j}\right)$

The size effects is captured by modelling every lattice member within the unit cell with the stress-driven nonlocal elasticity theory [64, 65] here formulated in conjunction with the Rayleigh beam theory. As basis for applying the Bloch's theorem, the governing equations of the unit cells are represented in terms of dynamic-stiffness matrix. For this purpose, consider the axial and bending equilibrium equations of a lattice member in the frequency domain, along with the associated constitutive boundary conditions (BCs) [20, 64, 65]:

$$-EA \cdot L_c^2 \left(u^{(4)} - \frac{1}{L_c^2} u^{(2)} \right) + \rho A \omega^2 u = 0 \quad (3.1)$$

$$\eta^{(1)}(0) = \frac{1}{L_c} \eta(0), \quad \eta^{(1)}(l) = -\frac{1}{L_c} \eta^{(1)}(l) \quad (3.2a,b)$$

$$-EI \cdot L_c^2 \left(v^{(6)} - \frac{1}{L_c^2} v^{(4)} \right) - \rho I \omega^2 v^{(2)} + \rho A \omega^2 u = 0 \quad (3.3)$$

$$\chi^{(1)}(0) = \frac{1}{L_c} \eta(0), \quad \chi^{(1)}(l) = -\frac{1}{L_c} \eta^{(1)}(l) \quad (3.4a,b)$$

where the superscript k denotes the k^{th} derivative with respect to the spatial coordinate x , ω is the frequency, u is the axial displacement and v the deflection in the local reference system of the member, η the axial strain and χ the curvature; l is the length of the member, E the Young's modulus, A the area of the cross section, I the moment of inertia, ρ the mass per unit volume. Further, L_c is the internal length of the stress-driven model, governing nonlocal effects.

Eq. (3.1) and Eq. (3.3) are obtained from the classical equilibrium equations of the Rayleigh beam

$$N^{(1)} + \rho A \omega^2 u = 0 \quad (3.5)$$

$$M^{(2)} - \rho I \omega^2 v^{(2)} + \rho A \omega^2 v = 0 \quad (3.6)$$

where the following expressions, derived from the stress-driven nonlocal elasticity theory [64, 65], are used for the axial force N and the bending moment M :

$$N = -EA \cdot L_c^2 \left(\eta^2 - \frac{1}{L_c^2} \eta \right) \quad (3.7)$$

$$M = -EI \cdot L_c^2 \left(\chi^2 - \frac{1}{L_c^2} \chi \right) \quad (3.8)$$

begin $\eta = u^{(1)}$, $\chi = -v^{(2)}$, $\theta = -v^{(1)}$ the rotation.

The dynamic-stiffness matrix of the unit cell is written by making use of Eq. (3.1) through Eq. (3.4). Here, two different approaches are used:

- 1) The exact dynamic-stiffness approach is based on modelling every lattice member by a unique two-node beam element, using the exact solutions of Eq. (3.1) through Eq. (3.4). In this case, the frequency-domain equilibrium equations of the unit cell in the global reference system take the form

$$\mathbf{D}(\omega) \mathbf{q} = \mathbf{0} \quad (3.9)$$

where $\mathbf{D}(\omega)$ is the exact dynamic-stiffness matrix of the cell and \mathbf{q} is the vector collecting displacements of the member-to-member nodes only.

- 2) The finite-element dynamic-stiffness approach, every lattice member is divided into a number n of two-node beam elements and pertinent stiffness and mass matrices are formulated. In this case, the frequency-domain equilibrium equations of the unit cell in the global reference

system are

$$(\mathbf{K} - \omega^2 \mathbf{M}) \mathbf{q} = \mathbf{0} \quad (3.10)$$

where \mathbf{K} and \mathbf{M} are the stiffness and mass matrices of the unit cell, while \mathbf{q} is the vector collecting displacements of all nodes within the cell; unlike the dynamic-stiffness approach, in this case \mathbf{q} includes not only the displacements of the member-to-member nodes but also those of the nodes along the lattice members.

Based on the Bloch's theorem Bloch's theorem [62], the following transformation enforces the Bloch's periodic boundary conditions on the degrees of freedom involved in Eqs. (3.9)-(3.10):

$$\mathbf{q} = \mathbf{T} \tilde{\mathbf{q}} = \begin{bmatrix} \mathbf{I} & \mathbf{0} & \mathbf{0} & \mathbf{0} \\ \mathbf{I}e^{k_1} & \mathbf{0} & \mathbf{0} & \mathbf{0} \\ \mathbf{0} & \mathbf{I} & \mathbf{0} & \mathbf{0} \\ \mathbf{0} & \mathbf{I}e^{k_2} & \mathbf{0} & \mathbf{0} \\ \mathbf{0} & \mathbf{0} & \mathbf{I} & \mathbf{0} \\ \mathbf{0} & \mathbf{0} & \mathbf{I}e^{k_1} & \mathbf{0} \\ \mathbf{0} & \mathbf{0} & \mathbf{I}e^{k_2} & \mathbf{0} \\ \mathbf{0} & \mathbf{0} & \mathbf{I}e^{k_1+k_2} & \mathbf{0} \\ \mathbf{0} & \mathbf{0} & \mathbf{0} & \mathbf{I} \end{bmatrix}; \quad \tilde{\mathbf{q}} = \begin{bmatrix} \mathbf{q}_l \\ \mathbf{q}_b \\ \mathbf{q}_{lb} \\ \mathbf{q}_i \end{bmatrix} \quad (3.11)$$

where $k_1 = \tilde{\mathbf{k}} \cdot \mathbf{e}_1 = \delta_1 + i\epsilon_1$ and $k_2 = \tilde{\mathbf{k}} \cdot \mathbf{e}_2 = \delta_2 + i\epsilon_2$ are the components of the wave vector $\tilde{\mathbf{k}}$ along the basis vectors \mathbf{e}_1 and \mathbf{e}_2 of the direct lattice, $\tilde{\mathbf{q}}$ collects the nodal displacements in the so-called Bloch reduced coordinates. Eqs. (3.30)-(3.10) refer to the general form of unit cell in Fig. 3.2, which encompasses the unit cells of the lattices in Fig. 3.1 where the subscripts l, r, b, t are related to the nodes shared with the neighbouring cells, the double subscripts are referred to the corner nodes and the subscript i to the (internal) nodes within the cell. Substituting Eq. (3.11) for \mathbf{q} in either Eq. (3.9) or Eq. (3.10) and pre-multiplying the resulting equations with the Hermitian transpose \mathbf{T}^H , the following eigenvalue problems are formulated in the reduced coordinates [62]:

$$\tilde{\mathbf{D}}(\omega, k_1, k_2) \tilde{\mathbf{q}} = \mathbf{0} \quad (3.12)$$

$$\left(\tilde{\mathbf{K}}(k_1, k_2) - \omega^2 \tilde{\mathbf{M}}(k_1, k_2) \right) \tilde{\mathbf{q}} = \mathbf{0} \quad (3.13)$$

being $\tilde{\mathbf{D}}(\omega, k_1, k_2) = \mathbf{T}^H \mathbf{D} \mathbf{T}$, $\tilde{\mathbf{K}}(k_1, k_2) = \mathbf{T}^H \mathbf{K} \mathbf{T}$, $\tilde{\mathbf{M}}(k_1, k_2) = \mathbf{T}^H \mathbf{M} \mathbf{T}$.

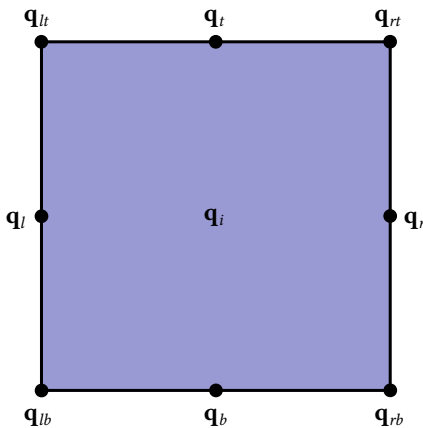


Figure 3.2: Degrees of freedom of a unit cell for a generic two-dimensional periodic structure, as taken from ref. [62].

Focusing on wave motion without attenuation, for which k_1 and k_2 are purely imaginary of the form $k_1 = i\epsilon_1$ and $k_2 = i\epsilon_2$, the frequency of wave propagation ω is obtained as solution of the eigenvalue problems (3.12) and (3.13). As customary, ω is calculated for (ϵ_1, ϵ_2) along the edges of the first Brillouin zone.

3.2 Exact dynamic-stiffness approach

Consider the generic member of the lattice in Fig. 3.3 subjected to harmonic forces/moments at the ends. In the proposed exact dynamic-stiffness approach the lattice member is treated as a unique two-node beam element and its two ends, i.e. its nodes, have 3 degrees of freedom each, 2 translations and 1 rotation.

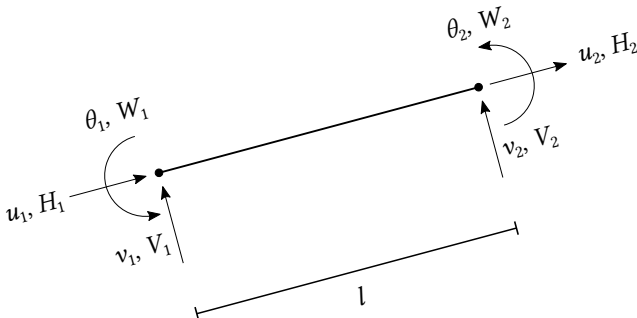


Figure 3.3: Dynamic-stiffness approach: Stress-driven nonlocal lattice member modelled by a unique two-node beam element.

For generality, the dynamic-stiffness matrix of the lattice member is sought in terms of dimensionless frequencies [4, 8, 17, 18]. As a conse-

quence, Eq. (3.1) through Eq. (3.6) governing the steady-state responses under harmonic forces/moments at the ends are:

$$(\mathcal{L}_a + \omega_a^2 \mathcal{I})[u] = 0, \quad \mathcal{L}_a = -\lambda^2 \frac{d^4}{d\bar{\zeta}^4} + \frac{d^2}{d\bar{\zeta}^2}, \quad \bar{\zeta} \in [0, 1] \quad (3.14)$$

$$\left. \frac{d\eta}{d\bar{\zeta}} \right|_{\bar{\zeta}=0} = \frac{1}{\lambda} \eta(0), \quad \left. \frac{d\eta}{d\bar{\zeta}} \right|_{\bar{\zeta}=1} = -\frac{1}{\lambda} \eta(1) \quad (3.15a,b)$$

$$(\mathcal{L}_b + \omega_b^2 \mathcal{M} + \omega_b^4 \mathcal{I})[u] = 0, \quad \mathcal{L}_b = \lambda^2 \frac{d^6}{d\bar{\zeta}^6} - \frac{d^4}{d\bar{\zeta}^4}, \quad \mathcal{M} = -\frac{d^2}{d\bar{\zeta}^2}, \quad \bar{\zeta} \in [0, 1] \quad (3.16)$$

$$\left. \frac{d\chi}{d\bar{\zeta}} \right|_{\bar{\zeta}=0} = \frac{1}{\lambda} \chi(0), \quad \left. \frac{d\chi}{d\bar{\zeta}} \right|_{\bar{\zeta}=1} = -\frac{1}{\lambda} \chi(1) \quad (3.17a,b)$$

where $d^k/d\bar{\zeta}^k$ denotes the k^{th} derivative with respect to the dimensionless spatial coordinate $\bar{\zeta}$, $\bar{\zeta} = x/l$ being x the spatial coordinate, $\omega_a = [\rho A(\omega l)^2/EI]^{1/2}$, $\omega_b = [\rho A(\omega l^2)^2/EI]^{1/4}$, $\omega_\rho = [\rho(\omega l)^2/E]^{1/2}$, \mathcal{I} is the identity map; further, $\lambda = L_c/l$ is the dimensionless internal length governing non-local effects.

It is noticed that the solutions of Eq. (3.14) and Eq. (3.16), which fulfil the constitutive BCs (3.15) and (3.17), can be cast in the form

$$u(\bar{\zeta}) = \sum_{k=1}^2 c_{a,k} f_k(\bar{\zeta}) \quad (3.18)$$

$$v(\bar{\zeta}) = \sum_{k=1}^4 c_{b,k} g_k(\bar{\zeta}) \quad (3.19)$$

where $c_{a,k}$ for $k = 1, 2$ and $c_{b,k}$ for $k = 1, \dots, 4$ are integration constants depending on the classical static/kinematic BCs, while $f_k(\bar{\zeta}) = f_k(\bar{\zeta}, \omega_a)$ and $g_k(\bar{\zeta}) = g_k(\bar{\zeta}, \omega_b, \omega_\rho)$ are closed analytical functions depending on the lattice member parameters and the frequency. Making use of Eq. (3.18) and Eq. (3.19), the whole set of response variables is readily available in the

following analytical forms:

$$u = u(\xi, \mathbf{c}_a) \quad (3.20)$$

$$N = -\frac{EA \cdot \lambda^2}{l} \left(\frac{d^3 u(\xi)}{d\xi^3} - \frac{1}{\lambda^2} \frac{du(\xi)}{d\xi} \right) = N(\xi, \mathbf{c}_a) \quad (3.21)$$

$$v = v(\xi, \mathbf{c}_b) \quad (3.22)$$

$$\theta = -\frac{1}{l} \frac{dv}{d\xi} = \theta(\xi, \mathbf{c}_b) \quad (3.23)$$

$$M = \frac{EI \cdot \lambda^2}{l^2} \left(\frac{d^4 v(\xi)}{d\xi^4} - \frac{1}{\lambda^2} \frac{d^2 v(\xi)}{d\xi^2} \right) = M(\xi, \mathbf{c}_b) \quad (3.24)$$

$$T = \frac{EI \cdot \lambda^2}{l^3} \left(\frac{d^5 v(\xi)}{d\xi^5} - \frac{1}{\lambda^2} \frac{d^3 v(\xi)}{d\xi^3} \right) - \frac{\rho I \omega^2}{l} \frac{dv(\xi)}{d\xi} = T(\xi, \mathbf{c}_b) \quad (3.25)$$

being $\mathbf{c}_a = [c_{a,1} \ c_{a,2}]^T$ and $\mathbf{c}_b = [c_{b,1} \ c_{b,2} \ c_{b,3} \ c_{b,4}]^T$. Eq. (3.20) through Eq. (3.25) are the basis to derive the dynamic-stiffness matrix of the lattice member. Indeed, being

$$\mathbf{d}_e = [u_1 \ u_2 \ v_1 \ \theta_1 \ v_2 \ \theta_2]^T = [u(0) \ u(1) \ v(0) \ \theta(0) \ v(1) \ \theta(1)]^T \quad (3.26)$$

$$\mathbf{p}_e = [H_1 \ H_2 \ V_1 \ W_1 \ V_2 \ W_2]^T = [-N(0) \ N(1) \ -T(0) \ -M(0) \ T(1) \ M(1)]^T \quad (3.27)$$

the vectors of nodal displacements and forces, computing Eq. (3.20) through Eq. (3.25) at $\xi = 0$ and $\xi = 1$ yields

$$\mathbf{d}_e = \mathbf{A}_e \mathbf{c} \quad (3.28)$$

$$\mathbf{p}_e = \mathbf{B}_e \mathbf{c} \quad (3.29)$$

where $\mathbf{c} = [c_a \ c_b]^T$. Next, using Eq. (3.28) to calculate $\mathbf{c} = \mathbf{A}_e^{-1} \mathbf{d}_e$ and substituting for \mathbf{c} in Eq. (3.29) leads to

$$\mathbf{p}_e = \mathbf{B}_e \mathbf{A}_e^{-1} \mathbf{d}_e = \mathbf{D}_e \mathbf{d}_e \quad (3.30)$$

where

$$\mathbf{D}_e(\omega) = \begin{bmatrix} \mathbf{D}_{e,a}(\omega_a(\omega)) & \mathbf{0} \\ \mathbf{0} & \mathbf{D}_{e,b}(\omega_b(\omega), \omega_\rho(\omega)) \end{bmatrix} \quad (3.31)$$

being $\mathbf{D}_{e,a}$ and $\mathbf{D}_{e,b}$ the block matrices associated with axial and bending responses, respectively. The matrix \mathbf{D}_e in Eq. (3.31) is the dynamic-stiffness

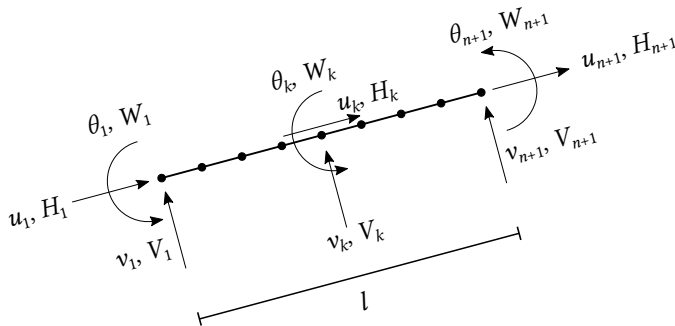
matrix of the two-node lattice member in Fig. 3.3, as modelled according to the stress-driven nonlocal elasticity theory in conjunction with the Rayleigh beam theory. It is noteworthy that the matrix \mathbf{D}_e is available in a closed analytical form, as the inverse matrix \mathbf{A}_e^{-1} in Eq. (3.30) can be obtained symbolically from the inverses of the two separate block matrices associated with axial and bending responses [27]. Furthermore, the matrix \mathbf{D}_e is exact, because is based on the exact solutions of the stress-driven differential equations of motion (3.14) and (3.16) along with the constitutive Bcs (3.15) and (3.17). Indeed, no approximations are made in building the solutions (3.18) and (3.19).

The dynamic-stiffness matrix of the unit cell $\mathbf{D}(\omega)$ in Eq. (3.9) is finally obtained by a finite-element-like assembling procedure of the dynamic-stiffness matrices of every member of the unit cell in the global reference system. The size of $\mathbf{D}(\omega)$ is equal to $(3 \times M_n) \times (3 \times M_n)$, where M_n is the number of member-to-member nodes within the unit cell. On constructing $\mathbf{D}(\omega)$ in Eq. (3.9), the wave dispersion analysis is carried out solving the eigenvalue problem (3.12) for the frequency ω corresponding to wave vectors along the edges of the first Brillouin zone. The eigenvalue problem is nonlinear in ω and is solved, here, by the so-called contour-integral algorithm illustrated in Section 1.3.2.

3.3 Finite-element approach

Consider the generic member of the lattice in Fig. 3.4 and assume it is divided in an arbitrary number n of two-node beam elements. Each node has 3 degrees of freedom, 2 translations and 1 rotation. Here, to build the stiffness matrix and the mass matrix of the lattice member the principle of virtual work is used.

Figure 3.4: Finite-element approach: Stress-driven nonlocal lattice member modelled by n two-node beam elements.



Given the numbering of nodal displacements reported in Fig. 3.4, be

$$\mathbf{u}_e = [\mathbf{u}_{e,a} \quad \mathbf{u}_{e,b}]^T \quad (3.32)$$

$$\mathbf{u}_{e,a} = [u_1 \quad u_2 \quad \dots \quad u_{n+1}]^T \quad (3.33)$$

$$\mathbf{u}_{e,b} = [v_1 \quad \theta_1 \quad v_2 \quad \theta_2 \quad \dots \quad v_{n+1} \quad \theta_{n+1}]^T \quad (3.34)$$

$$\mathbf{f}_e = [\mathbf{f}_{e,a} \quad \mathbf{f}_{e,b}]^T \quad (3.35)$$

$$\mathbf{f}_{e,a} = [H_1 \quad H_2 \quad \dots \quad H_{n+1}]^T \quad (3.36)$$

$$\mathbf{f}_{e,b} = [V_1 \quad W_1 \quad V_2 \quad W_2 \quad \dots \quad V_{n+1} \quad W_{n+1}]^T \quad (3.37)$$

the vectors of nodal displacements and forces. As assumed in Section 3.2, the lattice member are subjected to harmonic forces/moments at the ends, i.e. $H_2 = H_3 = \dots = H_n = 0$, $V_2 = V_3 = \dots = V_n = 0$ and $W_2 = W_3 = \dots = W_n = 0$.

The identities of external and internal works for the axial and bending problems separately read

$$l \int_0^1 \left(-\lambda^2 \frac{d^3 u}{d\xi^3} + \frac{du}{d\xi} \right) \delta\eta \, d\xi - \omega_a^2 l \int_0^1 u \delta u \, d\xi = \widehat{\mathbf{f}}_{e,a}^T \delta \mathbf{u}_{e,a} \quad (3.38)$$

$$l \int_0^1 \left(\lambda^2 \frac{d^4 v}{d\xi^4} - \frac{d^2 v}{d\xi^2} \right) \delta\chi \, d\xi - \omega_b^4 l \int_0^1 v \delta v \, d\xi - \omega_\rho^2 l \int_0^1 \frac{dv}{d\xi} \delta\theta \, d\xi = \widehat{\mathbf{f}}_{e,b}^T \delta \mathbf{u}_{e,b} \quad (3.39)$$

where $\delta \mathbf{u}_{e,a}$ and $\delta \mathbf{u}_{e,b}$ are virtual nodal displacements, $\delta\eta$ and $\delta\chi$ the corresponding virtual axial strain and curvature, $\widehat{\mathbf{f}}_{e,a} = (l^3/EA)\mathbf{f}_{e,a}$ and $\widehat{\mathbf{f}}_{e,b} = (l^4/EI)\mathbf{f}_{e,b}$. For the axial displacement u and the bending deflection v , the following expressions are adopted

$$u(\xi) = \mathbf{\Psi}_{e,a}(\xi) \mathbf{u}_{e,a} \quad (3.40)$$

$$v(\xi) = \mathbf{\Psi}_{e,b}(\xi) \mathbf{u}_{e,b} \quad (3.41)$$

where $\mathbf{\Psi}_{e,a}$ and $\mathbf{\Psi}_{e,b}$ are matrices of shape functions given as

$$\mathbf{\Psi}_{e,a}(\xi) = \text{diag}(\psi_1, \psi_2, \dots, \psi_{n+1}) \quad (3.42)$$

$$\mathbf{\Psi}_{e,b}(\xi) = \text{diag}(\beta_1, \beta_2, \dots, \beta_{2n+1}, \beta_{2n+2}) \quad (3.43)$$

Replacing Eq. (3.40) for u , Eq. (3.41) for v and enforcing the identities (3.38) and (3.39) for any virtual nodal displacements provide the following equations

$$(\widehat{\mathbf{K}}_{e,a} - \omega_a^2 \widehat{\mathbf{M}}_{e,a}) = \widehat{\mathbf{f}}_{e,a} \quad (3.44)$$

$$(\widehat{\mathbf{K}}_{e,b} - \omega_\rho^2 \widehat{\mathbf{M}}_{e,\rho} - \omega_b^4 \widehat{\mathbf{M}}_{e,b}) = \widehat{\mathbf{f}}_{e,b} \quad (3.45)$$

where

$$(\widehat{\mathbf{K}}_{e,a})_{ij} = l \int_0^1 \left(-\lambda^2 \frac{d\psi_i}{d\zeta} \frac{d^3\psi_j}{d\zeta^3} + \frac{d\psi_i}{d\zeta} \frac{d\psi_j}{d\zeta} \right) d\zeta \quad (3.46)$$

$$(\widehat{\mathbf{M}}_{e,a})_{ij} = l \int_0^1 \psi_i \psi_j d\zeta \quad (3.47)$$

$$(\widehat{\mathbf{K}}_{e,b})_{ij} = l \int_0^1 \left(-\lambda^2 \frac{d^2\beta_i}{d\zeta^2} \frac{d^4\beta_j}{d\zeta^4} + \frac{d^2\beta_i}{d\zeta^2} \frac{d^2\beta_j}{d\zeta^2} \right) d\zeta \quad (3.48)$$

$$(\widehat{\mathbf{M}}_{e,b})_{ij} = l \int_0^1 \beta_i \beta_j d\zeta \quad (3.49)$$

$$(\widehat{\mathbf{M}}_{e,\rho})_{ij} = l \int_0^1 \frac{d\beta_i}{d\zeta} \frac{d\beta_j}{d\zeta} d\zeta \quad (3.50)$$

The shape functions ψ_i 's and β_i 's involved in Eq. (3.46) through Eq. (3.50) are built making use of the exact solution of the static equilibrium equations of the beam.

For the axial problem, the i^{th} shape function ψ_i in Eq. (3.42) for $\Psi_{e,a}$ is the axial displacement corresponding to the axial nodal displacement $u_i = 1$ at node i , zero displacements at all the other nodes $k \neq i$ and fulfilling the BCs (3.15). The shape function ψ_i is calculated starting from the following expression:

$$\psi_i(\zeta) = g_{a,1}^{[i]} + g_{a,2}^{[i]} \zeta + g_{a,3}^{[i]} \lambda^2 e^{\zeta/\lambda} + g_{a,4}^{[i]} \lambda^2 e^{-\zeta/\lambda} + \sum_{j=2}^n \mathcal{G}_a(\zeta, \zeta_j) H_j^{[i]} \quad (3.51)$$

where $g_{a,k}^{[i]}$ for $k = 1, \dots, 4$ are integration constants, $H_j^{[i]}$ nodal axial forces ensuring equilibrium at the nodes and $\mathcal{G}_a(\zeta, y)$ is given as:

$$\mathcal{G}_a(\zeta, y) = \left[y - \zeta + \frac{\lambda}{2} \left(e^{(\zeta-y)/\lambda} - e^{-(\zeta-y)/\lambda} \right) \right] \mathcal{H}(\zeta - y) \quad (3.52)$$

where $\mathcal{H}(\xi - y)$ is the unit step function. Notably, \mathcal{G}_a in Eq. (3.52) is the particular integral of the following differential equation for static equilibrium under a unit axial force at $\xi = y$, as obtained by applying direct and inverse Laplace Transforms [69]:

$$\mathcal{L}_a[\mathcal{G}_a(\xi, y)] + \delta(\xi - y) = 0 \quad (3.53)$$

where symbol $\delta(\xi - y)$ denotes a Dirac's delta at $\xi = y$; further the first four terms in Eq. (3.51) are the solution of the homogeneous differential equation associated to Eq. (3.53). To define ψ_i in Eq. (3.51), the integration constant $g_{a,k}^{[i]}$ and the nodal forces $H_j^{[i]}$ are computed enforcing the following conditions: (a) $u_i = 1$ at the node i and zero displacements at all the other nodes; (b) the constitutive BCs (3.15). These conditions correspond to the following set of algebraic equations respectively

$$\mathbf{\Omega}_a \mathbf{g}_a^{[i]} + \mathbf{G}_a \mathbf{h}^{[i]} = \mathbf{u}_a^{[i]} \quad (3.54)$$

and

$$\mathbf{\Omega}_{a\lambda} \mathbf{g}_a^{[i]} + \mathbf{G}_{a\lambda} \mathbf{h}^{[i]} = \mathbf{0} \quad (3.55)$$

where $\mathbf{g}_a^{[i]} = [g_{a,1}^{[i]} \ g_{a,2}^{[i]} \ g_{a,3}^{[i]} \ g_{a,4}^{[i]}]^\top$, $\mathbf{h}^{[i]} = [H_2^{[i]} \ H_3^{[i]} \ \dots \ H_n^{[i]}]^\top$ and $\mathbf{u}_a^{[i]}$ is the vector with all components equal to zero except for the i^{th} one, which is equal to 1.

The matrices $\mathbf{\Omega}_a$ and $\mathbf{\Omega}_{a\lambda}$ in Eqs. (3.54)-(3.55) are defined as

$$\mathbf{\Omega}_a = \begin{bmatrix} \omega_a(0)^\top \\ \omega_a(\xi_2)^\top \\ \vdots \\ \omega_a(\xi_n)^\top \\ \omega_a(1)^\top \end{bmatrix}; \quad \mathbf{\Omega}_{a\lambda} = \begin{bmatrix} \omega_{a,2}(0)^\top - \frac{1}{\lambda} \omega_{a,1}(0)^\top \\ \omega_{a,2}(1)^\top + \frac{1}{\lambda} \omega_{a,1}(1)^\top \end{bmatrix} \quad (3.56)$$

being the functions ω_a , $\omega_{a,1}$, $\omega_{a,2}$ in Eq. (3.56) defined as

$$\begin{aligned} \omega_a(\xi) &= [1 \quad \xi \quad \lambda^2 e^{\xi/\lambda} \quad \lambda^2 e^{-\xi/\lambda}]^\top \\ \omega_{a,1}(\xi) &= \frac{d\omega_a(\xi)}{d\xi} = [0 \quad 1 \quad \lambda e^{\xi/\lambda} \quad -\lambda e^{-\xi/\lambda}]^\top \\ \omega_{a,2}(\xi) &= \frac{d^2\omega_a(\xi)}{d\xi^2} = [0 \quad 0 \quad e^{\xi/\lambda} \quad e^{-\xi/\lambda}]^\top \end{aligned} \quad (3.57)$$

Further, the matrices \mathbf{G}_a and $\mathbf{G}_{a\lambda}$ in Eq. (3.54)-(3.55) are given as

$$(\mathbf{G}_a)_{ij} = \mathcal{G}_a(\xi_i, \xi_j) \quad i = 1, \dots, n+1; j = 2, \dots, n$$

$$\mathbf{G}_{a\lambda} = \begin{bmatrix} \gamma_{a,1}(0) - \frac{1}{\lambda} \gamma_{a,1}(0) \\ \gamma_{a,1}(1) + \frac{1}{\lambda} \gamma_{a,1}(1) \end{bmatrix} \quad (3.58)$$

being

$$\gamma_{a,1}(\xi) = \begin{bmatrix} \frac{\partial \mathcal{G}_a(\xi, y)}{\partial \xi} \Big|_{y=\xi_2} & \cdots & \frac{\partial \mathcal{G}_a(\xi, y)}{\partial \xi} \Big|_{y=\xi_n} \\ \frac{\partial \mathcal{G}_a(\xi, y)}{\partial \xi} \Big|_{y=\xi_2} & \cdots & \frac{\partial \mathcal{G}_a(\xi, y)}{\partial \xi} \Big|_{y=\xi_n} \end{bmatrix} \quad (3.59)$$

Combining Eq. (3.54) and Eq. (3.55) the following linear system is obtained

$$\begin{bmatrix} \mathbf{\Omega}_a & \mathbf{G}_a \\ \mathbf{\Omega}_{a\lambda} & \mathbf{G}_{a\lambda} \end{bmatrix} \begin{bmatrix} \mathbf{g}_a^{[i]} \\ \mathbf{h}^{[i]} \end{bmatrix} = \begin{bmatrix} \mathbf{u}_a^{[i]} \\ \mathbf{0} \end{bmatrix} \quad (3.60)$$

whose solution $\mathbf{g}_a^{[i]}$ and $\mathbf{h}^{[i]}$ fully define the shape function ψ_i in Eq. (3.51).

For the bending problem, a similar approach holds. The i^{th} shape function β_i in Eq. (3.43) for $\Psi_{e,b}$ is the deflection corresponding to a unit nodal displacement at node m (unit deflection if $i = 2m - 1$ or unit rotation if $i = 2m$), zero displacements at all the other nodes and fulfilling the constitutive BCs (3.17). It can be evaluated as

$$\beta_i(\xi) = g_{b,1}^{[i]} + g_{b,2}^{[i]} \xi + g_{b,3}^{[i]} \xi^2 + g_{b,4}^{[i]} \xi^3 + g_{b,5}^{[i]} \lambda^4 e^{\xi/\lambda} + g_{b,6}^{[i]} \lambda^4 e^{-\xi/\lambda} + \sum_{j=2}^n \mathcal{G}_b^V(\xi, \xi_j) V_j^{[i]} + \sum_{j=2}^n \mathcal{G}_b^W(\xi, \xi_j) W_j^{[i]} \quad (3.61)$$

where $g_{b,k}^{[i]}$ for $k = 1, \dots, 6$ are integration constants, $V_j^{[i]}$ and $W_j^{[i]}$ are respectively the nodal forces and moments ensuring equilibrium at the nodes, $\mathcal{G}_b^V(\xi, y)$ and $\mathcal{G}_b^W(\xi, y)$ are given as:

$$\mathcal{G}_b^V(\xi, y) = \left(\lambda^2(\xi - y) + \frac{1}{6}(\xi - y)^3 + \frac{\lambda^3}{2} e^{-\frac{\xi-y}{\lambda}} - \frac{\lambda^3}{2} e^{\frac{\xi-y}{\lambda}} \right) \mathcal{H}(\xi - y) \quad (3.62)$$

$$\mathcal{G}_b^W(\xi, y) = \left(\lambda^2 + \frac{1}{2}(\xi - y)^2 - \frac{\lambda^2}{2} e^{-\frac{\xi-y}{\lambda}} - \frac{\lambda^2}{2} e^{\frac{\xi-y}{\lambda}} \right) \mathcal{H}(\xi - y) \quad (3.63)$$

\mathcal{G}_b^V and \mathcal{G}_b^W in Eqs. (3.62)-(3.63) are the particular integrals of the following differential equations for static equilibrium under a unit transverse force and a unit moment at $\xi = y$, as obtained by applying direct and inverse Laplace transform [69].

$$\mathcal{L}_b[\mathcal{G}_b^V(\xi, y)] + \delta(\xi - y) = 0 \quad (3.64)$$

$$\mathcal{L}_b[\mathcal{G}_b^W(\xi, y)] + \delta^{(1)}(\xi - y) = 0 \quad (3.65)$$

where symbol $\delta^{(1)}(\xi - y)$ denotes the formal first derivative of Dirac's delta at $\xi = y$; further the first six terms in Eq. (3.61) represent the solution of the homogeneous differential equation associated to Eq. (3.64) or Eq. (3.65). To define β_i in Eq. (3.61), the integration constants $g_{b,k}^{[i]}$, the nodal forces $V_j^{[i]}$ and nodal moments $W_j^{[i]}$ are computed by following set of algebraic equations respectively

$$\mathbf{\Omega}_b \mathbf{g}_b^{[i]} + \mathbf{G}_b^V \mathbf{v}^{[i]} + \mathbf{G}_b^W \mathbf{w}^{[i]} = \mathbf{v}_b^{[i]} \quad (3.66)$$

$$\mathbf{\Omega}_{b,1} \mathbf{g}_b^{[i]} + \mathbf{G}_{b,1}^V \mathbf{v}^{[i]} + \mathbf{G}_{b,1}^W \mathbf{w}^{[i]} = \boldsymbol{\theta}_b^{[i]} \quad (3.67)$$

and

$$\mathbf{\Omega}_{b\lambda} \mathbf{g}_b + \mathbf{G}_{b\lambda}^V \mathbf{v}^{[i]} + \mathbf{G}_{b\lambda}^W \mathbf{w}^{[i]} = \mathbf{0} \quad (3.68)$$

where $\mathbf{g}_b^{[i]} = [g_{b,1}^{[i]} \ g_{b,2}^{[i]} \ g_{b,3}^{[i]} \ g_{b,4}^{[i]} \ g_{b,5}^{[i]} \ g_{b,6}^{[i]}]^\top$, $\mathbf{v}^{[i]} = [V_2^{[i]} \ V_3^{[i]} \ \dots \ V_n^{[i]}]^\top$, $\mathbf{w}^{[i]} = [W_2^{[i]} \ W_3^{[i]} \ \dots \ W_n^{[i]}]^\top$; if the i^{th} shape function β_i corresponds to a unit deflection at node m such that $i = 2m - 1$, vector $\boldsymbol{\theta}_b^{[i]} = \mathbf{0}$ and $\mathbf{v}_b^{[i]}$ has zero components except for the m^{th} one, which is equal to 1; conversely, if the i^{th} shape function β_i corresponds to a unit rotation at node m such that $i = 2m$, vector $\mathbf{v}^{[i]} = \mathbf{0}$ and $\boldsymbol{\theta}_b^{[i]}$ has zero components except for the m^{th} one, which is equal to 1.

Matrices $\mathbf{\Omega}_b$, $\mathbf{\Omega}_{b\lambda}^V$ and $\mathbf{\Omega}_{b\lambda}^W$ in Eq. (3.66) through Eq. (3.68) are defined as

$$\mathbf{\Omega}_b = \begin{bmatrix} \boldsymbol{\omega}_b(0)^\top \\ \boldsymbol{\omega}_b(\xi_2)^\top \\ \vdots \\ \boldsymbol{\omega}_b(\xi_n)^\top \\ \boldsymbol{\omega}_b(1)^\top \end{bmatrix}; \quad \mathbf{\Omega}_{b,1} = \begin{bmatrix} \boldsymbol{\omega}_{b,1}(0)^\top \\ \boldsymbol{\omega}_{b,1}(\xi_2)^\top \\ \vdots \\ \boldsymbol{\omega}_{b,1}(\xi_n)^\top \\ \boldsymbol{\omega}_{b,1}(1)^\top \end{bmatrix}; \quad \mathbf{\Omega}_{b\lambda} = \begin{bmatrix} \boldsymbol{\omega}_{b,3}(0)^\top - \frac{1}{\lambda} \boldsymbol{\omega}_{b,2}(0)^\top \\ \boldsymbol{\omega}_{b,3}(1)^\top + \frac{1}{\lambda} \boldsymbol{\omega}_{b,2}(1)^\top \end{bmatrix}$$

(3.69)

being the functions $\omega_b, \omega_{b,1}, \omega_{b,2}, \omega_{b,3}$ in Eq. (3.69) defined as follows

$$\begin{aligned}\omega_b(\xi) &= \left[1 \quad \xi \quad \xi^2 \quad \xi^3 \quad \lambda^4 e^{\xi/\lambda} \quad \lambda^4 e^{-\xi/\lambda} \right]^T \\ \omega_{b,1}(\xi) &= \frac{d\omega_b(\xi)}{d\xi} = -\frac{1}{l} \left[0 \quad 1 \quad 2\xi \quad 3\xi^2 \quad \lambda^3 e^{\xi/\lambda} \quad -\lambda^3 e^{-\xi/\lambda} \right]^T \\ \omega_{b,2}(\xi) &= \frac{d^2\omega_b(\xi)}{d\xi^2} = \left[0 \quad 0 \quad 2 \quad 6\xi \quad \lambda^2 e^{\xi/\lambda} \quad \lambda^2 e^{-\xi/\lambda} \right]^T \\ \omega_{b,3}(\xi) &= \frac{d^3\omega_b(\xi)}{d\xi^3} = \left[0 \quad 0 \quad 0 \quad 6 \quad \lambda e^{\xi/\lambda} \quad -\lambda e^{-\xi/\lambda} \right]^T\end{aligned}\quad (3.70)$$

Matrices $\mathbf{G}_b^V, \mathbf{G}_b^W, \mathbf{G}_{b\lambda}^V$ and $\mathbf{G}_{b\lambda}^W$ in Eq. (3.66) through Eq. (3.68) are given as

$$\begin{aligned}(\mathbf{G}_b^V)_{ij} &= \mathcal{G}_b^V(\xi_i, \xi_j) & (\mathbf{G}_b^W)_{ij} &= \mathcal{G}_b^W(\xi_i, \xi_j) & i=1, \dots, n+1 \\ & & & & j=2, \dots, n \\ (\mathbf{G}_{b,1}^V)_{ij} &= -\frac{1}{l} \left. \frac{\partial \mathcal{G}_b^V(\xi, y)}{\partial \xi} \right|_{\substack{\xi=\xi_i \\ y=\xi_j}} & (\mathbf{G}_{b,1}^W)_{ij} &= -\frac{1}{l} \left. \frac{\partial \mathcal{G}_b^W(\xi, y)}{\partial \xi} \right|_{\substack{\xi=\xi_i \\ y=\xi_j}} \\ \mathbf{G}_{b\lambda}^V &= \begin{bmatrix} \gamma_{b,3}^V(0) - \frac{1}{\lambda} \gamma_{b,2}^V(0) \\ \gamma_{b,3}^V(1) + \frac{1}{\lambda} \gamma_{b,2}^V(1) \end{bmatrix} & \mathbf{G}_{b\lambda}^W &= \begin{bmatrix} \gamma_{b,3}^W(0) - \frac{1}{\lambda} \gamma_{b,2}^W(0) \\ \gamma_{b,3}^W(1) + \frac{1}{\lambda} \gamma_{b,2}^W(1) \end{bmatrix}\end{aligned}\quad (3.71)$$

being

$$\begin{aligned}\gamma_{b,1}^S(\xi) &= -\frac{1}{l} \left[\left. \frac{\partial \mathcal{G}_b^S(\xi, y)}{\partial \xi} \right|_{y=\xi_2} \quad \dots \quad \left. \frac{\partial \mathcal{G}_b^S(\xi, y)}{\partial \xi} \right|_{y=\xi_n} \right] \\ \gamma_b^S(\xi) &= \left[\left. \frac{\partial^2 \mathcal{G}_b^S(\xi, y)}{\partial \xi^2} \right|_{y=\xi_2} \quad \dots \quad \left. \frac{\partial^2 \mathcal{G}_b^S(\xi, y)}{\partial \xi^2} \right|_{y=\xi_n} \right] \\ \gamma_b^S(\xi) &= \left[\left. \frac{\partial^3 \mathcal{G}_b^S(\xi, y)}{\partial \xi^3} \right|_{y=\xi_2} \quad \dots \quad \left. \frac{\partial^3 \mathcal{G}_b^S(\xi, y)}{\partial \xi^3} \right|_{y=\xi_n} \right]\end{aligned}\quad (3.72)$$

with $S = V, W$. Combining Eq. (3.66) through Eq. (3.68) the following linear system is obtained

$$\begin{bmatrix} \mathbf{\Omega}_b & \mathbf{G}_b^V & \mathbf{G}_b^W \\ \mathbf{\Omega}_{b,1} & \mathbf{G}_{b,1}^V & \mathbf{G}_{b,1}^W \\ \mathbf{\Omega}_{b\lambda} & \mathbf{G}_{b\lambda}^V & \mathbf{G}_{b\lambda}^W \end{bmatrix} \begin{bmatrix} \mathbf{g}_b^{[i]} \\ \mathbf{v}^{[i]} \\ \mathbf{w}^{[i]} \end{bmatrix} = \begin{bmatrix} \mathbf{u}_v^{[i]} \\ \mathbf{u}_\theta^{[i]} \\ \mathbf{0} \end{bmatrix}\quad (3.73)$$

whose solutions $\mathbf{g}_b^{[i]}$, $\mathbf{v}^{[i]}$ and $\mathbf{w}^{[i]}$ fully define the shape function β_i in Eq. (3.61).

Using Eq. (3.51) and Eq. (3.61) to evaluate the entries $(\widehat{\mathbf{K}}_{e,a})_{ij}$, $(\widehat{\mathbf{M}}_{e,a})_{ij}$, $(\widehat{\mathbf{K}}_{e,b})_{ij}$, $(\widehat{\mathbf{M}}_{e,b})_{ij}$, the following equation can be written for the lattice member

$$(\mathbf{K}_e - \omega^2 \mathbf{M}_e) \mathbf{u}_e = \mathbf{f}_e \quad (3.74)$$

where

$$\mathbf{K}_e = \begin{bmatrix} \mathbf{K}_{e,a} & \mathbf{0} \\ \mathbf{0} & \mathbf{K}_{e,b} \end{bmatrix} \quad (3.75)$$

$$\mathbf{M}_e = \begin{bmatrix} \mathbf{M}_{e,a} & \mathbf{0} \\ \mathbf{0} & \mathbf{M}_{e,b} + \mathbf{M}_{e,\rho} \end{bmatrix} \quad (3.76)$$

being $\mathbf{K}_{e,a} = (EA/l^3) \widehat{\mathbf{K}}_{e,a}$, $\mathbf{K}_{e,b} = (EI/l^4) \widehat{\mathbf{K}}_{e,b}$, $\mathbf{M}_{e,a} = (\rho Al) \widehat{\mathbf{M}}_{e,a}$, $\mathbf{M}_{e,b} = (\rho Al) \widehat{\mathbf{M}}_{e,b}$, $\mathbf{M}_{e,\rho} = (\rho I/l) \widehat{\mathbf{M}}_{e,\rho}$. Matrix \mathbf{K}_e in Eq. (3.75) is the stiffness matrix and matrix \mathbf{M}_e in Eq. (3.76) is the mass matrix of the lattice member, as modelled according to the stress-driven nonlocal elasticity theory in conjunction with the Rayleigh beam theory. The size is $3(n+1) \times 3(n+1)$, being n the number of finite elements used to discretize the lattice member. In view of Eq. (3.46) through Eq. (3.50), \mathbf{M}_e is a consistent mass matrix, built based on the shape functions involved in the stiffness matrix.

The stiffness and mass matrices of the unit cell in the global reference system, \mathbf{K} and \mathbf{M} in Eq. (3.10), can be built by the performing standard finite-element assembling procedure making use of Eq. (3.75) and Eq. (3.76) for every lattice member. The band structure is computed by solving the corresponding eigenvalue problem (3.13). Since the eigenvalue problem is linear in the frequency for each given wave vector along the edges of the first Brillouin zone. Standard solvers for linear eigenvalue problems can be used in this case, as for instance the QZ eigensolver of Matlab [54].

Finally, it is noticed that the stress-driven differential equations derive from a constitutive integral equation where the strain at a given point depends on the stress at different points within a certain nonlocal neighbourhood [64]. Consequently, the stiffness matrix \mathbf{K}_e of the member accounts for nonlocal interactions among points which may fall within the same finite element or belong to different finite elements of the mesh. These nonlocal interactions are duly accounted for in proposed stiffness matrix \mathbf{K}_e , because \mathbf{K}_e is derived using the solutions of the stress-driven differential equations

Nonlocal interactions

(3.53)-(3.64)-(3.65) defined over the whole domain of the lattice member. Likewise, the dynamic-stiffness model, where the nonlocal constitutive interactions among points within the lattice member are necessarily taken into account being the dynamic-stiffness matrix built based on the exact solution of Eq. (3.14) through Eq. (3.17).

3.4 Numerical examples

To validate the dynamic-stiffness approach described in Section 3.2 and the finite-element approach introduced in Section 3.3, the wave dispersion analysis of stress-driven nonlocal beam of two lattices is carried out. In particular, considering the unit cell of the lattices, every lattice member is modelled exactly by a unique two-node element in the dynamic-stiffness approach; on the other hand the same lattices are modelled approximately by an increasingly refined mesh of two-node elements in the finite-element approach. Both the approaches are implemented in-house using Matlab [54]. The codes run on a HP Zbook 15v G5 Workstation (Intel i5-9300H 2.40GHz CPU with 8 GB of memory). The numerical validation has the further purpose to check the convergence of the finite-element results to the dynamic-stiffness ones and to assess how and to which extent the size effects affect the wave dispersion properties of the lattice, as modelled by the stress-driven nonlocal elasticity theory.

In agreement with existing studies in the literature [72], the following parameters are assumed for the lattice members: $E = 1.44$ GPa, $\rho = 1200$ kg/m³; the cross section is rectangular, $b = 20 \times 10^{-6}$ m is the width and $h = 20 \times 10^{-6}$ m is the thickness in the plane of the lattice, corresponding to $A = b \times h = 4 \times 10^{-10}$ m² and $I = bh^3/12 = 1.333 \times 10^{-20}$ m⁴ for area and moment of inertia. In the wave dispersion analysis, the frequencies are normalized to the first natural frequency of a hinged-hinged beam of length l that is characteristic of the lattice and is equal to $\pi^2 \sqrt{EI/(\rho AI^4)}$.

Consider the triangular lattice in Fig. 3.1a and the associated first Brillouin zone. Assume $l = 2 \times 10^{-4}$ m for the length of the lattice members and different internal lengths $L_c = \lambda l$, with $\lambda \in [0, 0.25]$.

For wave dispersion analysis, the nonlinear eigenvalue problem (3.12) associated with the dynamic-stiffness approach is solved by an in-house implementation of the contour-integral algorithm, selecting $K = 5$, $L = 10$ (with $\epsilon = 10^{-10}$) and $N_0 = 40$ as parameters of the algorithm described in Section 1.3.2.

Fig. 3.5 shows the first eight dispersion branches for three internal lengths $L_c = \lambda l$, with $\lambda = 0.10, 0.15, 0.20$, as obtained by the dynamic-stiffness approach and the finite-element approach, the latter with $n = 7$ for every lattice member within the cell. It is observed that the two approaches provide the same dispersion curves and that the finite-element results do not change appreciably increasing the number of finite elements, i.e., considering $n > 7$ for every lattice member. It is also noticed that no significant differences are encountered if the parameters of the contour-integral algorithm for the nonlinear eigenvalue problem (3.12) are changed for better accuracy.

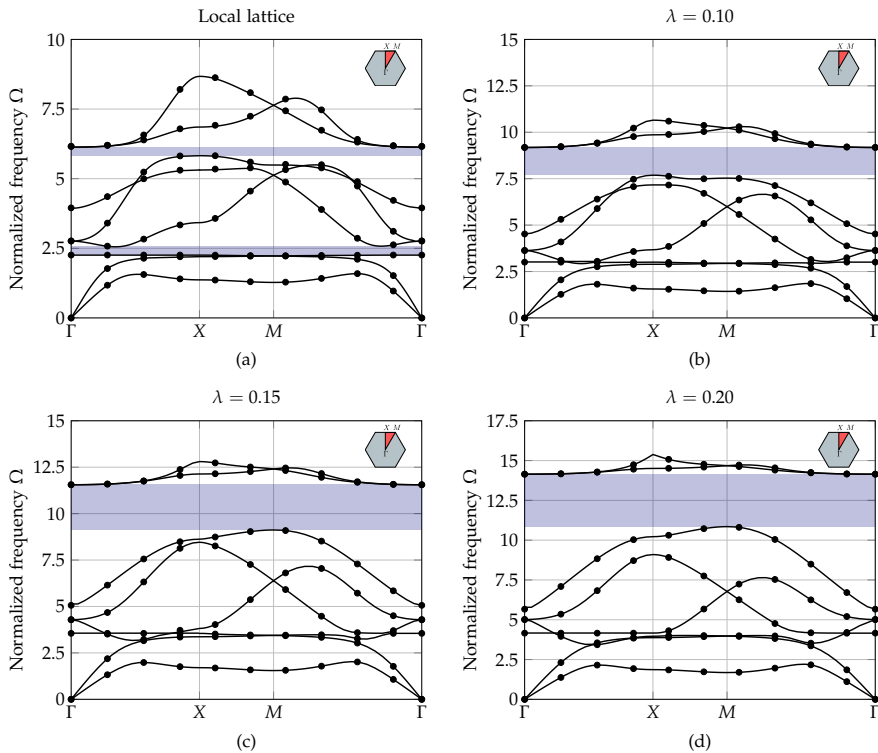


Figure 3.5: Dispersion curves along the irreducible Brillouin zone computed by the dynamic-stiffness approach (continuous line) and the finite-element approach (dots) with $n = 7$ finite elements, for various internal lengths $L_c = \lambda l$ and $l = 2 \times 10^{-4}$ m: (a) local lattice, (b) $\lambda = 0.10$, (c) $\lambda = 0.15$, (d) $\lambda = 0.20$.

In order to highlight the size effects predicted by the stress-driven nonlocal model, Fig. 3.5 includes for comparison the first eight dispersion branches for the Rayleigh local lattice. It is apparent that both the local lattice and the stress-driven nonlocal lattice exhibit band gaps, i.e. stop bands where the elastic waves do not propagate. However, while the local lattice exhibits two band gaps, the stress-driven nonlocal lattice features

one band gap, which is opened between the sixth and seventh branches. It shifts to higher frequencies and widens as the internal length increases. Notably, a band gap between the sixth and the seventh branches was found by Sepehri et al. [72] for a triangular lattice modelled by the modified couple stress theory.

For a further insight into the comparison between dynamic-stiffness and finite-element results, the first and second dispersion branches in Fig. 3.5 are now reported in Fig. 3.6, as calculated by the dynamic-stiffness approach and the finite-element approach with increasingly refined meshes. It is noticed that $n = 7$ finite elements provide satisfactory accuracy for all the considered dispersion branches; moreover, finite-element results for $n > 7$ coincide with those for $n = 7$ and are omitted for clarity.

Having discussed the convergence of the finite-element results to the dynamic-stiffness ones, now a few remarks are in order on the respective advantages of the two approaches. On one hand, the dynamic-stiffness approach is an exact approach, while the finite-element approach is an approximate approach, which attains the same accuracy of the dynamic-stiffness approach as the number of finite elements increases. That is, the size of the finite-element formulation is inevitably larger than the size of the dynamic-stiffness formulation. On the other hand, it is noteworthy that the eigenvalue problem (3.12) associated with the dynamic-stiffness approach is a nonlinear problem solved by an in-house implementation of the contour integral algorithm, while the eigenvalue problem (3.13) associated with the finite-element approach is linear and can be solved by standard and efficient eigensolvers available in most common numerical packages as, in this case, the QZ eigensolver of Matlab [54].

At this stage, it is interesting to compare the dispersion curves in Figure 3.5 with the corresponding ones obtained by using the stress-driven nonlocal model in conjunction with the Euler-Bernoulli theory, instead of the Rayleigh theory. The Rayleigh theory is used for beam lattices in several studies [21, 30, 31] as the rotational inertia of the beam cross section, which is not accounted for in the Euler-Bernoulli theory, may affect the dispersion properties of the lattice, especially at high frequencies. This concept is demonstrated in Figure 3.7, reporting the dispersion curves obtained by using the stress-driven nonlocal model in conjunction with the Rayleigh theory and the Euler-Bernoulli theory, for two internal lengths $L_c = \lambda l$, with $\lambda = 0.15, 0.20$. Indeed, it is seen that the dispersion curves based on the Euler-Bernoulli theory almost coincide with those based on the Rayleigh

theory at low frequencies, while they differ for increasing frequency. In both the dynamic-stiffness and finite-element approaches, the results for the Euler-Bernoulli theory are readily obtained by setting to zero the rotational inertia terms in Eq. (3.12) and Eq. (3.13) derived for the Rayleigh theory.

Next, the focus is on the size effects predicted by the stress-driven non-local model. Fig. 3.8 shows the dispersion curves of the stress-driven non-local lattice for various internal lengths $L_c = \lambda l$, with $\lambda \in [0, 0.25]$, as compared to the corresponding ones of the local lattice. It is apparent that the stress-driven model induces stiffening size effects as indeed, for a given wave vector, the elastic wave propagates at frequency larger than the corresponding frequency in the local model. In this respect, it is noteworthy that stiffening size effects occur also in alternative nonlocal models, see for instance the modified couple stress one [72] as the pertinent internal length scale parameter increases (see l_0 in Eq. (17-b) of ref. [72]). It is also apparent in Fig. 3.8 that the stiffening size effects become more pronounced as the internal length increases and are more evident in the high-frequency dispersion branches.

Further, to get a deeper insight into the size effects predicted by the stress-driven model, an interesting comparison can be made with the results obtained in ref. [72] for a triangular lattice modelled by the modified couple stress theory and, specifically, with the results showing the variation of the response for a reducing size of the lattice members at constant relative density of the lattice. The relative density, defined as ratio of the density of the lattice material to the density of the solid [29, 62], is given by $2\sqrt{3}(h/l)$ for a triangular lattice, being l the length of the lattice member and h its thickness in the plane of the lattice. Therefore, reducing the size of the lattice members at constant relative density of the lattice means that thickness h and length l of every lattice member are both reduced while the ratio h/l and, consequently, the relative density $2\sqrt{3}(h/l)$ are held constant. Figure 8 of ref. [72] shows that, for a given internal length scale parameter, the modified couple stress theory predicts a stiffening response for a reducing size of the lattice members at constant relative density of the lattice; indeed, the dispersion curves shift to higher frequencies as the size reduces and tend to the dispersion curves predicted by the classical Euler-Bernoulli local theory as the size increases. Remarkably, here Figures 3.9-3.10 demonstrate that, for given internal length L_c , the stress-driven model predicts stiffening effects as well, with dispersion curves shifting to higher

frequencies as the size reduces and tending to those predicted by the classical Rayleigh local theory as the size increases. Furthermore, it is seen that the Rayleigh local theory predicts the same dispersion curves regardless of the size of the lattice members, in agreement with the corresponding results pertaining to the classical Euler-Bernoulli local theory in Figure 8 of ref. [72]. Notice that Figures 3.9-3.10 are built varying the thickness of the lattice members in the plane of the lattice (and, consequently, the length l) at a constant relative density of the lattice equal to 0.346, which is the relative density considered for the results in Figure 3.5 through Figure 3.7; $h' = 0.7h$, $h' = h$, $h' = 1.3h$ are selected, with $h = 20 \times 10^{-6}$ m. It is noteworthy that stiffening size effects are well documented in the literature, see for instance the experimental results provided by Lam et al. [42] for cantilever beams subjected to a static tip load, for a reducing thickness and constant ratio h/l .

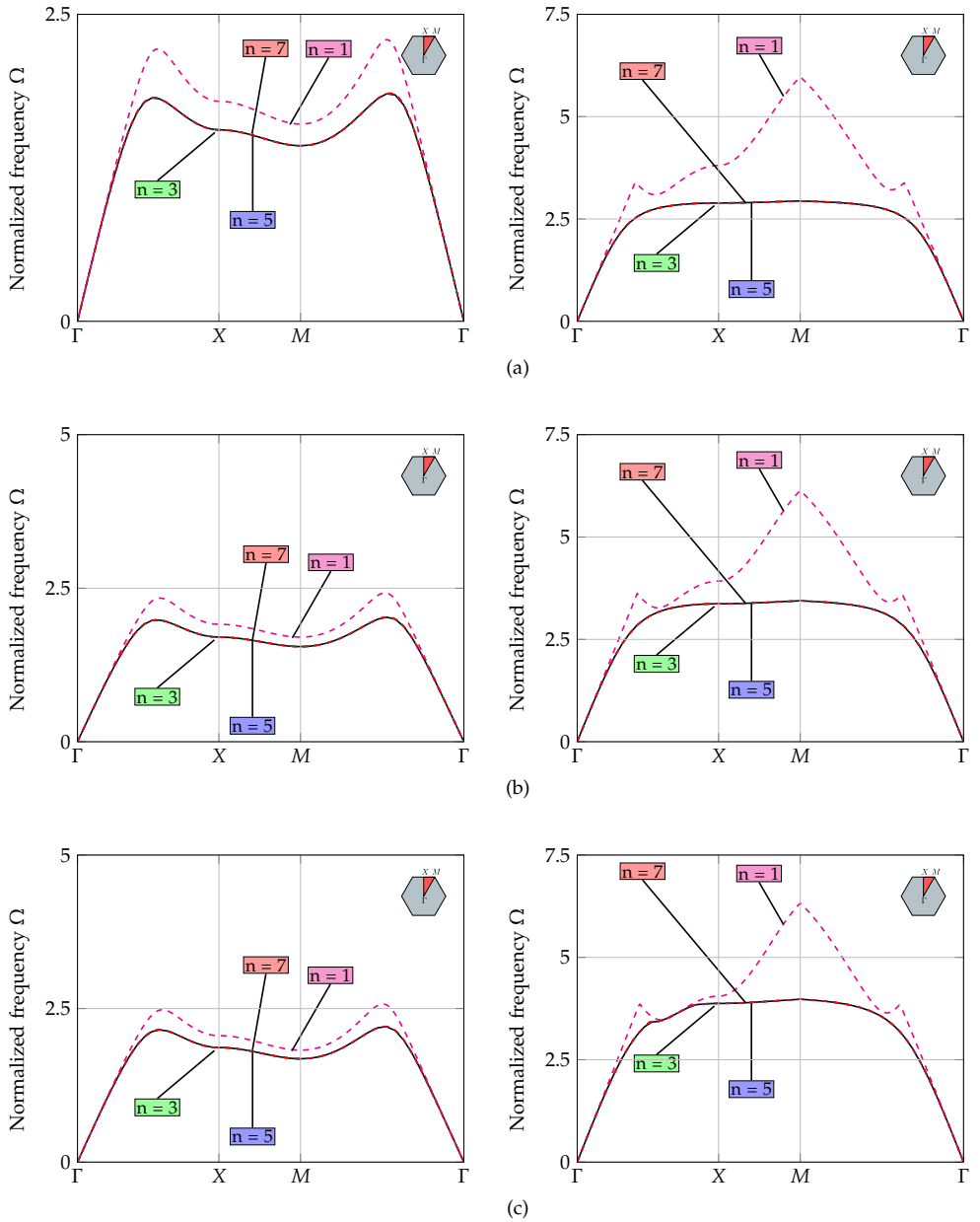
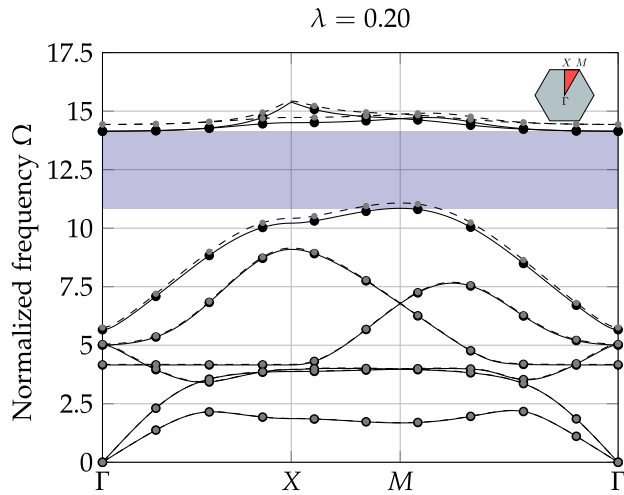
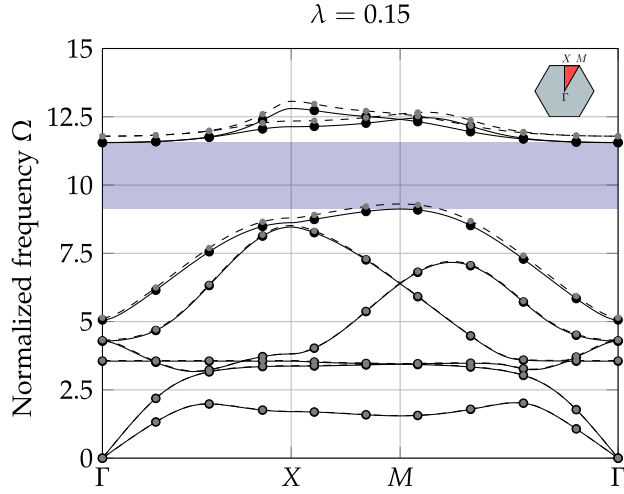


Figure 3.6: Dispersion curves along the irreducible Brillouin computed by the finite-element approach with increasing number n of finite elements, first branch (left column) and second branch (right column) for various internal lengths $L_c = \lambda l$ and $l = 2 \times 10^{-4}$ m: (a) $\lambda = 0.10$, (b) $\lambda = 0.15$, (c) $\lambda = 0.20$.

Figure 3.7: Dispersion curves along the irreducible Brillouin zone computed by the dynamic-stiffness approach (Rayleigh theory (continuous line), Euler-Bernoulli theory (dashed line)) and the finite-element approach (Rayleigh theory (black dots), Euler-Bernoulli theory (gray dots)) with $n = 7$ finite elements, for various internal lengths $L_c = \lambda l$ and $l = 2 \times 10^{-4}$ m: (a) $\lambda = 0.15$, (b) $\lambda = 0.20$.



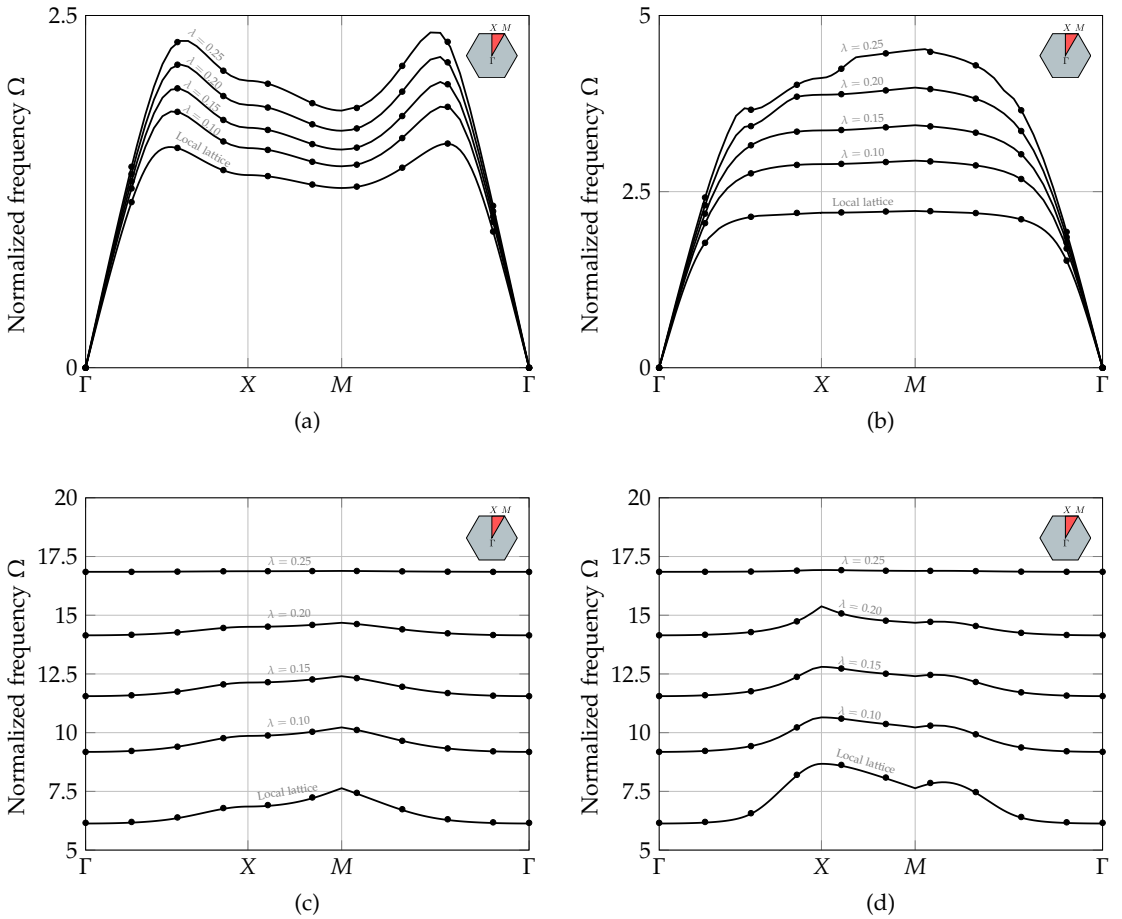


Figure 3.8: Dispersion curves along the irreducible Brillouin zone computed by the dynamic-stiffness approach (continuous line) and the finite-element approach (dots) with $n = 7$ finite elements, for various internal lengths $L_c = \lambda l$ and $l = 2 \times 10^{-4}$ m: (a) first branch, (b) second branch, (c) seventh branch, (d) eighth branch.

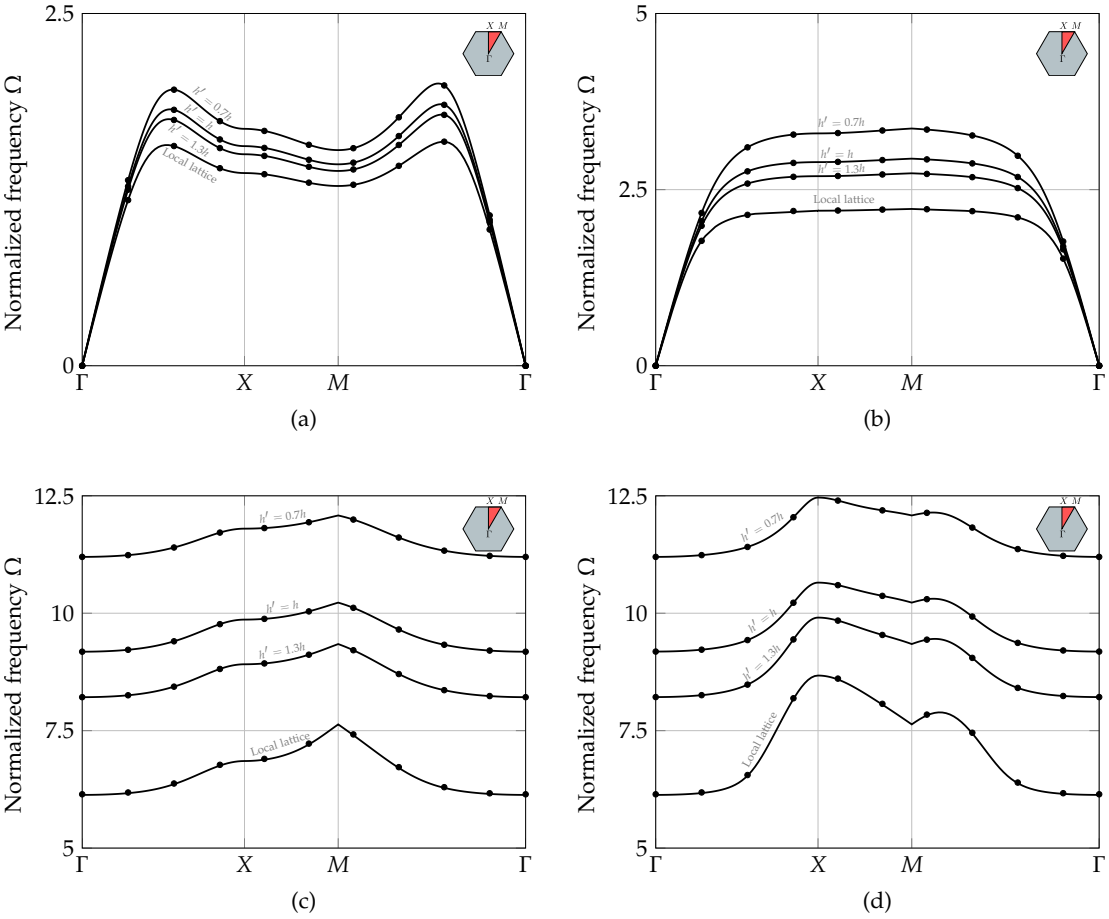


Figure 3.9: Dispersion curves along the irreducible Brillouin zone computed by the dynamic-stiffness approach (continuous line) and the finite-element approach (dots) with $n = 7$ finite elements, for the same internal length $L_c = 2 \times 10^{-5}$ m and various thicknesses h' , at constant relative density of the lattice = 0.346: (a) first branch, (b) second branch, (c) seventh branch, (d) eighth branch.

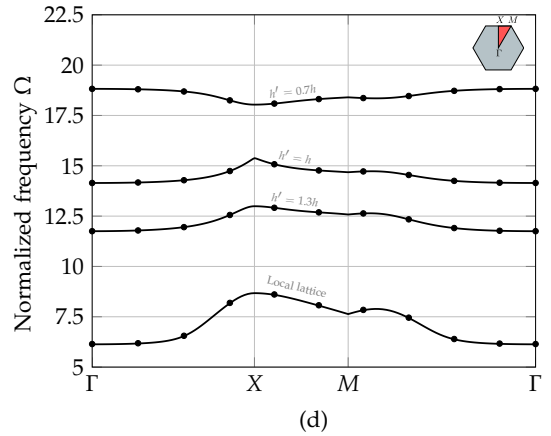
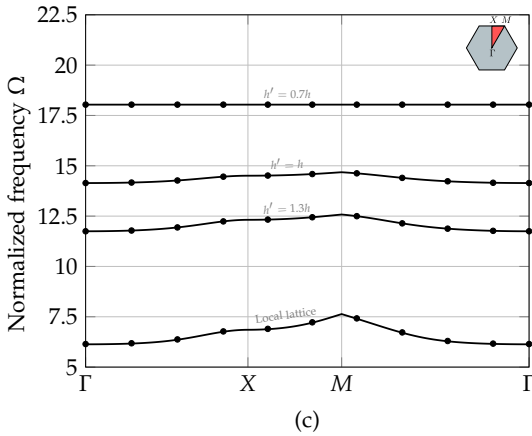
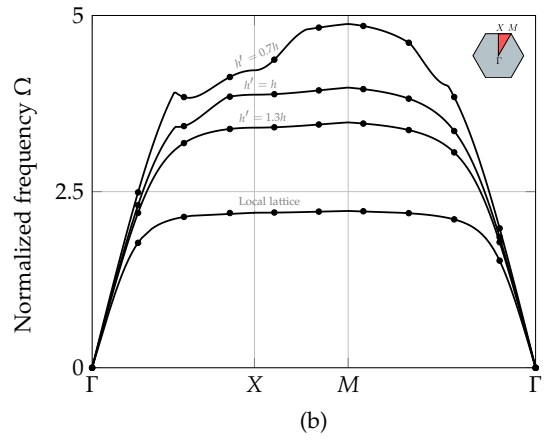
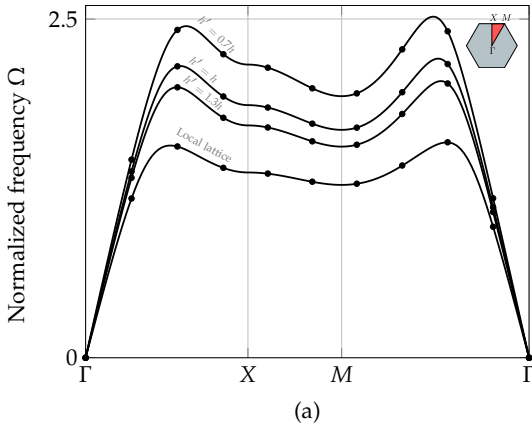


Figure 3.10: Dispersion curves along the irreducible Brillouin zone computed by the dynamic-stiffness approach (continuous line) and the finite-element approach (dots) with $n = 7$ finite elements, for the same internal length $L_c = 4 \times 10^{-5}$ m and various thicknesses h' , at constant relative density of the lattice = 0.346: (a) first branch, (b) second branch, (c) seventh branch, (d) eighth branch.

3.5 Conclusions

In this chapter, two ad-hoc computational approaches to analyse the wave propagation in small-size planar beam lattices, modelled with the stress-driven nonlocal elasticity theory, have been developed: 1) the exact dynamic-stiffness approach relies on the closed form solutions of the governing equation of the single lattice member, consequently each lattice member is modelled by a unique two-node beam element, whose nodal displacements and forces are exactly related by the exact dynamic-stiffness matrix, as a consequence no further discretization is needed; 2) the finite-element approach hinges on the discretization of the single beam member into a mesh of two-node beam elements. The stiffness and mass matrices of each element are derived from the principle of virtual work, making use of appropriate shape functions based on the exact solution of the governing equations for static equilibrium.

For the first time, the stress-driven nonlocal elasticity theory has been employed to investigate the dispersion properties of small-size planar beam lattices. It has been found that the dispersion curves of the stress-driven nonlocal beam lattice exhibit significant stiffening size effects, in complete agreement with previous studies based on the modified couple stress theory. The result here calculated by the proposed computational framework may be relevant for designing small-size planar beam lattices for applications in NEMS/MEMS. Specifically, it is relevant to assess whether waves produced by external shocks propagates or they may be filtered out by band gaps within certain frequency ranges, as the band gaps found in the numerical examples.

SUMMARY AND CONCLUSIONS

This thesis addressed the formulation and development of novel analytically-based computational frameworks for investigating the dynamics and wave propagation properties of an emerging class of structures, namely metamaterial structures. The development of these computational frameworks is motivated by the increasing number of studies that address metamaterial structures, in which standard numerical techniques based on the finite element method are employed to investigate their dynamics and dispersion properties; indeed, the proposed computational frameworks are conceived to serve as benchmarks for the finite element results.

Throughout the chapters of this thesis several novelties have introduced. In particular, a new reduced-order dynamic-stiffness model of locally-resonant metamaterial beams has been derived building the exact dynamic-stiffness matrix based on closed-form solutions of the governing equations obtained by means of exact dynamic condensation of the degrees of freedom within the resonators, modelled as multi-degrees-of-freedom mass-spring-dashpot, and making use of the theory of the generalized functions. The dynamic-stiffness matrix serves as basis to exactly calculate the dynamic response for forced and free vibrations in the frequency domain. To calculate the complex eigenvalues and modes, an accurate and efficient contour-integral method has been employed here for this purpose for the first time. Deriving suitable orthogonality conditions for the complex modes of the metamaterial beams, the modal response for arbitrary loads in time and frequency domains has been obtained.

Furthermore, a novel reduced-order dynamic stiffness model has been formulated for investigating the dynamics of locally-resonant metamaterial plates, that is assemblies of plates coupled by periodic arrays of resonators. The derivation of the dynamic-stiffness matrix for these assemblies hinges on the exact dynamic-condensation of the coupling arrays of resonators

leading to a reduced-order dynamic stiffness model obtained by the application of the spectral dynamic stiffness method. The dynamic-stiffness matrix allows to compute the natural frequencies and undamped modes by extending the Wittrick-Williams algorithm in such a way to make it applicable to the reduced-order model. The natural frequencies and the undamped modes together with appropriate orthogonality conditions derived for the reduced-order model are the basis to compute the modal response for arbitrary loads in time and frequency domain.

Moreover, the wave propagation in small-size metamaterial structures is addressed employing the exact dynamic-stiffness method to compute the dispersion proprieties of planar microlattices. Considering the unit cells as ensembles of stress-drive nonlocal Rayleigh beams, the dispersion curves are calculated by solving the exact nonlinear eigenproblem arising from the application of the Bloch's theorem to the governing equations of the unit cell in the frequency domain. Furthermore, an ad-hoc computationally efficient finite-element procedure has been developed by deriving suitable shape functions from closed-form solutions of the governing equation for static equilibrium.

The developments addressed in this thesis contributed to extend the previous literature, since so far no study has directly addressed, within the framework of the dynamic-stiffness method, the dynamics of locally-resonant metamaterial structures.

The availability of the novel analytically-based computational methods developed in this thesis may have a significant impact on the modelling of metamaterial structures, due to the lack of efficient and exact reduced-order models in the literature. In particular, the availability of closed-form solutions significantly reduces the computational cost to the the free-vibration response analysis, which has to be performed just once. Furthermore, the proposed methods can also serve as benchmarks for the standard numerical techniques usually employed.

LIST OF SYMBOLS - CHAPTER 1



α_i	coefficients in solution of homogeneous differential equation
A	coefficient matrix in equations of boundary conditions for displacements
A	cross-section area
a	mutual distance between consecutive resonators
B	coefficient matrix in equations of boundary conditions for forces
B, C, D, F	coefficients in particular integral for deflection
χ_n	load-dependent coefficient defined in modal response, n^{th} mode
C_r	damping matrix of the resonator
c	vector of integration constants
c_1, c_2	resonator damping coefficients
Δ_1	2-DOF resonator-depending coefficient in modal response
δ	Dirac's delta function
D	dynamic stiffness matrix of the beam
$\mathbf{D}^{[uu]}, \mathbf{D}^{[uk]}, \mathbf{D}^{[ku]}, \mathbf{D}^{[kk]}$	submatrices of matrix D
D_r	dynamic stiffness matrix of the resonator
$D_r^{[vv]}, \mathbf{d}_r^{[vu]}, \mathbf{d}_r^{[uv]}, \mathbf{D}_r^{[uu]}$	submatrices of matrix D_r
ϵ	tolerance in contour-integral algorithm
E	elastic modulus
Φ_J, Φ_Ω	matrices of frequency response terms associated with resonator reaction forces and solution of homogeneous differential equation, respectively
ϕ, Φ	cross-section rotation in time and frequency domains, respectively

γ_n	space-dependent function in modal impulse response function, n^{th} mode
γ_0	center of integration circle in contour-integral algorithm
γ_1, γ_2	coefficients in modal response for 2DOF resonators
Γ	circle in contour-integral algorithm
$\Gamma_1, \Gamma_2, \Gamma_3$	coefficients in modal response for 2DOF resonators
$\hat{\mathbf{g}}_n$	n^{th} coefficient of modal coordinate
G	shear modulus
g_n	n^{th} modal coordinate
\mathbf{f}	vector of nodal forces of the beam
\mathcal{H}	Heaviside function
\mathbf{H}	vector of frequency response functions
\mathbf{H}_n	modal frequency response function vector, n^{th} mode
$\hat{\mathbf{H}}_{KL_0}, \hat{\mathbf{H}}_{KL_0}^{\leq}$	Hankel matrices in contour-integral algorithm
\mathbf{h}	vector of impulse response functions
\mathbf{h}_n	vector of modal impulse response functions, n^{th} mode
H_n	complex function in modal frequency response, n^{th} mode
\mathbf{I}	identity matrix
I	cross-section moment of inertia
\mathbf{J}	vector of particular integrals of equations of motion associated with Dirac's deltas
J_V, J_Φ, J_M, J_S	particular integral of uncoupled differential equation associated with Dirac's delta and its derivatives
J_Z	particular integral of uncoupled differential equation associated with Dirac's delta and its derivatives, $J_Z = J_V$ for deflection and $J_Z = J_\Phi$ for rotation
κ_{eq}	resonator frequency-dependent stiffness
\mathbf{K}_r	stiffness matrix of the resonator
K	maximum moment degree in contour-integral algorithm
k_1, k_2	resonator stiffness coefficients
\mathcal{L}	stiffness operator
L	beam length
L_0	number of source vectors collected in \mathbf{U} and \mathbf{V} in contour-integral algorithm

$\mathbf{\Lambda}$	vector of unknown resonator reaction forces
λ_i	roots of characteristic polynomial from homogeneous differential equation
\mathcal{M}	mass operator
μ_n	resonator-depending coefficient in modal response, n^{th} mode
\mathbf{M}_k	shifted and scaled moments in contour-integral algorithm
\mathbf{M}_r	mass matrix of the resonator
m, M	bending moment in time and frequency domains, respectively
m_1, m_2	resonator masses
\tilde{m}	number of singular value components retained in contour-integral algorithm
\mathcal{N}	number of finite elements along the beam
N_0	number of points for trapezoidal rule integration in contour-integral algorithm
N_r	number of resonators
n_0	size of dynamic stiffness matrix \mathbf{D}
n_r	number of degrees of freedom within every resonator
\mathcal{O}	frequency-dependent terms in orthogonality conditions
$\mathbf{\Omega}$	matrix associated with solution of homogeneous differential equation
ω	frequency
ω_n	complex eigenvalue, n^{th} mode
ω_{Dn}	pseudo-undamped frequency, n^{th} mode
Π_n	inertia and resonator-depending coefficient in modal response, n^{th} mode
ψ_n	vector in modal impulse response function, n^{th} mode
\mathbf{p}	vector of dynamic loads
p_1, p_2	coefficients in uncoupled differential equation
p_3	function depending on load and resonator reaction in uncoupled differential equation
p_v, p_ϕ	transversal and rotational dynamic loads
q	resonator-reaction depending coefficient

\mathcal{R}	operator associated with the reactions of the resonators
ρ	volumetric mass density
ρ_0	radius of integration circle in contour-integral algorithm
\mathbf{R}	matrix of particular integrals of equation of motion associated with Dirac's delta
r_h, R_h	h^{th} resonator reaction force in time and frequency domains, respectively
$\Sigma_1, \Sigma_2, \Sigma_3$	coefficients in particular integral for deflection
σ_i	i^{th} singular value component
$\mathcal{S}_1, \mathcal{S}_2$	coefficients in particular integral for rotation
s, S	shear-force in time and frequency domains, respectively
θ	angle parameter in contour-integral algorithm
\mathbf{U}	complex random source matrix in contour-integral algorithm
$\mathbf{U}_{h,n}$	eigenvector of the h^{th} resonators, n^{th} mode
$\mathbf{u}_h, \mathbf{U}_h$	vector of displacements within h^{th} resonator in time and frequency domains, respectively
\mathbf{u}	vector of nodal displacements of the beam
$\mathbf{u}^{[k]}, \mathbf{u}^{[u]}$	subvectors of vector \mathbf{u}
\mathbf{V}	complex random source matrix in contour-integral algorithm
\mathbf{v}	vector of deflections and rotations.
v, V	deflection in time and frequency domains, respectively
V_g	ground displacement for calculation of transmittance
\mathbf{W}	matrix depending on solution of homogeneous differential equation
w_n	time-dependent function in modal impulse response function, n^{th} mode
$\tilde{\zeta}_n$	modal damping ratio, n^{th} mode
x_h	application point of h^{th} resonator
Y_1, Y_2	constants
v_n	vector in modal impulse response function, n^{th} mode

\mathbf{y}, \mathbf{Y}	vector of beam displacements in time and frequency domains, respectively
\mathbf{Y}_n	vector of eigenfunctions of the response variable, n^{th} mode
ζ_j	j^{th} complex eigenvalue of linear pencil
Z	symbol for deflection ($Z = V$) or rotation ($Z = \Phi$)
Z_{om}	solution of homogeneous differential equation, $Z_{om} = V_{om}$ for deflection or $Z_{om} = \Phi_{om}$ for rotation

B

LIST OF SYMBOLS - CHAPTER 2

a	semibase of a plate strip
b	semiheight of a plate strip
χ_n	load-dependent coefficient defined in modal response, n^{th} mode
δ	Dirac's delta function
D_k	flexural stiffness of the k^{th} plate
$d_i^{(k,j)}$	i^{th} generalized displacements of the j^{th} strip on the k^{th} plate
$\mathbf{d}_i^{(k,j)}$	vector collecting the coefficients of the modified Fourier series representation of the i^{th} generalized displacements of the j^{th} strip on the k^{th} plate
$\mathbf{D}^{(k,j)}$	dynamic stiffness matrix of the j^{th} strip on the k^{th} plate
$\tilde{\mathbf{D}}$	reduced-order global dynamic stiffness matrix
E_k	Young modulus of the k^{th} plate
\mathbf{F}'_e	vector of the forces exerted by the plates on the resonators aligned along the vertical line at $\mathbf{x} = \mathbf{x}_h$
\mathbf{F}_e	vector of the forces exerted by the resonators aligned along the vertical line at $\mathbf{x} = \mathbf{x}_h$ on the plates
$\mathbf{F}_e^{(k,g)'}$	force exerted by the k^{th} and g^{th} plates on the resonator
$\mathbf{F}_e^{(k,g)}$	force exerted by the resonator on the k^{th} and g^{th} plates
$\mathbf{f}_i^{(k,j)}$	vector collecting the coefficients of the modified Fourier series representation of the i^{th} generalized forces of the j^{th} strip on the k^{th} plate
$f_s^{k,j}$	s^{th} generalized forces of the j^{th} strip on the k^{th} plate
f	time-dependent load function

\hat{f}	frequency-dependent load function
h_k	thickness of the k^{th} plate
J	number of natural frequencies below a given trial frequency
J_0	numbers of “clamped-clamped” natural frequencies of the bare strips
J_{0r}	numbers of “clamped-clamped” natural frequencies of the resonators
$\mathcal{K}_{11}, \mathcal{K}_{12}, \mathcal{K}_{21}, \mathcal{K}_{22}$	spectral dynamic stiffness matrix of the resonators coupling two consecutive plates
κ_{eq}	condensed dynamic stiffness matrix of the resonators aligned along a vertical line $\mathbf{x} = \mathbf{x}_h$
$\kappa_{eq}^{(k,g)}$	condensed dynamic stiffness matrix of the resonator coupling the k^{th} and g^{th} plate
$\tilde{\kappa}_{eq}$	diagonal block matrix collecting all the condensed dynamic stiffness matrices of the resonators coupling the plates along a vertical line
$\mathbf{K}_{ee}^{k,g}, \mathbf{K}_{em}^{k,g}, \mathbf{K}_{me}^{k,g}, \mathbf{K}_{mm}^{k,g}$	submatrices of the dynamic stiffness matrix of the resonator coupling the k^{th} and g^{th} plate
\mathcal{L}	stiffness operator
L	semilength of a strip edge (either $L = a$ or $L = b$)
\mathcal{M}	mass operator
μ_n	resonator-depending vector in modal response, n^{th} mode
ν_k	Poisson coefficient of the k^{th} plate
N_r	number of resonators connecting two consecutive plates
N_i	number of DOFs within each resonator
n_e	number of resonators along each connected edge of two consecutive plates
n_p	number of plates
ω	frequency
ω_{hi}	i^{th} natural frequency of the h^{th} resonator
ω_n	n^{th} natural frequency of the locally-resonant meta-material plate assembly
Π_n	inertia and resonator-depending coefficient in modal response, n^{th} mode
\mathbf{P}	permutation matrix

\mathcal{R}	operator associated with the reactions of the resonators
ρ_k	volume mass density of the k^{th} plate
$\mathbf{r}_h, \mathbf{R}_h$	h^{th} resonator reaction force in time and frequency domains, respectively
\mathcal{T}_l	modified Fourier basis function
\mathbf{U}_e	vector of the deflections of all the plates at the attachment points of the resonators aligned along the vertical line $\mathbf{x} = \mathbf{x}_h$
$\mathbf{U}_e^{(k,g)}$	vector collecting the deflections of the k^{th} and g^{th} plates at the attachment points of the resonator at $\mathbf{x} = \mathbf{x}_h$
$\mathbf{U}_m^{(k,g)}$	vector of the DOFs of the masses within the resonator coupling the k^{th} and g^{th} plates at $\mathbf{x} = \mathbf{x}_h$
\mathbf{v}	constant vector
\mathbf{w}, \mathbf{W}	vector collecting the deflections in all the plates in time and frequency domains, respectively
\mathbf{W}_n	vector of the deflection eigenfunctions in all the plates, n^{th} mode
$W^{(k)}$	deflection of the k^{th} plate
$W^{(k,j)}, \Phi_x^{(k,j)}, M_x^{(k,j)}, V_x^{(k,j)}$	deflection, rotation, bending moment and Kirchhoff shear force per unit of length along the four edge of the j^{th} strip on the k^{th} plate
ζ	coordinate along an edge of the plate strip
\mathbf{x}_h	application point of the h^{th} resonator
\mathbf{Y}_n	vector of eigenfunctions of the response variable, n^{th} mode
ζ_{ls}	coefficient of the modified Fourier basis function

LIST OF SYMBOLS - CHAPTER 3



\mathbf{A}_e	coefficient matrix in equations of boundary conditions for end node displacements
A	cross-section area
β_i	i^{th} flexural shape function
\mathbf{B}_e	coefficient matrix in equations of boundary conditions for end node forces
b	cross-section base
χ	curvature
\mathbf{c}	vector of integration constants
$\mathbf{c}_a, \mathbf{c}_b$	subvectors of \mathbf{c}
$c_{a,k}, c_{b,k}$	k^{th} integration constant for axial and flexural response, respectively
δ_1, δ_2	real part of the wave vector components
\mathbf{D}	exact dynamic-stiffness matrix of the unit cell
\mathbf{D}_e	exact dynamic-stiffness matrix a two-node member
$\mathbf{D}_{e,a}, \mathbf{D}_{e,b}$	submatrices of exact dynamic-stiffness matrix a two-node member associated with the axial and flexural degrees of freedom, respectively
$\tilde{\mathbf{D}}$	Bloch-transformed exact dynamic-stiffness matrix of the unit cell
\mathbf{d}_e	vector of end nodal displacements of a two-node member
η	axial strain
ϵ_1, ϵ_2	imaginary part of the wave vector components
$\mathbf{e}_1, \mathbf{e}_2$	basis vectors of the direct lattice
$\mathbf{e}_1^*, \mathbf{e}_2^*$	basis vectors of the reciprocal lattice
E	Young modulus
\mathbf{f}_e	nodal force vector of a two-node member divided into several two-node beam elements

$\mathbf{f}_{e,a}, \mathbf{f}_{e,b}$	subvectors of vector \mathbf{f}_e collecting axial and flexural nodal forces, respectively
$\widehat{\mathbf{f}}_{e,a}, \widehat{\mathbf{f}}_{e,b}$	scaled vectors of $\mathbf{f}_{e,a}, \mathbf{f}_{e,b}$, respectively
$\mathcal{G}_a, \mathcal{G}_b$	fundamental solution of the static equilibrium equation under unitary concentrated axial and flexural force
g_k, f_k	k^{th} term of the exact solution of the axial and flexural response, respectively
$g_{a,k}^{[i]}, g_{b,k}^{[i]}$	k^{th} integration constant for axial and flexural i^{th} shape function, respectively
$\mathbf{g}_a^{[i]}, \mathbf{g}_b^{[i]}$	vector of integration constants for axial and flexural i^{th} shape function, respectively
$\mathbf{h}^{[i]}$	vector of nodal axial forces ensuring equilibrium at the nodes for the i^{th} shape function
h	cross-section height
\mathcal{I}	identity operator
\mathbf{i}, \mathbf{j}	basis vectors of the coordinate system
I	cross-section moment of inertia
\mathbf{K}	stiffness matrix of the unit cell
\mathbf{K}_e	stiffness matrix of a two-node member divided into several two-node beam elements
$\mathbf{K}_{e,a}, \mathbf{K}_{e,b}$	submatrices of matrix \mathbf{K}_e associated with axial and flexural degrees of freedom
$\widehat{\mathbf{K}}_{e,a}, \widehat{\mathbf{K}}_{e,b}$	scaled matrices of $\mathbf{K}_{e,a}$ and $\mathbf{K}_{e,b}$, respectively
$\widetilde{\mathbf{K}}$	Bloch-transformed stiffness matrix of the unit cell
$\widetilde{\mathbf{k}}$	wave vector
k_1, k_2	wave vector components
\mathcal{L}_a	axial stiffness operator
\mathcal{L}_b	flexural stiffness operator
λ	dimensionless internal length
L	beam length
L_c	internal length
l	length of the member
\mathbf{M}	mass matrix of the unit cell
\mathbf{M}_e	stiffness matrix of a two-node member divided into several two-node beam elements

$\mathbf{M}_{e,a}, \mathbf{M}_{e,b}, \mathbf{M}_{e,\rho}$	submatrices of matrix \mathbf{M}_e associated with axial and flexural degrees of freedom, and rotary inertia respectively
$\widehat{\mathbf{M}}_{e,a}, \widehat{\mathbf{M}}_{e,b}, \widehat{\mathbf{M}}_{e,\rho}$	scaled matrices of $\mathbf{M}_{e,a}$, $\mathbf{M}_{e,b}$ and $\mathbf{M}_{e,\rho}$, respectively
$\widetilde{\mathbf{M}}$	Bloch-transformed mass matrix of the unit cell
M	bending moment
M_n	number of member-to-member nodes
N	axial force
n	number of two-node beam elements into which a member is divided
$\Omega_a, \Omega_{a\lambda}$	coefficient matrices in equations enforcing the boundary conditions satisfied by the axial shape functions
$\Omega_b, \Omega_{b\lambda}^V, \Omega_{b\lambda}^W$	coefficient matrices in equations enforcing the boundary conditions satisfied by the flexural shape functions
$\omega_a, \omega_{a,1}, \omega_{a,2}$	vector collecting the terms of the homogeneous axial static equilibrium solution and their derivatives
$\omega_b, \omega_{b,1}, \omega_{b,2}, \omega_{b,3}$	vector collecting the terms of the homogeneous flexural static equilibrium solution and their derivatives
ω	frequency
$\omega_a, \omega_b, \omega_\rho$	frequency parameters
$\Psi_{e,a}, \Psi_{e,b}$	diagonal matrices collecting axial and flexural shape functions, respectively
ψ_i	i^{th} axial shape function
\mathbf{p}_e	vector of end nodal forces of a two-node member
\mathbf{q}	vector of nodal displacements
$\mathbf{q}_l, \mathbf{q}_b, \mathbf{q}_{lb}, \mathbf{q}_i$	subvectors of \mathbf{q} corresponding to displacements of the the left, bottom, left-bottom, internal nodes of the unit cell, respectively
$\widetilde{\mathbf{q}}$	vector of Bloch reduced coordinates
ρ	volumetric mass density
θ	cross-section rotation
\mathbf{T}	transformation matrix
T	shear force
\mathbf{u}_e	nodal displacement vector of a two-node member divided into several two-node beam elements

$\mathbf{u}_{e,a}, \mathbf{u}_{e,b}$	subvectors of vector \mathbf{u}_e collecting axial and flexural nodal displacements, respectively
$\mathbf{u}_a^{[i]}$	vector with all components equal to zero except for the i^{th} one
u	axial displacement
$\mathbf{v}^{[i]}$	vector of nodal forces ensuring equilibrium at the nodes for the i^{th} shape function
v	deflection
$\mathbf{w}^{[i]}$	vector of nodal bending moments ensuring equilibrium at the nodes for the i^{th} shape function
ξ	dimensionless spatial coordinate
x	spatial coordinate

BIBLIOGRAPHY

- [1] J. Asakura, T. Sakurai, H. Tadano, T. Ikegami, and K. Kimura. A numerical method for nonlinear eigenvalue problems using contour integrals. *JSIAM Letters*, 1:52–55, 2009.
- [2] M. Badreddine Assouar and M. Oudich. Enlargement of a locally resonant sonic band gap by using double-sides stubbed phononic plates. *Applied Physics Letters*, 100(12):123506, 2012.
- [3] J. Banerjee. Dynamic stiffness formulation for structural elements: A general approach. *Computers & Structures*, 63(1):101–103, 1997.
- [4] J. Banerjee. Free vibration of axially loaded composite Timoshenko beams using the dynamic stiffness matrix method. *Computers & Structures*, 69(2):197–208, 1998.
- [5] J. Banerjee. Free vibration of centrifugally stiffened uniform and tapered beams using the dynamic stiffness method. *Journal of Sound and Vibration*, 233(5):857–875, 2000.
- [6] J. Banerjee. Dynamic stiffness formulation and free vibration analysis of centrifugally stiffened Timoshenko beams. *Journal of Sound and Vibration*, 247(1):97–115, 2001.
- [7] J. Banerjee. Free vibration analysis of a twisted beam using the dynamic stiffness method. *International Journal of Solids and Structures*, 38(38-39):6703–6722, 2001.
- [8] J. Banerjee. Frequency equation and mode shape formulae for composite Timoshenko beams. *Composite Structures*, 51(4):381–388, 2001.
- [9] J. Banerjee. Free vibration of sandwich beams using the dynamic stiffness method. *Computers & structures*, 81(18-19):1915–1922, 2003.

- [10] J. Banerjee. Development of an exact dynamic stiffness matrix for free vibration analysis of a twisted Timoshenko beam. *Journal of Sound and Vibration*, 270(1-2):379–401, 2004.
- [11] J. Banerjee. Free vibration of beams carrying spring-mass systems- a dynamic stiffness approach. *Computers & structures*, 104:21–26, 2012.
- [12] J. Banerjee, C. Cheung, R. Morishima, M. Perera, and J. Njuguna. Free vibration of a three-layered sandwich beam using the dynamic stiffness method and experiment. *International Journal of Solids and Structures*, 44(22-23):7543–7563, 2007.
- [13] J. Banerjee and D. Kennedy. Dynamic stiffness method for inplane free vibration of rotating beams including Coriolis effects. *Journal of Sound and Vibration*, 333(26):7299–7312, 2014.
- [14] J. Banerjee and A. Sobey. Dynamic stiffness formulation and free vibration analysis of a three-layered sandwich beam. *International Journal of Solids and Structures*, 42(8):2181–2197, 2005.
- [15] J. Banerjee and F. Williams. Exact Bernoulli-Euler dynamic stiffness matrix for a range of tapered beams. *International journal for numerical methods in engineering*, 21(12):2289–2302, 1985.
- [16] J. Banerjee and F. Williams. Exact Bernoulli-Euler static stiffness matrix for a range of tapered beam-columns. *International Journal for Numerical Methods in Engineering*, 23(9):1615–1628, 1986.
- [17] J. Banerjee and F. Williams. Exact dynamic stiffness matrix for composite Timoshenko beams with applications. *Journal of Sound and Vibration*, 194(4):573–585, 1996.
- [18] J. R. Banerjee. Dynamic stiffness formulation and its application for a combined beam and a two degree-of-freedom system. *Journal of Vibration and Acoustics*, 125(3):351–358, 06 2003.
- [19] J. R. Banerjee. Review of the dynamic stiffness method for free-vibration analysis of beams. *transp saf environ*, 1(2):106–116, Nov. 2019.
- [20] R. Barretta, S. A. Faghidian, and R. Luciano. Longitudinal vibrations of nano-rods by stress-driven integral elasticity. *Mechanics of Advanced Materials and Structures*, 26(15):1307–1315, 2019.

- [21] G. Bordiga, L. Cabras, D. Bigoni, and A. Piccolroaz. Free and forced wave propagation in a Rayleigh-beam grid: Flat bands, dirac cones, and vibration localization vs isotropization. *International Journal of Solids and Structures*, 161:64–81, 2019.
- [22] T. Bückmann, M. Thiel, M. Kadic, R. Schittny, and M. Wegener. An elasto-mechanical unfeelability cloak made of pentamode metamaterials. *Nature communications*, 5(1):1–6, 2014.
- [23] A. Casalotti, S. El-Borgi, and W. Lacarbonara. Metamaterial beam with embedded nonlinear vibration absorbers. *International Journal of Non-Linear Mechanics*, 98:32–42, 2018.
- [24] J.-S. Chen, B. Sharma, and C. Sun. Dynamic behaviour of sandwich structure containing spring-mass resonators. *Composite Structures*, 93(8):2120–2125, 2011.
- [25] C. C. Claeys, K. Vergote, P. Sas, and W. Desmet. On the potential of tuned resonators to obtain low-frequency vibrational stop bands in periodic panels. *Journal of Sound and Vibration*, 332(6):1418–1436, 2013.
- [26] P. Deymier. *Acoustic Metamaterials and Phononic Crystals*. Springer Series in Solid-State Sciences. Springer Berlin Heidelberg, 2013.
- [27] G. Failla. An exact generalised function approach to frequency response analysis of beams and plane frames with the inclusion of viscoelastic damping. *Journal of Sound and Vibration*, 360:171–202, 2016.
- [28] M. Farhat, S. Guenneau, and S. Enoch. Ultrabroadband elastic cloaking in thin plates. *Physical review letters*, 103(2):024301, 2009.
- [29] N. A. Fleck, V. S. Deshpande, and M. F. Ashby. Micro-architected materials: past, present and future. *Proceedings of the Royal Society A: Mathematical, Physical and Engineering Sciences*, 466(2121):2495–2516, 2010.
- [30] V. E. Gasparetto and M. S. ElSayed. Multiscale optimization of specific elastic properties and microscopic frequency band-gaps of architected microtruss lattice materials. *International Journal of Mechanical Sciences*, 197:106320, 2021.

- [31] V. E. Gasparetto and M. S. ElSayed. Shape transformers for phononic band gaps tuning in two-dimensional Bloch-periodic lattice structures. *European Journal of Mechanics - A/Solids*, 89:104278, 2021.
- [32] H. He and H. Fan. Explosion vibration mitigation of meta-plate with mass–spring metastructures. *Extreme Mechanics Letters*, 42:101108, 2021.
- [33] J.-C. Hsu. Local resonances-induced low-frequency band gaps in two-dimensional phononic crystal slabs with periodic stepped resonators. *Journal of Physics D: Applied Physics*, 44(5):055401, 2011.
- [34] G. Hu, L. Tang, and R. Das. Internally coupled metamaterial beam for simultaneous vibration suppression and low frequency energy harvesting. *Journal of Applied Physics*, 123(5):055107, 2018.
- [35] T. Ikegami, T. Sakurai, and U. Nagashima. A filter diagonalization for generalized eigenvalue problems based on the Sakurai–Sugiura projection method. *Journal of Computational and Applied Mathematics*, 233(8):1927–1936, 2010.
- [36] R. Khajehtourian and D. M. Kochmann. Soft adaptive mechanical metamaterials. *Frontiers in Robotics and AI*, 8, 2021.
- [37] S.-H. Kim and M. P. Das. Seismic waveguide of metamaterials. *Modern Physics Letters B*, 26(17):1250105, 2012.
- [38] S.-H. Kim and M. P. Das. Artificial seismic shadow zone by acoustic metamaterials. *Modern Physics Letters B*, 27(20):1350140, 2013.
- [39] V. Koloušek. Dynamics of continuous beams and frame. *VTN, Prague (in Czech)*, 1950.
- [40] V. Koloušek. Dynamik der durchlaufträger und rahmen. *Fachbuchverlag, Leipzig (in German)*, 1953.
- [41] V. Koloušek. Dynamics of civil engineering structures. *Academia Praha & Butterworth, London*, 1973.
- [42] D. Lam, F. Yang, A. Chong, J. Wang, and P. Tong. Experiments and theory in strain gradient elasticity. *Journal of the Mechanics and Physics of Solids*, 51(8):1477–1508, 2003.

- [43] J. Li, X. Fan, and F. Li. Numerical and experimental study of a sandwich-like metamaterial plate for vibration suppression. *Composite Structures*, 238:111969, 2020.
- [44] S. Li, T. Chen, X. Wang, Y. Li, and W. Chen. Expansion of lower-frequency locally resonant band gaps using a double-sided stubbed composite phononic crystals plate with composite stubs. *Physics Letters A*, 380(25-26):2167–2172, 2016.
- [45] T. Li, Q. Su, and S. Kaewunruen. Seismic metamaterial barriers for ground vibration mitigation in railways considering the train-track-soil dynamic interactions. *Construction and Building Materials*, 260:119936, 2020.
- [46] X. Liu and J. Banerjee. An exact spectral-dynamic stiffness method for free flexural vibration analysis of orthotropic composite plate assemblies—part i: Theory. *Composite Structures*, 132:1274–1287, 2015.
- [47] X. Liu and J. Banerjee. An exact spectral-dynamic stiffness method for free flexural vibration analysis of orthotropic composite plate assemblies – part ii: Applications. *Composite Structures*, 132:1288–1302, 2015.
- [48] X. Liu and J. Banerjee. Free vibration analysis for plates with arbitrary boundary conditions using a novel spectral-dynamic stiffness method. *Computers and Structures*, 164:108–126, 2016.
- [49] X. Liu, H. Kassem, and J. Banerjee. An exact spectral dynamic stiffness theory for composite plate-like structures with arbitrary non-uniform elastic supports, mass attachments and coupling constraints. *Composite Structures*, 142:140–154, 2016.
- [50] Y. Liu, D. Yu, L. Li, H. Zhao, J. Wen, and X. Wen. Design guidelines for flexural wave attenuation of slender beams with local resonators. *Physics Letters A*, 362(5-6):344–347, 2007.
- [51] Z. Liu, K.-Q. Qin, and G.-L. Yu. Partially embedded gradient metabarrier: broadband shielding from seismic rayleigh waves at ultralow frequencies. *Journal of Engineering Mechanics*, 146(5):04020032, 2020.
- [52] R. Lucklum, M. Zubtsov, A. Oseev, S. Hirsch, and F. Hagemann. Phononic crystals and applications. In *AMA Conferences 2013 - SENSOR 2013, OPTO 2013, IRS 2013*, 2013.

- [53] G. Mancusi, F. Fabbrocino, L. Feo, and F. Fraternali. Size effect and dynamic properties of 2D lattice materials. *Composites Part B: Engineering*, 112:235–242, 2017.
- [54] MATLAB. *version 7.10.0 (R2010a)*. The MathWorks Inc., Natick, Massachusetts, 2010.
- [55] L. Meirovitch. *Principles and Techniques of Vibrations*. Prentice Hall, 1997.
- [56] E. Miranda Jr, E. Nobrega, A. Ferreira, and J. Dos Santos. Flexural wave band gaps in a multi-resonator elastic metamaterial plate using kirchhoff-love theory. *Mechanical Systems and Signal Processing*, 116:480–504, 2019.
- [57] D. Mu, H. Shu, L. Zhao, and S. An. A review of research on seismic metamaterials. *Advanced Engineering Materials*, 22(4):1901148, 2020.
- [58] G. Oliveto, A. Santini, and E. Tripodi. Complex modal analysis of a flexural vibrating beam with viscous end conditions. *Journal of Sound and Vibration*, 200(3):327–345, 1997.
- [59] P. F. Pai. Metamaterial-based broadband elastic wave absorber. *Journal of Intelligent Material Systems and Structures*, 21(5):517–528, 2010.
- [60] H. Peng and P. F. Pai. Acoustic metamaterial plates for elastic wave absorption and structural vibration suppression. *International Journal of Mechanical Sciences*, 89:350–361, 2014.
- [61] Y. Pennec, Y. Jin, and B. Djafari-Rouhani. Chapter two - phononic and photonic crystals for sensing applications. In M. I. Hussein, editor, *Advances in Applied Mechanics*, volume 52, pages 105–145. Elsevier, Jan. 2019.
- [62] A. S. Phani, J. Woodhouse, and N. A. Fleck. Wave propagation in two-dimensional periodic lattices. *The Journal of the Acoustical Society of America*, 119(4):1995–2005, 2006.
- [63] D. Qian and Z. Shi. Bandgap properties in locally resonant phononic crystal double panel structures with periodically attached spring-mass resonators. *Physics Letters A*, 380(41):3319–3325, 2016.

- [64] G. Romano and R. Barretta. Nonlocal elasticity in nanobeams: The stress-driven integral model. *International Journal of Engineering Science*, 115:14–27, 2017.
- [65] G. Romano and R. Barretta. Stress-driven versus strain-driven nonlocal integral model for elastic nano-beams. *Composites Part B: Engineering*, 114:184–188, 2017.
- [66] A. F. Russillo and G. Failla. On the free vibrations of locally-resonant structures. *Computers & Structures*, 241:106356, 2020.
- [67] A. F. Russillo and G. Failla. A novel reduced-order dynamic-stiffness formulation for locally resonant metamaterial plates. *Composite Structures*, 280:114811, 2022.
- [68] A. F. Russillo and G. Failla. Wave propagation in stress-driven nonlocal rayleigh beam lattices. *International Journal of Mechanical Sciences*, 215:106901, 2022.
- [69] A. F. Russillo, G. Failla, G. Alotta, F. Marotti de Sciarra, and R. Barretta. On the dynamics of nano-frames. *International Journal of Engineering Science*, 160:103433, 2021.
- [70] A. F. Russillo, G. Failla, and F. Fraternali. Free and forced vibrations of damped locally-resonant sandwich beams. *European Journal of Mechanics-A/Solids*, 86:104188, 2021.
- [71] T. Sakurai and H. Sugiura. A projection method for generalized eigenvalue problems using numerical integration. *Journal of Computational and Applied Mathematics*, 159(1):119–128, 2003.
- [72] S. Sepehri, H. Jafari, M. M. Mashhadi, M. R. H. Yazdi, and M. M. S. Fakhrabadi. Small-scale effects on wave propagation in planar micro-lattices. *Journal of Sound and Vibration*, 494:115894, 2021.
- [73] S. Sepehri, M. Mosavi Mashhadi, and M. M. Seyyed Fakhrabadi. Out-of-plane wave propagation in two-dimensional micro-lattices. *Physica Scripta*, 96(8):085704, May 2021.
- [74] H. Su and J. Banerjee. Development of dynamic stiffness method for free vibration of functionally graded Timoshenko beams. *Computers & Structures*, 147:107–116, 2015.

- [75] H. Su, J. Banerjee, and C. Cheung. Dynamic stiffness formulation and free vibration analysis of functionally graded beams. *Composite Structures*, 106:854–862, 2013.
- [76] H. Sun, X. Du, and P. F. Pai. Theory of metamaterial beams for broadband vibration absorption. *Journal of Intelligent Material Systems and Structures*, 21(11):1085–1101, 2010.
- [77] K. Wang, J. Zhou, C. Cai, D. Xu, and H. Ouyang. Mathematical modeling and analysis of a meta-plate for very low-frequency band gap. *Applied Mathematical Modelling*, 73:581–597, 2019.
- [78] Q. Wang, J. Li, Y. Zhang, Y. Xue, and F. Li. Bandgap properties in metamaterial sandwich plate with periodically embedded plate-type resonators. *Mechanical Systems and Signal Processing*, 151:107375, 2021.
- [79] T. Wang. Tunable band gaps in an inertant metamaterial plate with two-degree-of-freedom local resonance. *Physics Letters A*, 384(21):126420, 2020.
- [80] T. Wang, M. Sheng, X. Ding, and X. Yan. Wave propagation and power flow in an acoustic metamaterial plate with lateral local resonance attachment. *Journal of Physics D: Applied Physics*, 51(11):115306, 2018.
- [81] T. Wang, M.-P. Sheng, Z.-W. Guo, and Q.-H. Qin. Flexural wave suppression by an acoustic metamaterial plate. *Applied Acoustics*, 114:118–124, 2016.
- [82] T. Wang, M.-P. Sheng, and Q.-H. Qin. Multi-flexural band gaps in an euler–bernoulli beam with lateral local resonators. *Physics Letters A*, 380(4):525–529, 2016.
- [83] F. Williams and M. Anderson. Inclusion of elastically connected members in exact buckling and frequency calculations. *Computers and Structures*, 22(3):395–397, 1986.
- [84] F. W. Williams and W. H. Wittrick. Exact buckling and frequency calculations surveyed. *Journal of Structural Engineering*, 109(1):169–187, 1983.
- [85] W. Wittrick and F. Williams. A general algorithm for computing natural frequencies of elastic structures. *The Quarterly Journal of Mechanics and Applied Mathematics*, 24(3):263–284, 1971.

- [86] W. Wittrick and F. Williams. An algorithm for computing critical buckling loads of elastic structures. *Journal of Structural Mechanics*, 1(4):497–518, 1973.
- [87] Y. Xiao, J. Wen, L. Huang, and X. Wen. Analysis and experimental realization of locally resonant phononic plates carrying a periodic array of beam-like resonators. *Journal of Physics D: Applied Physics*, 47(4):045307, 2013.
- [88] Y. Xiao, J. Wen, G. Wang, and X. Wen. Theoretical and experimental study of locally resonant and bragg band gaps in flexural beams carrying periodic arrays of beam-like resonators. *Journal of Vibration and Acoustics*, 135(4), 2013.
- [89] Y. Xiao, J. Wen, and X. Wen. Flexural wave band gaps in locally resonant thin plates with periodically attached spring–mass resonators. *Journal of Physics D: Applied Physics*, 45(19):195401, 2012.
- [90] Y. Xiao, J. Wen, and X. Wen. Sound transmission loss of metamaterial-based thin plates with multiple subwavelength arrays of attached resonators. *Journal of Sound and Vibration*, 331(25):5408–5423, 2012.
- [91] Y. Xiao, J. Wen, D. Yu, and X. Wen. Flexural wave propagation in beams with periodically attached vibration absorbers: band-gap behavior and band formation mechanisms. *Journal of Sound and Vibration*, 332(4):867–893, 2013.
- [92] R. Zhu, X. Liu, G. Hu, C. Sun, and G. Huang. A chiral elastic metamaterial beam for broadband vibration suppression. *Journal of Sound and Vibration*, 333(10):2759–2773, 2014.
- [93] S. Zouari, J. Brocail, and J.-M. G enevaux. Flexural wave band gaps in metamaterial plates: A numerical and experimental study from infinite to finite models. *Journal of Sound and Vibration*, 435:246–263, 2018.